Imperial College
London

Department of Physics
Imperial College London

Graphene Plasmon Cavities

Xiaofei Xiao

A thesis submitted to Imperial College London for the degree of
Doctor of Philosophy

Supervisors:
Professor Stefan A. Maier
Doctor Vincenzo Giannini

March 2019

To my father and my family

Declaration of Authorship

I, Xiaofei Xiao, declare that this thesis titled 'Graphene Plasmon Cavities' and the work presented in it are my own. I confirm that:

- This work was done wholly or mainly while in candidature for a research degree at this University.
- Where any part of this thesis has previously been submitted for a degree or any other qualification at this University or any other institution, this has been clearly stated.
- Where I have consulted the published work of others, this is always clearly attributed.
- Where I have quoted from the work of others, the source is always given. With the exception of such quotations, this thesis is entirely my own work.
- I have acknowledged all main sources of help.
- Where the thesis is based on work done by myself jointly with others, I have made clear exactly what was done by others and what I have contributed myself.

Xiaofei Xiao

Date: September 12, 2019

Acknowledgements

First of all, I would like to sincerely thank my two supervisors, Prof. Stefan A. Maier and Dr. Vincenzo Giannini. Prof. Stefan A. Maier gave me the great opportunity to join his world-leading group and to participate in fascinating projects. His endless enthusiasm for scientific research and rigorous academic spirit will have a profound influence on my later life. Stefan, thank you for being my idol and providing me with the chance to continue my work in Munich. Dr. Vincenzo Giannini unreservedly shared his passion and intellectual curiosity for nanophotonics with me. Over the years, I've enjoyed working with him to propose new ideas, interpret complex results, and discuss my silly questions. In addition, he gave me great care and useful suggestions in my life. Vincenzo, thank you for being an excellent supervisor and for all your efforts.

Next, I want to thank all the collaborators who are involved in the projects. In particular, I would like to thank Paloma Arroyo-Huidobro, Sung-Gyu Park, Yi Li, Rupert F. Oulton, Lesley F. Cohen, Viktoryia Shautsova, Joshua D. Caldwell, Doris E. Reiter, Richard M. Kerber, Ke Li, Emiliano Cortés, Yao-Ting Wang, Avi Braun, Gustavo Grinblat for every fruitful discussion. Besides, I would like to thank all my colleagues and friends in the Plasmonic group at Imperial College. Particularly, I would like to thank Daan M. Arroo, Thomas Brick, Zhuo Wang, Rodrigo Berte, Wentao Huang, Alberto Lauri, Ibrahim Abdelwahab, Zhijie Ma, Brock Doiron, Monica Mota, Nicolas Gusken, Toshihiko Shibanuma, Harriet Walker, and Ngoc Bao Nguyen. Thank you all for the great memories. I am honoured to work with all of you. I also would like to thank all in the Giannini Theory Lab. They are Samuel Palmer, Marie Rider, Simon Pocock, Jamie Fitzgerald and Gleb Siroki. I had a wonderful time with you, and thank you for helping me improve my English. And I wish to express my sincere gratitude to Lee Family Scholars for the generous financial support and the precious chance for studying at Imperial.

Last, my family has given me a lot of understanding, support and encouragement since I have been born. The best thing in the world is their love. Most importantly, I would like to thank Miss Kebin Wu, who eternally gives care, encouragement and support over the years. Kebin, thank you for your patiences and making me a better person. Will you marry me? My family, thank you and love all of you FOREVER!

I would like to thank everyone who helped me throughout my PhD, and I apologise to those who I might have forgotten to name here.

List of Publications

Publications

[1] K. Li*, J. M. Fitzgerald*, **X. Xiao***, J. D. Caldwell, C. Zhang, S. A. Maier, X. Li,V. Giannini, "Graphene plasmon cavities made with silicon carbide", *ACS Omega*, 2, 3640-3646 (2017). (**Joint first author**)

[2] A. Lauri, L. Velleman, **X. Xiao**, E. Cortés, J. B. Edel, V. Giannini, A. Rakovich, S. A. Maier, "3D confocal Raman tomography to probe field enhancements inside supercluster metamaterials", *ACS Photonics*, 4, 2070-2077 (2017).

[3] S.-G. Park, C. Mun, **X. Xiao**, A. Braun, S. Kim, V. Giannini, S. A. Maier, D.-H. Kim, "Surface energy-controlled SERS substrates for molecular concentration at plasmonic nanogaps", *Advanced Functional Materials*, 27, 1703376 (2017).

[4] X. Wang, S.-G. Park, J. Ko, **X. Xiao**, V. Giannini, S. A. Maier, D.-H. Kim, J. Choo, "Sensitive and reproducible immunoassay of multiple mycotoxins using surface-enhanced Raman scattering mapping on 3D plasmonic nanopillar arrays", *Small*, 1801623 (2018).

[5] S. R. Pocock, **X. Xiao**, P. A. Huidobro, V. Giannini, "Topological plasmonic chain with retardation and radiative effects", *ACS Photonics*, 5, 2271-2279 (2018).

[6] **X. Xiao**, X. Li, J. D. Caldwell, S. A. Maier, V. Giannini, "Theoretical analysis of graphene plasmon cavities", *Applied Materials Today*, 12, 283-293 (2018).

[7] R. M. Kerber, J. M. Fitzgerald, **X. Xiao**, S. S. Oh, S. Maier, V. Giannini, D. Reiter, "Interaction of an archimedean spiral structure with orbital angular momentum light", *New Journal of Physics*, 20, 095005 (2018).

[8] V. Shautsova, T. Sidiropoulos, **X. Xiao**, N. A. Gusken, N. C. Black, A. M. Gilbert-son, V. Giannini, S. A. Maier, L. F. Cohen, R. F. Oulton, "Plasmon induced thermoelectric effect in graphene", *Nature Communications*, 9, 5190 (2018).

[9] V. T. N. Linh, **X. Xiao**, V. Giannini, S. A. Maier, D.-H. Kim, Y.-I. Lee, S.-G. Park, "Compact integration of TiO2 nanoparticles into the cross-points of 3D vertically stacked Ag nanowires for plasmon-enhanced photocatalysis", *Nanomaterials*, 9, 468 (2019).

[10] M. S. Rider, S. J. Palmer, S. R. Pocock, **X. Xiao**, Paloma Arroyo Huidobro, V. Giannini, "A perspective on topological nanophotonics: current status and future challenges", *Journal of Applied Physics*, 125, 120901 (2019).

[11] S. J. Palmer, **X. Xiao**, N. Pazos-Perez, L. Guerrini, M. A. Correa-Duarte, S. A. Maier, R. Craster, R. A. Alvarez-Puebla, V. Giannini, "Extraordinarily transparent compact metallic metamaterials", *Nature Communications*, 10, 2118 (2019).

[12] S.-G. Park, **X. Xiao**, J. Min, C. Mun, H.-S. Jung, V. Giannini, R.Weissleder, S. A. Maier, H. Im, D.-H. Kim, "Self-assembly of nanoparticle-spiked pillar arrays for plasmonic biosensing", *Advanced Functional Materials*, 1904257 (2019).

[13] M. Blanco-Formoso, A. Sousa-Castillo, **X. Xiao**, A. Marino-Lopez, M. Turino, N. Pazos-Perez, V. Giannini, M. A. Correa-Duarte, R. A. Alvarez-Puebla, "Boosting the analytical properties of gold nanostars by single particle confinement into Yolk porous silica shells", (2019). (Submitted to *Materials Horizons*)

Conferences

[1] **X. Xiao**, V. Giannini, S. A. Maier, "Finite-difference frequency-domain method", *London Plasmonics Forum*, 2016. (Poster)

[2] A. Lauri, **X. Xiao**, L. Velleman, E. Cortés, J. B. Edel, V. Giannini, A. Rakovich, S. A. Maier, "3D confocal Raman tomography to probe field enhancements inside super-cluster metamaterials", *London Plasmonics Forum*, 2017. (Poster)

[3] **X. Xiao**, V. Giannini, S. A. Maier, "Theoretical analysis of graphene plasmon cavity", *London Plasmonics Forum*, 2017. (Poster)

[4] **X. Xiao**, S. A. Maier, V. Giannini, "Theory of graphene plasmon cavity", *London Plasmonics Forum*, 2018. (Poster)

[5] A. Lauri, L. Velleman, **X. Xiao**, E. Cortés, J. B. Edel, V. Giannini, A. Rakovich, "3D confocal Raman mapping of field enhancement inside supercluster metamaterials (conference presentation)", *Metamaterials XI*, Vol. 10671 (International Society for Optics and Photonics, 2018), 106711O.

[6] **X. Xiao**, S. A. Maier, V. Giannini, "Theoretical analysis of graphene plasmon cavity", *Gold 2018*, 2018. (Poster)

[7] **X. Xiao**, S. A. Maier, V. Giannini, "Theory of graphene plasmon cavity", *Metamaterials 2018*, 2018. (Poster)

[8] **X. Xiao**, J. D. Caldwell, S. A. Maier, V. Giannini, "Plasmons in Suspended Graphene", *Faraday Discussion*, 2019. (Poster)

[9] **X. Xiao**, S. A. Maier, V. Giannini, "Graphene Plasmonic Cavities Operating at Infrared Frequencies", *Nanophotonics and Micro/Nano Optics International Conference 2019*, 2019. (Oral)

Abstract

In the past decades, we have witnessed the rapid growth of plasmonics, which is a field investigating the properties and applications of surface plasmon polaritons. Two key features of plasmons are that they enable us overcome the diffraction limit and they provide large field enhancement on the surface of metals. However, traditional surface plasmon polaritons have some significant drawbacks, such as high loss and low tunability. Fortunately, new materials with plasmon-like behaviour, such as graphene and silicon carbide, have recently been found both theoretically and experimentally. Compared to traditional plasmonic materials, those new materials exhibit low loss and high tunability and work at mid-infrared frequencies, significantly expanding this field. However, the coupling between different plasmon-like behaviours in those new materials has been largely unsuccessful to date.

In this thesis, we investigate the coupling between the localized surface phonon polaritons of silicon carbide and surface plasmon polaritons of graphene, by studying the tunable plasmonic cavities working at the mid-infrared frequencies, using a monolayer of graphene deposited on a silicon carbide grating. Models for graphene plasmonic cavities are established to reveal the underlying physics. We first focus on a simple model by considering a Fabry-Pérot model in the horizontal cavity direction, in which the commonly used dispersion relation of graphene plasmons is applied. Then, we improve the model by deriving a new dispersion relation, revealing the cavity height dependence of the dispersion relation of graphene plasmons. A Fabry-Pérot model in the vertical cavity direction is also established. Last, we establish the model of the suspended graphene plasmon cavities based on the newly derived relationship. In addition, we realize several interesting features by optimizing the proposed system, such as complete absorption, extremely high field enhancement and extraordinary field compression. All these models are confirmed by the numerical simulations.

Table of Contents

Contents *Page*

List of Figures

List of Tables

CHAPTER

1

Introduction

1.1 General Introduction

Plasmonics is an emerging sub-discipline of nano-photonics that allows the full manipulation of light at the nanoscale via plasmons [1–4]. Surface plasmon polaritons (SPPs) arise due to the strong coupling of photons and charge systems. They generally exist on the surface of conductive materials (such as metals, highly doped semiconductors, graphene). SPPs can be categorised into two groups [5–7]: One is called propagating SPPs, which exist in one-dimensional (such as the surface of a metallic nanowire) and two-dimensional systems (such as the interface between a dielectric and a metal), and their electromagnetic energy propagates in a certain direction. Another one is called localized SPPs, which primarily exist on the surface of zero-dimensional systems, such as the surface of a metallic nanoparticle. In this case, SPPs are confined in three directions, and hence the electromagnetic energy cannot be transmitted.

Unlike ordinary optical phenomena, SPPs possess some preeminent optical properties, such as selective scattering of light and extreme field enhancement. It is particularly noteworthy that the diffraction limit can be overcome because the sub-wavelength confinement of electromagnetic waves can be realized by using SPPs [6, 8, 9]. A large number of studies have shown that these distinct optical properties enable SPPs to have promising prospects for applications in the fields of biology, chemistry, energy, and information, including single molecule sensors [6, 10, 11], efficient solar cells [12–14], metasurfaces [15, 16] and photonic integrated circuits [17, 18]. Previously, this field mainly investigated the optical properties of SPPs on noble metallic materials (such as gold and silver), especially their excitation techniques, propagation and loss properties, manipulation approaches, and potentials in applications [6, 19–21]. It should be noted that the operating frequencies of SPPs on metals are at the visible and near infrared bands.

However, the traditional SPPs on metals represent some drawbacks: On the one hand, there is a trade-off between the confinement ability of electromagnetic field and the loss when using lossy materials. Usually, the smaller the confinement dimension, the larger the loss, and vice versa.

Certainly, miniaturized integrated optical systems are expected. At present, the characteristic scale of the device has reached dozens of nanometers, about one tenth of the wavelength of visible light. With such a small scale of the confinement, the loss is bound to be very large. How to effectively reduce the loss of SPPs has become an urgent problem in plasmonics. Approaches based on the dynamic modulation depend entirely on the adjacent functional materials (such as quantum dots, liquid crystals and other electro-optic materials). However, this greatly increases the difficulty of fabrication and instability of the integrated system.

Graphene plasmons (GPs) offer us the ability to solve the mentioned problems, thanks to the fact that the properties of GPs are significantly different from the traditional SPPs on metals [22–30], because graphene has a special electronic band structure, GPs exhibit unique electrical tunability [31,32], low intrinsic loss [33,34] and high field confinement [35,36]. The resonance frequencies of GPs are continuously tunable from mid-infrared to terahertz [37], thus greatly expanding the range of operating frequency of plasmons. These properties make GPs have a high potential in a range of applications [38] (as shown in Figure 1.1), including the fields of bio-chemical sensors, active devices, spectroscopy and infrared/terahertz detection. In addition, silicon carbide (SiC), as an exemplary polar dielectric, exhibits a plasmon-like behaviour known as surface phonon polaritons (SPhPs), which operate at mid-infrared frequencies. However, coupling GPs and SPhPs have been largely unsuccessful to date.

In this thesis, we focused on this issue and the key targets are summarized as follows: First, we attempted to couple the localized SPhPs of SiC with SPPs of graphene, and to create tunable plasmonic cavities in the mid-infrared range. Second, we established models for those plasmonic cavities and reveal the physics behind. Third, we tried to reveal the insufficiency of current theories and to improve them by introducing necessary corrections. Fourth, we anticipated realizing several interesting features by optimizing the proposed system, such as complete absorption, extremely high field enhancement and extraordinary field compression.

1.2 The Electromagnetism Theory

Nanophotonics is the study of the interaction between the electromagnetic fields with the materials on the nanometer scale. All findings reported here belong to a major part of nano-photonics, namely plasmonics. Plasmonics provides us the ability to confine the electromagnetic waves over the sub-wavelength dimensions, based on the interaction between the electromagnetic fields with the free charge carriers in conductors. In this section, we will first review the mathematical description of optics, Maxwell's Equations. Subsequently, we will summarize the permittivity and the permeability of materials. The classical model for metals, the Drude model, will also be derived from the Drude-Lorentz model in this section.

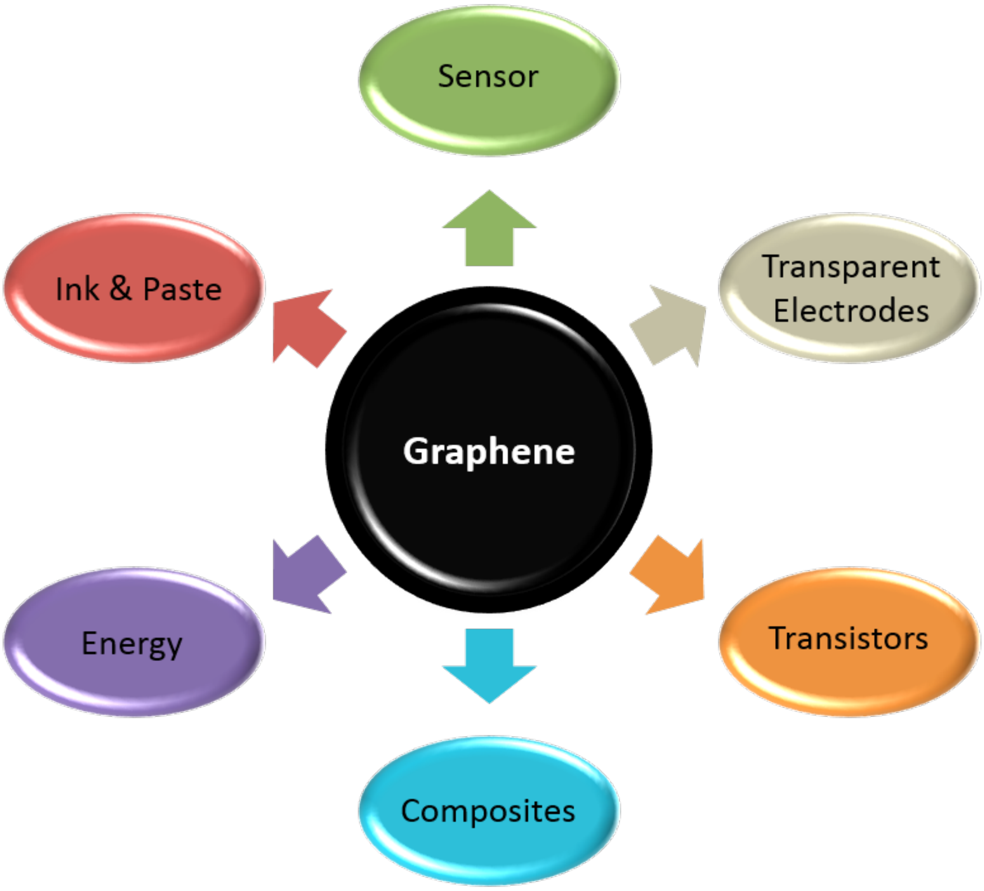

Figure 1.1: Overview of applications using graphene.

1.2.1 Maxwell's Equations

Maxwell's equations are concise equations that are used to model the interaction between electromagnetic waves and matter. Their establishment was one of the most important achievements of the 19th century. Although based on the efforts of a number of physicists, these equations are summarized by the physicist and mathematician James Clerk Maxwell, and establish the foundation of the classical electromagnetic theory.

There exist two major variants - the microscopic and the macroscopic Maxwell's equations. The microscopic formulation relates the fields (the electric field $\mathbf{E}$ and the magnetic induction $\mathbf{B}$) to the total charge and current in the system, so it has the universal applicability. However, it is very difficult to be directly used in the calculations, because of the complexity of the calculation of the total charge and current that include the ones at the atom scale. The macroscopic formulation avoids this calculation complexity by introducing two new auxiliary fields (the electric displacement $\mathbf{D}$ and the magnetization field $\mathbf{H}$). We summarize the macroscopic Maxwell's equations in the differential form here

$$
\begin{aligned}
\nabla \cdot \mathbf{D}(\mathbf{r}, t) &= \rho_{ext}(\mathbf{r}, t), && (1.1)\\
\nabla \cdot \mathbf{B}(\mathbf{r}, t) &= 0, && (1.2)\\
\nabla \times \mathbf{E}(\mathbf{r}, t) &= -\frac{\partial \mathbf{B}(\mathbf{r}, t)}{\partial t}, && (1.3)\\
\nabla \times \mathbf{H}(\mathbf{r}, t) &= \mathbf{J}_{ext} + \frac{\partial \mathbf{D}(\mathbf{r}, t)}{\partial t}, && (1.4)
\end{aligned}
$$

where $\rho_{ext}(\mathbf{r}, t)$ is the external charge density, and $\mathbf{J}_{ext}$ is the external current density. Equations (1.1) to (1.4) represent Gauss' law for the electric field (which is also known as Gauss' flux theorem), Gauss' law for the magnetic field, Faraday's law, and Ampère's law, respectively. Gauss' law reflects that the electric field originates from a source, that is, it describes the properties of the electric field. Similar to Gauss' law for electric field, Gauss' law for magnetic states that magnetic monopoles do not exist and describes the properties of magnetic field. Faraday's law demonstrates that a time-varying magnetic field generates an electric field, while Ampère's law indicates that a time-varying electric field generates a magnetic field via introducing the displacement current hypothesis by Maxwell. Maxwell's equations show that the electric field and magnetic field are not isolated from each other. The varying magnetic field can generate the vortex electric field, and vice versa. The varying electric and magnetic fields are always closely linked and generate each other to form the electromagnetic field as a whole, which is also the basic concepts of Maxwell's equations and the core idea of electromagnetics. Maxwell's equations predicate the existence of electromagnetic waves. From the point of view of future generations, the greatest contribution of these equations is to clearly reveal how electromagnetic waves propagate in space.

The auxiliary fields can be related to the electric and magnetic fields via the constitutive relations. Although the form of these relations is dependent on the properties of the materials applied, the form for the homogeneous isotropic material is simple as follows

$$
\begin{aligned}
\mathbf{D} &= \epsilon_0 \mathbf{E} + \mathbf{P} = \epsilon \epsilon_0 \mathbf{E}, && (1.5)\\
\mathbf{H} &= \frac{1}{\mu_0}\mathbf{B} - \mathbf{M} = \frac{1}{\mu \mu_0}\mathbf{B}, && (1.6)
\end{aligned}
$$

where $\mathbf{P}$ is the polarization of the material, and $\mathbf{M}$ is the magnetization of the material, ϵ_0 is the vacuum permittivity, μ_0 is the vacuum permeability, ϵ is the relative permittivity of the material and μ is the relative permeability of the material. It should be noted that the International System of Units are applied in this thesis and that all materials used are non-magnetic ($\mu = 1$), and hence the refraction index n equals to $\sqrt{\epsilon}$. Furthermore, we can relate the relative permittivity and the relative permeability to the electric (χ) and magnetic (χ_m) susceptibilities (which are used to describe the degree of the change of a matter under the an external electric and magnetic fields) via

$$\begin{aligned} \epsilon &= 1 + \chi, & (1.7) \\ \mu &= 1 + \chi_m. & (1.8) \end{aligned}$$

The permittivity and permeability will be further interpreted in the following section. In this thesis, the relative permittivity and the relative permeability will be called the permittivity and the permeability for short.

1.2.2 Helmoltz Equation and Boundary Conditions

Maxwell's equations form the foundation of the electromagnetism and hence the classical plasmonics. In the following, we will derive the wave equation based on Maxwell's equations considering the homogeneous material cases without external charge ($\rho_{ext} = 0$) and current ($\mathbf{J}_{ext} = 0$) densities. Applying the vector identity $\nabla \times \nabla \times \mathbf{E} = \nabla(\nabla \cdot \mathbf{E}) - \nabla^2 \mathbf{E}$, we obtain the core formula of the electromagnetic wave theory

$$\nabla^2 \mathbf{E} - \frac{\epsilon}{c^2} \frac{\partial^2 \mathbf{E}}{\partial t^2} = 0, \tag{1.9}$$

where $c = \frac{1}{\sqrt{\epsilon_0 \mu_0}}$ is the light speed in vacuum. Considering the time-harmonic dependence of the electric field (where $\mathbf{E}(t) = \mathbf{E}_0 e^{-i\omega t}$, thus $\frac{\partial}{\partial t} = -i\omega$), we obtain the so-called Helmoltz equation for monochromatic waves in the homogeneous isotropic medium with the permittivity of ϵ

$$\nabla^2 \mathbf{E} + k_0^2 \epsilon \mathbf{E} = 0, \tag{1.10}$$

where $k_0 = \frac{\omega}{c}$ represents the wavevector in vacuum with the angular frequency ω.

Maxwell's equations can be used to describe the behaviour of electromagnetic fields in the non-homogeneous medium (where the permittivity and permeability should be spatially dependent). However, we usually consider homogeneous media as mentioned. This begs the question: How to describe the behaviour of electromagnetic fields across the interface between two materials? Boundary conditions provide the answer. Considering the interface between a medium i and a medium j, the boundary conditions reads

$$\begin{aligned} \mathbf{E}_t^i - \mathbf{E}_t^j &= 0, & (1.11) \\ \mathbf{H}_t^i - \mathbf{H}_t^j &= \mathbf{J}_s \times \mathbf{n}, & (1.12) \end{aligned}$$

where $\mathbf{n}$ represents the normal vector of the interface from medium j to medium i, $\mathbf{E}_t^i$ and $\mathbf{H}_t^i$ ($\mathbf{E}_t^j$ and $\mathbf{H}_t^j$) represent the tangential components of the electric field and the magnetic field in medium i (medium j), and $\mathbf{J}_s$ represents the surface current density at the interface. The surface current density can be related to the electric field via the conductivity σ

$$\mathbf{J}_s = \sigma \mathbf{E}. \tag{1.13}$$

Therefore, we could obtain the simplified equations of boundary conditions

$$\begin{aligned} \mathbf{E}_t^i &= \mathbf{E}_t^j, & (1.14) \\ \mathbf{H}_t^i - \mathbf{H}_t^j &= \sigma \mathbf{E}^i \times \mathbf{n}. & (1.15) \end{aligned}$$

Boundary conditions tell us that the tangential components of the electric field $\mathbf{E}$ and the magnetization field $\mathbf{H}$ must be continuous across the boundary when the surface current density does not exist. This is valid when dielectrics are considered. In this thesis, the graphene layer can be modelled as a surface with a complex surface conductivity, which means the surface current density should be considered.

Indeed, the Helmholtz equation and boundary conditions are very important for the numerical calculation in optics. Understanding these equations also helps us to derive the analytical expression for the phenomena of interest. In the following part of this thesis, both approaches will be used.

1.2.3 Permeability and Permittivity

As can be seen in the constitutive relations (Equations (1.5) and (1.6)), permittivity is used to measure the degree of the polarization of a material in response to an applied electric field, while permittivity is employed to describe the ability to establish a magnetic field inside of a medium when a medium is magnetized. In order to explain the physics behind the permeability and permittivity of a medium, several models were proposed. Among them, the Drude-Lorentz model is the most important and the most commonly used one. In the following, we will focus on this model and its derivative model.

1.2.3.1 The Drude-Lorentz model

In this section, we will briefly describe the derivative process of the Drude-Lorentz model using a classical method. We begin by considering an intuitively familiar system - a mass on a spring system. In order to account for loss, we will explicitly put a damper in the system. It turns out that this intuitively familiar system is an extremely good analogy to an electron cloud around a nucleus. In the mass-spring system, we could pull on the mass, and stretch the spring. In the electron-nucleus system, an electric field could be applied to put electric forces on charge carriers, and hence push the nucleus in one direction and push electric cloud to the opposite direction, due to the opposite charges they have. Therefore, this electron cloud is stretched just like the mass on the spring when the mass is pulled on. If we release the mass on the spring, the mass would bounce back, and pull back and forth around the equilibrium position. Similarly, if we were to let go of that electron cloud, it would slosh back and forth on either side of the nucleus, and it would be resonant. Similar to the equation for the mass-spring system, we can reduce the equation of motion for the electron-nucleus system as follows

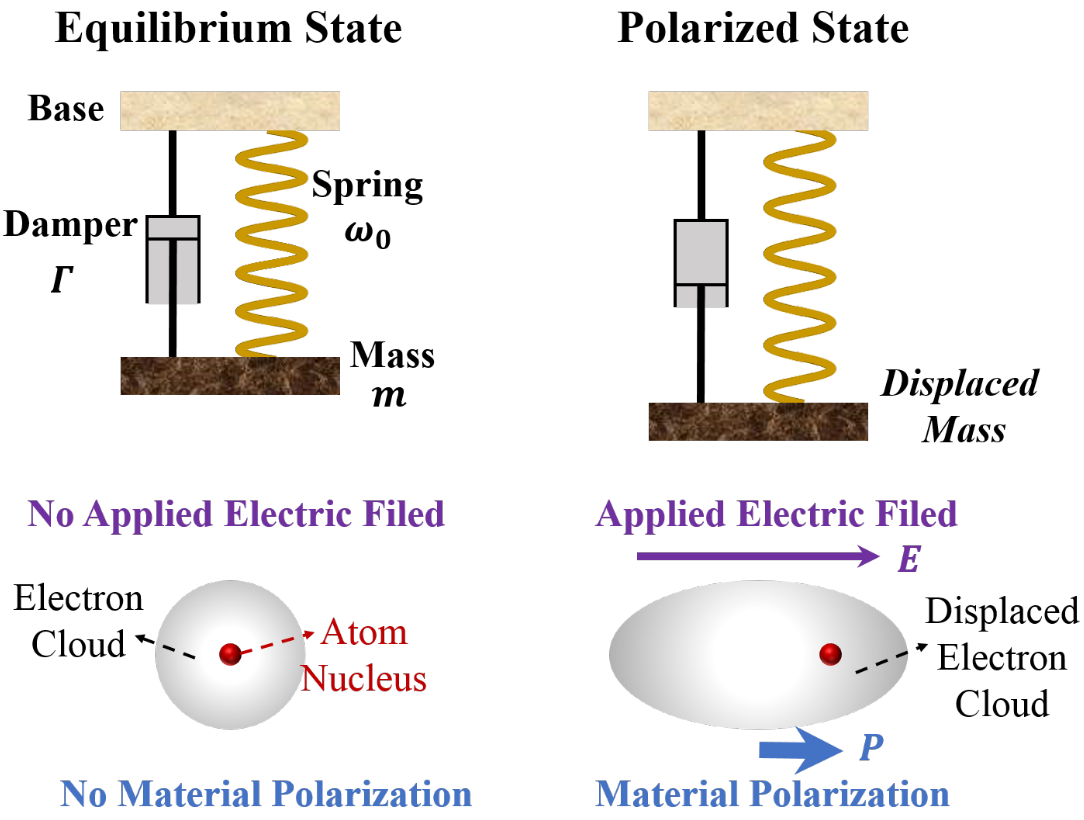

Figure 1.2: Schematic representation of Lorentz oscillator model: In the mass-spring system, a solid object with a finite mass is suspended on a spring. The spring is held by the base. A damper also exists between the base and the solid object. This system is an analogy of an electron-nucleus system. In the electron-nucleus system, there are an electron cloud and an atom nucleus. The electron cloud is marked in gray, while the nucleus is marked as a little red ball. When there is no applied electric field, the electric cloud is symmetric around the nucleus. However, the electron-nucleus system will be polarized in response to an applied electric field.

$$m\frac{\partial^2 \mathbf{r}}{\partial t^2} + m\Gamma\frac{\partial \mathbf{r}}{\partial t} + m\omega_0^2\mathbf{r} = -q\mathbf{E} \tag{1.16}$$

where the first term represents the acceleration force, the second term represents the frictional force, the third term represents the restoring force, the term on the right side of the equation is the driving force, the electric force, **r** is the distance of the charge from the center, $m \equiv m_e$

is the mass of an electron, Γ is the damping rate, $\omega_0 = \sqrt{\frac{K}{m}}$ is the natural frequency, and $q = q_e$ is the charge of a electron. This equation can be solved by applying a Fourier transform to transform this time-domain equations to a frequency-domain equation: Considering the time-harmonic dependence of the electric field ($\mathbf{E}(t) = \mathbf{E}_0 e^{-i\omega t}$, thus $\frac{\partial}{\partial t} = -i\omega$) and the similar form of the displacement of the electron ($\mathbf{r}(t) = \mathbf{r}_0 e^{-i\omega t}$), we can rewrite the equation in the following form with the explicit expression of the frequency dependence

$$(-m\omega^2 - i\omega m\Gamma + m\omega_0^2)\mathbf{r}(\omega) = -q\mathbf{E}(\omega) \tag{1.17}$$

which leads to the displacement

$$\mathbf{r}(\omega) = -\frac{q_e}{m_e}\frac{\mathbf{E}(\omega)}{\omega_0^2 - \omega^2 - i\omega\Gamma}. \tag{1.18}$$

The displacement is now described in terms of the driving electric field and the Lorentz parameters and can be interpreted as follows: When there is no electric field, the electron cloud fills around the nucleus and has a symmetric distribution. However, the nucleus gets pushed one way and the electron cloud gets pushed another when an electric field is applied. The overall displacement of the cloud is what we are calling $\mathbf{r}(\omega)$ here. Therefore, we conclude that the electric dipole moment of the charge displaced by $\mathbf{r}$ should be $-q_e\mathbf{r}$. According to the definition, the Lorentz polarizability $\alpha(\omega)$ for a single atom reads

$$\alpha(\omega) = \frac{q_e^2}{m_e}\frac{1}{\omega_0^2 - \omega^2 - i\omega\Gamma}. \tag{1.19}$$

It should be bear in mind that the polarizability of anisotropic materials should be a tensor. For simplicity, the scalar form is still employed here. Given that the total electronic polarization $\mathbf{P}_e$ of the material is defined as the volume averaged dipole moment, the material polarization reads

$$\mathbf{P}_e(\omega) = -Nq_e\mathbf{r} = \epsilon_0\chi(\omega)\mathbf{E}(\omega), \tag{1.20}$$

where N represents the number of atoms per unit volume. This equation leads to the susceptibility considering Equation (1.18)

$$\chi(\omega) = \frac{\omega_p^2}{\omega_0^2 - \omega^2 - i\omega\Gamma}. \tag{1.21}$$

Therefore, the displacement field reads as follows by considering the relation between the polarization and the applied field

$$\mathbf{D}(\omega) = \epsilon\epsilon_0\mathbf{E}(\omega) = \epsilon_0\mathbf{E}(\omega) + \mathbf{P}_e(\omega) = \epsilon_0(1 + \chi(\omega))\mathbf{E}(\omega). \tag{1.22}$$

Thus, the permittivity of a material with a single resonance is

$$\epsilon(\omega) = 1 + \chi(\omega) = 1 + \frac{\omega_p^2}{\omega_0^2 - \omega^2 - i\omega\Gamma}, \tag{1.23}$$

where ω_p ($\omega_p^2 = \dfrac{Nq_e^2}{\epsilon_0 m_e}$) is called the plasma frequency. This model also has another name, the Lorentz model, and has a characteristic feature of a harmonic oscillator with damping meaning $\epsilon(\omega)$ is a complex value. There are two special cases that we are particularly interested in: The first one is used to describe the response of the conduction electrons in metallic materials, while the second one is applied to represent the optical photon effect on the permittivity of the polar dielectrics.

Although we have fully derived the permittivity in the Drude-Lorentz model, I still want to mention another commonly used form of it, and show the difference in the derivation procedure. When considering the polarization associated with the static ion cores background, the polarization of the medium will become

$$\mathbf{D}(\omega) = \epsilon\epsilon_0\mathbf{E}(\omega) = \epsilon_0\mathbf{E}(\omega) + \mathbf{P}_e(\omega) + \mathbf{P}_{back}(\omega), \tag{1.24}$$

where the $\mathbf{P}_{back}(\omega) = (\epsilon_\infty - 1)\epsilon_0\mathbf{E}(\omega)$ is the background polarization associated with the static ion cores, and ϵ_∞ is the permittivity at high frequency. Consequently, the permittivity in the Drude-Lorentz model reads

$$\epsilon(\omega) = \epsilon_\infty + \frac{\omega_p^2}{\omega_0^2 - \omega^2 - i\omega\Gamma}. \tag{1.25}$$

Equation (1.25) model a real material, while Equation (1.23) describes an ideal free-electron material. In real materials, such as noble metals (Au and Ag), when the frequency is larger than the plasma frequency ($\omega > \omega_p$), a high polarized background caused by the filled d band exists. Thus the background polarization should be added, while the $\mathbf{P}_e$ represents the polarization associated to the free electrons (the free s electrons in this case). Therefore, the permittivity at high frequency exists, and usually the value of ϵ_∞ is between 1 and 10. However, in ideal free-electron materials, the polarized environment is ignored, and therefore $\epsilon_\infty = 1$, when $\omega > \omega_p$. In the following part of this thesis, both of the expression are used. Please be careful about which one is applied.

It also should be noted that a Drude-Lorentz model for permeability has the same format as the one for permittivity

$$\mu(\omega) = \mu_\infty + \frac{\omega_{mp}^2}{\omega_{m0}^2 - \omega^2 - i\omega\Gamma_m} \tag{1.26}$$

where all the parameters have the similar name: ω_{mp} is the magnetic plasma frequency, ω_{0p} is the magnetic resonance frequency, Γ_m is the magnetic damping rate, and μ_∞ is the permeability at high frequency. In most cases, only non-magnetic materials are considered.

The Drude-Lorentz model provides a good explanation for the physics behind the behaviour of the permeability and permittivity in a medium. However, there are many possibilities for the plasma frequency in the real atoms, because there are tens of electron levels. In addition to the electron transitions, many other sources of resonances exist. All these resonances can be modelled in the Drude-Lorentz model. Therefore, the generalization of the Drude-Lorentz model should include all these mechanisms. Indeed, the general Drude-Lorentz model is in a summation form. This is out of the scope of this thesis, and will not be included here.

Besides, it should be noted that the permeability and the permittivity are fundamentally tied to Maxwell's equations as the constants included in Maxwell's equations. However, the refractive index and the impedance of a material are indeed more intuitive parameters that really tell us what happens when a wave propagates in a medium.

1.2.3.2 The Drude model

The Drude model is a special case of the Drude-Lorentz model. In metals, most electrons move freely because they are not bound to the nucleolus. As a result, the restoring force in Equation (1.16) can be regarded as a negligible force. Therefore, we come to the well-know Drude model (from Equation (1.25)) for metallic materials by assuming $\omega_0 = 0$

$$\epsilon(\omega) = \epsilon_\infty - \frac{\omega_p^2}{\omega^2 + i\omega\Gamma} \tag{1.27}$$

where we use the definition the plasma frequency $\omega_p^2 = \dfrac{Nq_e^2}{\epsilon_0 m_e^*}$, N represents the electron density, and m_e^* represents the effective mass of the electron, the damping rate Γ is called collision frequency that can be expressed as $\dfrac{2\pi}{\tau_D}$, and τ_D is the collision time. The Drude model has been widely used, because it is an accurate description of the optical property of the metallic material, except the spectral region where the interband transition should be considered. It reveals the key features of the permittivity of a metal: When the frequency is smaller than the plasma frequency, the real part of the permittivity is negative, and hence the incident light is strongly reflected. However, the material behaves like a traditional dielectric when the frequency is larger than the plasma frequency. When the ideal free-electron material model ($\epsilon_\infty = 1$) is considered and the attenuation is neglected ($\Gamma = 0$), the Drude model can be deduced to the following form

$$\epsilon(\omega) = 1 - \frac{\omega_p^2}{\omega^2}. \tag{1.28}$$

This equation will be used to derive the key features of SPPs on metals in the following of this thesis.

1.3 Surface Plasmons

In this section, we will summarize the most important facts and phenomena in plasmonics, when using traditional plasmonic materials. The famous dispersion relation of SPPs at a single interface will be also presented here.

1.3.1 Polaritons

Polaritons are the collective excitations and are an emergent phenomenon that forms when photons couple strongly with electric or magnetic dipole-carrying excitations in solids. As can be seen from an example shown in Figure 1.3, the dispersion relation in this process follows the anti-crossing principle, which forms two different branches in the dispersion curves, namely upper and lower polariton branches, respectively. The anti-crossing points occurs due to the strong interaction of the sub-systems (the photons and the charged excitations) in the whole system. Two different branches represent two distinct kinds of modes: The upper branch above the light line in free space has smaller wavevectors representing unbound or radiative modes, while the lower branch below the light line corresponds to the bound or surface polariton modes. In the perspective of the dielectric theory, the electromagnetic fields with the frequency in the upper branch feel the medium as transparent material.

The surface polariton modes would be more interesting, and are usually accompanied by strong resonance and therefore strong absorption. Those modes, and therefore all the physics, are tightly bound to the interface between the dielectric and metallic materials. We could be inspired by considering the characteristic skin depth, δ_c, of a metal under Drude model at the low frequencies

$$\delta_c \sim \frac{1}{\sqrt{2\sigma_0 \omega \mu_0}}. \tag{1.29}$$

where $\sigma_0 = \frac{N q_e^2 \tau_D}{m_e^*}$. This indicates those surface polariton modes are confirmed on the surface of metals. Such modes will be discussed further in the following sections.

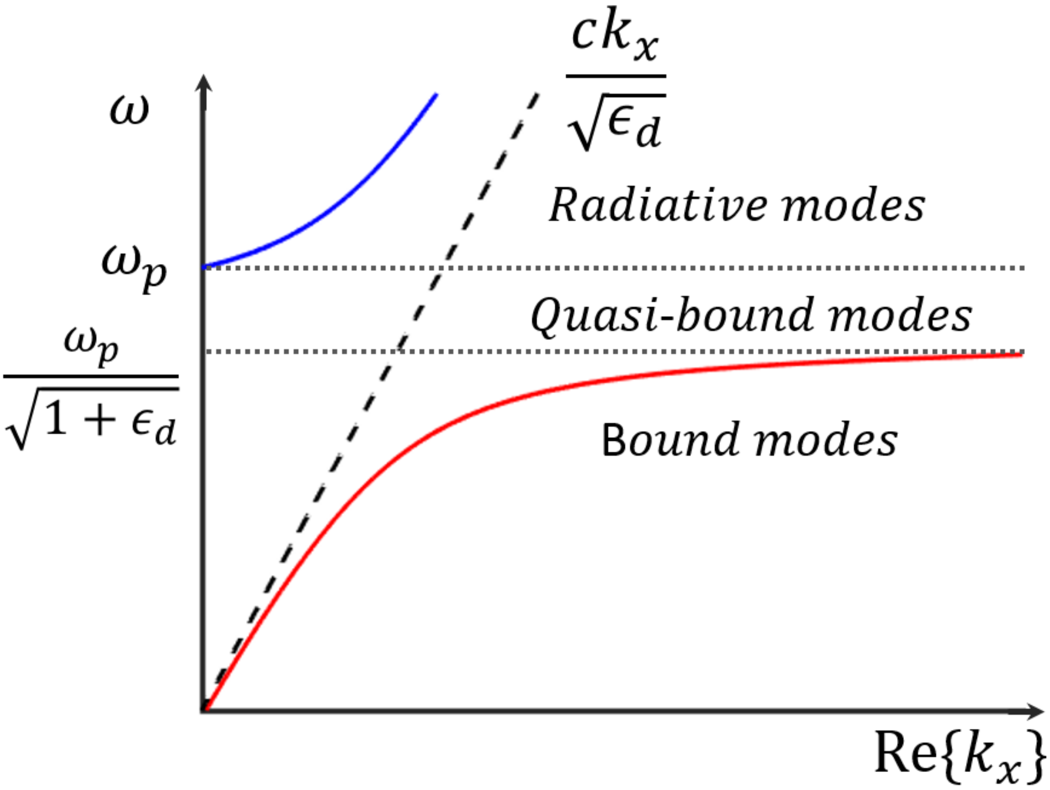

Figure 1.3: Dispersion relation of a typical kind of polaritons – surface plasmon polaritons: There exist three different modes. However, there are two branches that can be reflected in the dispersion curves. The upper branch corresponds to the radiative modes. In this spectral region, $Re\{\epsilon_m\} > 0$, and hence both k_x and k_z are real numbers. The lower branch represents the bound modes. In this spectral region, $Re\{\epsilon_m\} < -\epsilon_d$, and hence k_x are a real number, while k_z is an imaginary number. The middle spectral regtion corresponds to quasi-bound modes, where k_x is purely imaginary, because $-\epsilon_d < Re\{\epsilon_m\} < 0$. ϵ_m and ϵ_d are the permittivities of metal and dielectric that consist of the system. The system configuration is shown in Figure 1.4.

1.3.2 Surface Plasmon Polaritons

Before the exposition of GPs, traditional SPPs, arising due to collective oscillations of free charge carries in conductors [1, 39], at a single interface in a multilayer system will be also brief presented here to understand the physical insight of these bound modes. Because SPPs are able to achieve sub-wavelength confincement, they have attracted significant interest [6, 9]. Understanding the principle of traditional SPPs helps us to comprehend the properties of GPs.

The simplest plasmonic system is a two-dimensional geometry consisting of two semi-infinite space with two different materials, dielectric (upper semi-space) and metal (lower semi-space), as shown in Figure 1.3. The relative permittivities and permeabilities are ϵ_i and μ_i, respectively, where $i = 1, 2$ represent dielectric ($\epsilon_1 > 0$) and metal, respectively. Let us recall that the following assumptions are used without specification in this thesis, unless otherwise stated: The electromagnetic fields are assumed to have a harmonic time dependence ($\mathbf{E}(t) = \mathbf{E}_0 e^{-i\omega t}$, thus $\frac{\partial}{\partial t} = -i\omega$), and the spaces occupied are source-free regions ($\mathbf{J}_{ext} = 0$), and all materials used are non-magnetic ($\mu_i = 1$). Given that the surface polariton mode is confined to the interface of the two materials and decaying in the perpendicular z-direction, we assume that a wave propagates along the x-direction in the XOZ plane ($\frac{\partial}{\partial x} = i\beta$) and confined to the surface at $z = 0$. The electric field is assumed to have the form $\mathbf{E}(x, y, z) = \mathbf{E}_z e^{i\beta x}$, where β has a complex value and is named the propagation constant corresponding to the x-component of the wavevector (k_x). Certainly, the light could be decomposed into two polarizations: the transverse electric (TE) polarization and traverse magnetic (TM) polarization. We will consider each polarization individually.

Figure 1.4: Configuration of single interface system: There exist two semi-spaces. The upper one consists of a dielectric with the permittivity ϵ_d, while the lower one consists of a metal with the permittivity ϵ_m. However, in order to deal with the general case, we consider ϵ_1 and ϵ_2 here representing the permittivities of the media. The system is homogeneous in the y-direction.

Let us first consider the possibility of a TM solution. For TM polarized mode, the magnetic field is parallel to the interface. In consideration of the homogeneity in the y-direction ($\frac{\partial}{\partial y} = 0$), the non-zero components of the electromagnetic fields are as follows: In the upper space ($z > 0$),

$$E_x = iA_2 \frac{1}{\omega\epsilon_0\epsilon_2} k_{z2} e^{i\beta x} e^{-k_{z2}z}, \tag{1.30}$$

$$H_y = A_2 e^{i\beta x} e^{-k_{z2}z}, \tag{1.31}$$

$$E_z = -A_1 \frac{\beta}{\omega\epsilon_0\epsilon_2} k_{z2} e^{i\beta x} e^{-k_{z2}z}, \tag{1.32}$$

and in the lower space ($z < 0$)

$$E_x = -iA_1 \frac{1}{\omega\epsilon_0\epsilon_1} k_{z1} e^{i\beta x} e^{k_{z1}z}, \tag{1.33}$$

$$\begin{aligned} H_y &= A_1 e^{i\beta x} e^{k_{z1} z}, && (1.34) \\ E_z &= -A_1 \frac{\beta}{\omega \epsilon_0 \epsilon_1} k_{z2} e^{i\beta x} e^{k_{z1} z}, && (1.35) \end{aligned}$$

where k_{zi} $(i = 1, 2)$ is the z-component of the wave vector in the two spaces and is positive (since we explicitly take the signage in those equations), and A_1 and A_2 are the amplitude of y-component of the magnetization fields in the upper and lower spaces. Based on this set of equations, we find that all fields are evanescent waves, which means they are confined to the interface.

According to the boundary conditions at the interface ($z = 0$), we conclude

$$A_1 = A_2, \tag{1.36}$$

and

$$\frac{k_{z2}}{k_{z1}} = -\frac{\epsilon_2}{\epsilon_1}. \tag{1.37}$$

Given that k_{z1} and k_{z2} are both positive, we deduce that the real parts of ϵ_1 and ϵ_2 are with opposite signs ($Re\{\epsilon_1\} < 0$ and $\epsilon_2 > 0$). That means that the SPPs only can exist at the interface between two materials with permittivities having opposite signs. The best-known interface is the one formed between a dielectric ($\epsilon_1 = \epsilon_d$) and a metal ($\epsilon_2 = \epsilon_m$).

Based on Equation (1.10), the generic wave equation for TM polarized light is deduced

$$\frac{\partial H_y}{\partial z^2} + (k_0^2 \epsilon - \beta^2) H_y = 0. \tag{1.38}$$

Hence, the following relations are derived when Equation(1.38) is fulfilled

$$\begin{aligned} k_{z1}^2 &= \beta^2 - \epsilon_d k_0^2, && (1.39) \\ k_{z2}^2 &= \beta^2 - \epsilon_m(\omega) k_0^2, && (1.40) \end{aligned}$$

Combining Equations (1.37), (1.39) and (1.40), we come to the most famous dispersion relation of SPPs at a single interface

$$\beta = k_0 \sqrt{\frac{\epsilon_m(\omega)\epsilon_d}{\epsilon_m(\omega) + \epsilon_d}} \tag{1.41}$$

The calculated dispersion relation of SPPs is shown in Figure 1.3. Here, the x-component (k_x) of the wavevector refers to β. In the lower branch, when the frequency is very small, the dispersion curve is close to the light line indicting that the SPP acts as a photon. However, the dispersion curve bends over with the increase of the frequency, and asymptotically reaches a frequency limit. This frequency limit is named the surface plasma frequency ω_{sp}, and it located at the frequency when beta reaches an extremum and hence $Re\{\epsilon_m(\omega_{sp})\} = -\epsilon_d$. We then apply the Drude model in Equation (1.28) to estimate the permittivity of a metal, and hence the surface plasma frequency reads

$$\omega_{sp} = \frac{\omega_p}{\sqrt{1+\epsilon_d}}. \tag{1.42}$$

This equation shows clearly that the surface plasma frequency is below the (bulk) plasma frequency.

Then, we move on to the TE polarized modes. With the similar analysis, we could conclude that the electromagnetic fields in a TE solution read as follows: In the upper space ($z > 0$),

$$\begin{aligned} E_y &= A_2 e^{i\beta x} e^{-k_{z2}z}, & (1.43)\\ H_x &= -iA_2 \frac{1}{\omega\mu_0} k_{z2} e^{i\beta x} e^{-k_{z2}z}, & (1.44)\\ H_z &= A_2 \frac{\beta}{\omega\mu_0} e^{i\beta x} e^{-k_{z2}z}, & (1.45) \end{aligned}$$

and in the lower space ($z < 0$)

$$\begin{aligned} E_y &= A_1 e^{i\beta x} e^{k_{z1}z}, & (1.46)\\ H_x &= iA_1 \frac{1}{\omega\mu_0} k_{z1} e^{i\beta x} e^{k_{z1}z}, & (1.47)\\ H_z &= A_1 \frac{\beta}{\omega\mu_0} e^{i\beta x} e^{k_{z1}z} & (1.48) \end{aligned}$$

According to the boundary condition, the following equation need to be satisfied

$$A_1(k_1 + k_2) = 0. \tag{1.49}$$

Because the real part of both wavevectors is positive, this condition is guaranteed only when $A_1 = 0$. As a consequence, it is impossible to exist the TE mode at the air-metal interface. However, it should bear in mind that it is indeed possible to stimulate TE modes when magnetic materials are applied.

It is worth noted that the key advantages of SPPs: First, the field on the metal surface is enhanced, which could benefit molecular detection, such as surface-enhanced Raman spectroscopy [40,41]. Second, the field is confined on the surface beyond the diffraction limit, which is useful for the integrated optical systems [42].

1.4 Numerical Algorithms

Mie theory provides an analytical approach to investigate the plasmonic behaviour of resonators in very simple geometries, such as spheroidal resonators, however, it fails to provide analytical solution for more complicated geometries. Fortunately, with the ever-increasing computational power, those complex problems could be solved using the powerful numerical techniques. Two numerical techniques, namely Finite-Difference Time-Domain (FDTD) and Finite Element Method (FEM), are the most widely used, due to their robustness and flexibility. In this thesis, two commercialized packages, Lumerical FDTD solutions (a commercial FDTD package) and COMSOL Multiphysics (a commercial FEM package), are employed.

1.4.1 Finite Difference Time Domain

The main concept of the FDTD method is to numerically solve Maxwell's equations based on the finite-difference approximation in time domain for the user-defined problems [43–46]. In other words, FDTD method evolves the electric and magnetic fields by iterating Maxwell's equations in small time steps. The simulation region usually contains a light source, which emits a pulse over the frequency range of interest. In FDTD algorithm, the electric and magnetic fields are updated at alternating time steps until a steady state is obtained. Therefore, FDTD algorithm could provide intuitively the process of how the light interacts with a device, as compared to other numerical techniques. The fields are recorded as a function of the time by monitors. The corresponding results in the frequency domain could be easily extracted via performing a Fourier transform on the recorded data.

There are several significant advantages to this technique. First, FDTD benefits for modelling complicated structures with a large volume. Second, being a time domain method, this method is able to simulate the transient response of devices, and calculate broad band frequency response in a single simulation. Third, non-linear behaviours, such as second harmonic generation, can be easily incorporated into this method. These advantages make FDTD one of the easiest and the most widely used technique in the computation of modern optics.

The disadvantages of FDTD are as follows: First, it is difficult to resolve curved surfaces, because the structured grid is usually applied in the method. This structured grid is also very inefficient, especially in the cases that very fine features are contained in the simulation region. In this situation, the small grid needs to be within the whole simulation region to resolve the fine features, even though those features is localized. Second, it would be very time consuming to simulate the response of structures with a strong resonance, since a steady-state solution is difficult to be found in those cases. Third, it is difficult for this method to handle problems with strong dispersion. This is because a continuous function needs to be fit to describe the optical constant of the materials involved.

1.4.2 Finite Element Method

As a famous alternative to FDTD, FEM is frequenclty used in the frequency domain. The concept of FEM is to numerically solve boundary-value problems by discretizing the geometrical domain into a set of sub-domain elements and generating the corresponding boundary conditions [47, 48]. A set of linear equation, thus, is established by applying the differential equation to each sub-domain element. Finally, the fields are calculated, when the global matrix for the whole system is solved. Such method contains those sub-domain elements, namely the finite element, hence its name. It should be noted that meshing structure is a very important and involved step in this method.

The following advantages distinguish FEM from other numerical techniques. First, in FEM both structured (such as cuboids and rectangles) and unstructured (such as tetrahedrons and triangles) grids could be applied to discretize the geometrical domain. This is very important, because the unstructured grid is highly efficient to resolve the curved surfaces and fine features without significant improvement of the computational time. Second, FEM could provide more accurate solution than FDTD. This is because the fields in each grid are calculated directly without any post-process, and the permittivity or refractive index of the materials at each single frequency should be given without any approximation. Another appeal of FEM is that it is very efficient to simulate the resonance response.

However, there are also some drawbacks in FEM. First, because FEM is a frequency domain method, sweeping across the range of interested frequencies is necessary to calculate a spectrum. Simulating a response over a broad range of frequencies would therefore be very time consuming. Second, it would very difficult to incorporate the non-linear response into the FEM simulation. Third, although FEM is more flexible than FDTD method, the computation time using FEM would increase faster when degrees of freedom of increases.

Table 1.1: Comparation between FDTD and FEM. "✓" means good performance, while " × " represents bad performance.

	Curved Surfaces	Strong Dispersion	Strong Resonance	Spectrum
FDTD	×	✓	×	✓
FEM	✓	×	✓	×

In general, FEM and FDTD method are two complementary techniques in computational optics as Table 1.1 shows. In this thesis, I usually use both for the validation of the results. However, FEM is used more to reduce the computation time and to obtain accurate results, because the strong resonance response of devices is stimulated in most case.

1.5 Organization of Thesis

In Chapter 1, we provide an general introduction of the theoretical description of the light-matter interaction and plasmonics. Starting from the dielectric theory, we summarize the main conclusions of Maxwell's equations and derive the classical models for the permittivity and permeability of materials in the response of electromagnetic radiation. Then, we present the famous dispersion relation of SPPs at a single interface and report briefly their most important properties. Lastly, we describe briefly and compare the working principles of numerical simulation approaches (the finite-difference time-domain method and finite-element method) heavily used in this thesis.

In Chapter 2, we summarize the drawbacks of the traditional SPPs, and introduce the new materials with plasmon-like behaviour. In this chapter, the properties of graphene (as an example of two-dimensional materials) and SiC (as an example of polar dielectrics) are then presented, which establishes the theoretical background of the thesis.

In Chapter 3, we focus on a simple model of a graphene plasmon cavity based on a system including a graphene layer sitting on a SiC grating. We investigate hybrid modes excited and the coupling between the SPPs in graphene and SPhPs in SiC. A simple Fabry-Pérot model is established to explain the results, in which a commonly used dispersion relation of GPs is used. Finally, a preliminary model was set up in this chapter.

In Chapter 4, we investigate the cavity height dependence of the dispersion relation of GPs by deriving an analytical expression for the dispersion relation of graphene plasmon waves in a multilayer system. We verify the precision of this dispersion relation by comparing its prediction and the numerical simulation results. The vertical optical property of the cavity is also investigated and anther Fabry-Pérot model is used to interpret the phenomenon of complete absorption. We also study the tunability of geometric parameters of cavities and the Fermi energy, which make for flexible system design. High enhancement and extraordinary compression of graphene plasmon waves are also demonstrated.

In Chapter 5, we study a system in which a graphene film is suspended above a SiC grating with a small gap. We apply the height dependence of the dispersion relation derived in Chapter 4 to study the optical properties of this suspended graphene plasmon cavities. A modified Fabry-Pérot model is used to elucidate the observed phenomena. What is the most important is that we try to realize the simultaneous implementation of extremely high enhancement and extraordinary compression, which would be powerful for potential applications.

In Chapter 6, we summarise the thesis with some general conclusions and propose some possible prospects for future researches based on our current results.

CHAPTER 2

New Materials with Plasmon-like Behaviour

2.1 Overview

Due to the use of metallic materials, traditional SPPs have some drawbacks, such as the high Ohmic loss. In order to overcome these shortcomings, many other materials have been studied. It is found that when the permittivity of these materials presents a negative real part, they will exhibit plasmon-like behaviour. In this chapter, we will discuss two new materials: graphene and polar dielectrics. In comparison with tradition SPPs on metals, both of these new materials have some advantages. For example, they are low loss and operate at the mid-infrared frequencies, thus significantly enlarging the working frequency range of plasmonic waves. This chapter will provide the necessary theoretical basis for presenting the principle and the applications of graphene plasmon cavities.

2.2 Graphene

As an allotrope of carbon, graphene consists of a mono-layer of carbon atoms arranged in an atomic-scale hexagonal lattice as shown in Figure 2.1. Since the experimental discovery of graphene in 2004 by Geim and Novoselov [49], graphene has become one of the hottest research topics in nano-science and technology [35,50–56], thanks to its extraordinary properties. Graphene is the first truely two-dimensional material that was experimentally obtained. Due to the atomic thickness, graphene layers support unprecedented mechanical, electronic and optical behaviours [57–63]. For example, graphene is regarded as the strongest material ever produced, exhibits excellent thermal conductivity [64–66]. Nevertheless, the real miracle of graphene can indeed be observed in electrical and optical fields.

Graphene can be modeled as a 2D continuous sheet charaterized by its in-plane electrical conductivity σ_g based on the Kubo formula within the local random-phase model [50, 68, 69], which ignores that the response is dependent on the wavevector and assumes that the electronic system is controlled by the average potential. Such conductivity can be expressed as $\sigma_g =$

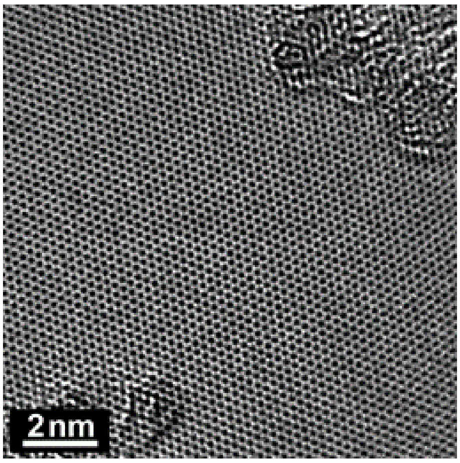

Figure 2.1: High-resolution transmission electron microscopy image of graphene. Reprinted from [67].

$\sigma_{intra} + \sigma_{inter}$, where σ_{intra} and σ_{inter} refer the contributions from the intraband and interband transitions of electrons in graphene, respectively. In this way, both contribuitons are given by [70]

$$\sigma_{intra} = \frac{8i\sigma_0 k_B T}{\pi\hbar(\omega + i/\tau)} \ln\left[2\cosh\left(\frac{E_F}{2k_B T}\right)\right], \tag{2.1}$$

and

$$\sigma_{inter} = \sigma_0\left[\frac{1}{2} + \frac{1}{\pi}\arctan\left(\frac{\hbar\omega - 2E_F}{2k_B T}\right) - \frac{i}{2\pi}\ln\left(\frac{(\hbar\omega + 2E_F)^2}{(\hbar\omega - 2E_F)^2 + (2k_B T)^2}\right)\right], \tag{2.2}$$

where $\sigma_0 = e^2/(4\hbar)$, τ is the carrier relaxation time and is linked to the carrier mobility μ via the equation $\tau = \mu E_F/(ev_F^2)$, E_F is the chemical potential (or Fermi level), k_B is the Boltzmann constant, T is the temperature, $\hbar$ is the reduced Planck's constant, and all other symbols have their usual meaning. It should be noted that the intraband transition term is Drude-like, with the term $1/(\omega + i/\tau)$. Furthermore, within the low electronic-temperature approximation ($E_F >> k_B T$), we can reduce Equations (2.1) and (2.2) to the following forms

$$\sigma_{intra} = \frac{4i\sigma_0 E_F}{\pi\hbar(\omega + i/\tau)}, \tag{2.3}$$

and

$$\sigma_{inter} = \sigma_0\left[\Theta(\hbar\omega - 2E_F) + \frac{i}{\pi}\ln\left(\left|\frac{\hbar\omega - 2E_F}{\hbar\omega + 2E_F}\right|\right)\right], \tag{2.4}$$

where Θ is a step functions with two possible values (when $\hbar\omega - 2E_F < 0$, it is 0, while when $\hbar\omega - 2E_F > 0$, it is 1). Indeed, these equations are for the zero-temperature limit.

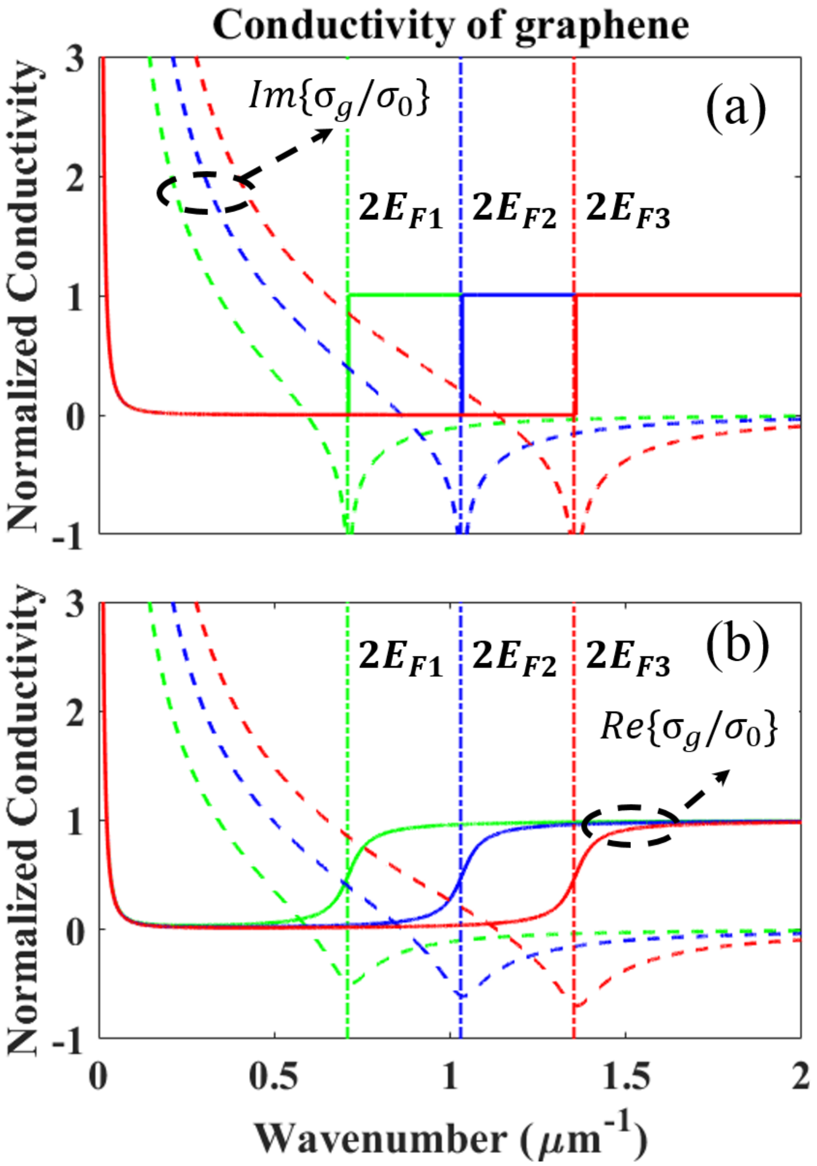

Figure 2.2: Normalized conductivity of graphene: (a) is for the zero-temperature limit, (b) corresponds to a temperature of $300K$. The solid lines denote the real part of the normalized conductivity, while the dashed lines denote the imaginary part. The vertical dash-dot lines are used to mark the double Fermi energies. Three Fermi energies are reported here and are represented by three colors: $E_{F1} = 0.44eV$ (green), $E_{F2} = 0.64eV$ (blue), and $E_{F3} = 0.84eV$ (red).

Figure 2.2 shows the normalized conductivity (σ_g/σ_0) of graphene under different doping conditions. Both the zero-temperature approximation and a temperature of $300K$ are reported. According to Equations (2.1) and (2.2), the conductivity is dominated by the intraband contribution in the frequency band $\omega < 2E_F$. Both the real part and the imaginary part of the normalized conductivity are positive and increase with the decrease of the frequency. The interband contribution dominates the conductivity when $\omega > 2E_F$. The imaginary part of the normalized conductivity becomes negative, and there is a saturation of the real part. Within the boundary region (the region where the frequency is close to $2E_F$), the real part of the normalized conductivity exhibits the step-like behaviour, while the imaginary part changes the sign. When the zero-temperature limit is considered, the step-like behaviour is sharper.

We also can describe graphene using a three-dimensional model, first proposed by Vakil and Engheta [71]. In this model, grahene is considered as a layer with a finite thickness, δ. Such layer can be described by an effective bulk conductivity, $\sigma_G = \sigma_g/\delta$. When the thicknesses are small enough (usually smaller than $0.5nm$), the simulation results using the two-dimensional model are the same as those using the three-dimensional model and agree with the experimental results. Hence, an effective permittivity can be introduced to describe the graphene layer

$$\epsilon_G = 1 + \frac{i\sigma_G}{\epsilon_0 \omega} = 1 + \frac{i\sigma_g}{\epsilon_0 \omega \delta}. \tag{2.5}$$

Figure 2.3b shows the effective permittivity of graphene when $\delta = 0.5nm$ is considered. We find that the real part of the permittivity is negative indicating that graphene acts like a metal, when the frequency is smaller than the boundary frequency ($2E_F$). So there is no surprise to find that GPs exist in this spectral region. One excellent feature of graphene is that its palsmonic resonance can be readily tuned through external gate voltage [72–76]. Furthermore, when $1.667E_F < \omega < 2E_F$, the permittivity becomes extremely high. Indeed, weakly bound TE modes can be supported by the graphene layer, due to the existence of TE guided modes in a dielectric slab [77].

In Figure 2.3a and b, we plot the conductivity and permittivity of graphene under three different doping conditions. In this thesis, $E_F = 0.64\ eV$ and $\mu = 10000\ cm^2/(Vs)$ (which is a typical maximum value for the carrier mobility of chemical-vapor-deposition-grown graphene) are used unless otherwise stated. Figure 2.4 shows the corresponding absorption. It can be seen that a monolayer of graphene suspended in the air has a remarkably large absorption at visible wavelengths. Despite single layer graphene being atomically thin, the absorption can reach 2.3%, which is a significant fraction of the incident white light. Such extraordinary performance results from the unique electronic structure of graphene [78].

2.3 Graphene Plasmonics

As mentioned, SPPs arise due to collective oscillations of free charge carries in conductors [1,39] and have attracted significant interest for overcoming the diffraction limit [6,9]. The emeregence of graphene brings new features for plasmonics [33,50,79–81].

Compared to the traditional SPPs, GPs possess the following significant advantages: First, SPPs at the dielectric-metal interface have a short life time and mainly exist at the visible and near

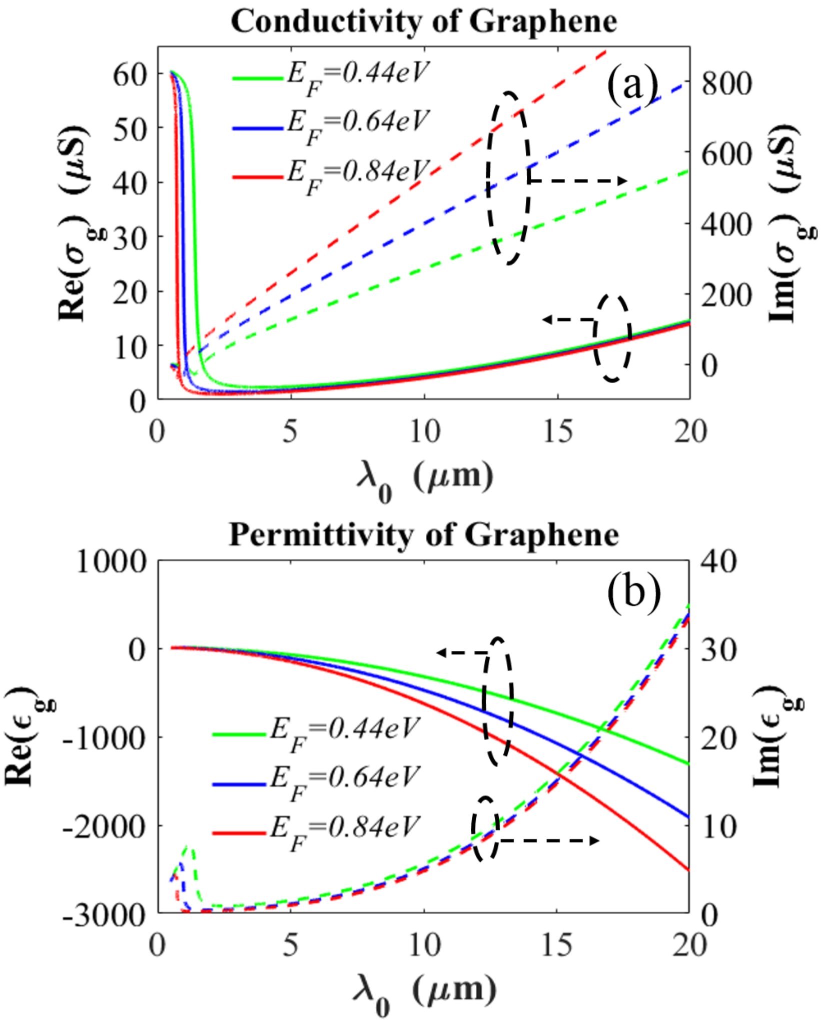

Figure 2.3: Properties of graphene used in this thesis: Real and imaginary parts of the conductivity (a) and permittivity (b) of graphene under different doping conditions are represented by solid and dashed lines. In this thesis, $T = 300K$ and $\mu = 10000cm^2/(Vs)$ (thus, $E_F = 0.64eV$) are used unless otherwise stated.

infrared frequencies. Thanks to the low carrier concentration, GPs are relatively long-lived and exist at lower frequencies (covering the mid-infrared to terahertz frequencies) [34, 82–85]. Second, GPs have very short wavelengths and exhibit extremely high confinement [86–88], because of the two-dimensional nature of graphene. Third, and the most important, the carrier concentration can be precisely controlled by electrical gating and/or surface doping to permit the existence of GPs along the sheet [33, 83]. These strongly confined, long-lived, easily tunable GPs make graphene a very promising plasmonic candidate at terahertz to mid-infrared frequencies [70, 88].

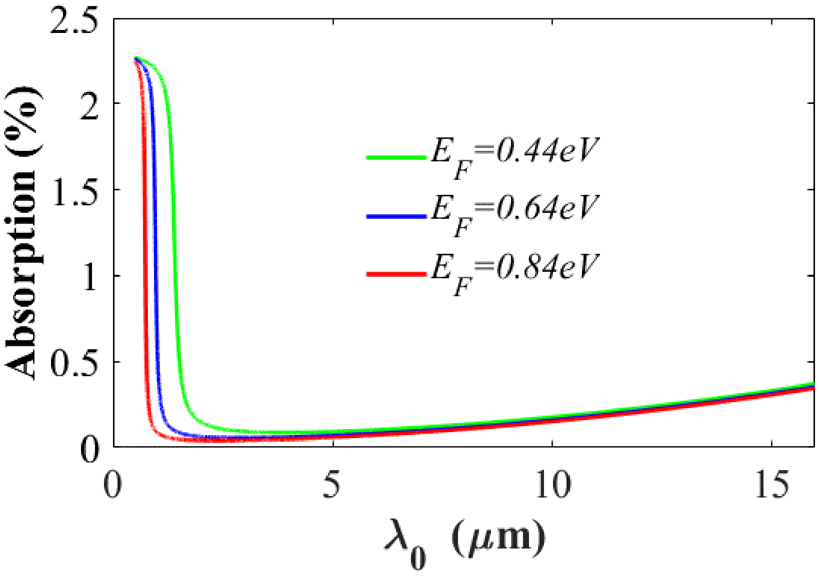

Figure 2.4: Graphene absorption under different doping conditions. The graphene is suspended in air.

Figure 2.5 shows the configuration of the system which consists of two semi-infinite spaces and a graphene layer at the interface. Similar to the derivation process for the dispersion relation of SPPs on metal-dielectric interfaces, the dispersion relation of GPs can be deduced by considering the TM solutions on the mentioned system. The field components can be written in the same form as the ones in Equations (1.30) to (1.35). However, due to the existence of the graphene layer, the boundary conditions read

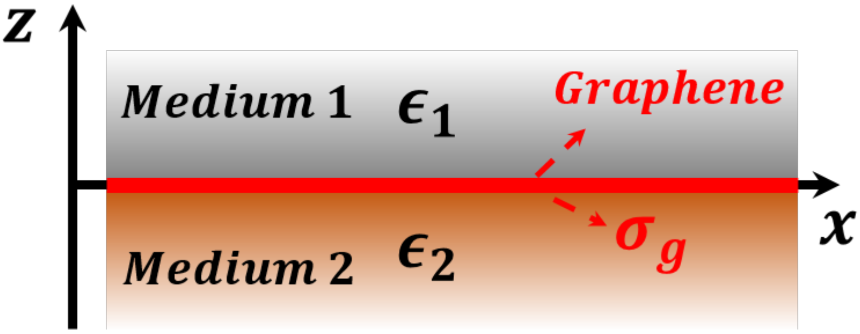

Figure 2.5: Configuration of a single interface system for graphene plasmons: There exist two semi-spaces. The system consists of two media in the upper and lower semi-spaces and a graphene layer between them characterised by a complex surface conductivity σ_g. ϵ_1 and ϵ_2 denote the permittivities of the media. The system is homogeneous in the y-direction.

$$E_x^1 = E_x^2, \tag{2.6}$$

$$H_y^1 - H_y^2 = -\sigma_g E_x^1, \tag{2.7}$$

Solving the linear equations results in the following relation

$$\frac{\epsilon_1}{k_{z,1}} + \frac{\epsilon_2}{k_{z,2}} + \frac{i\sigma_g}{\epsilon_0 \omega} = 0, \tag{2.8}$$

where ϵ_1 and ϵ_2 represent the permittivities of the media above and below the graphene layer. This is a general form of Equation (2.8) to the situation where a surface current density exists at the interface between two media. Equation (2.8) is equivalent to Equation (1.41) when a dielectric and a metal are considered in the system with $\sigma_g = 0$. Because Equation (2.8) is an implicit equation for ω and β, we should apply numerical approaches to obtain the relationship between the wavevector and the frequency. To reveal the physics behind the equation, an analytical expression is presented by assuming the non-retarded limit ($\beta >> \sqrt{\epsilon}\omega/c$)

$$\beta \approx i\frac{\omega(\epsilon_1 + \epsilon_2)\epsilon_0}{\sigma_g(\omega)}. \tag{2.9}$$

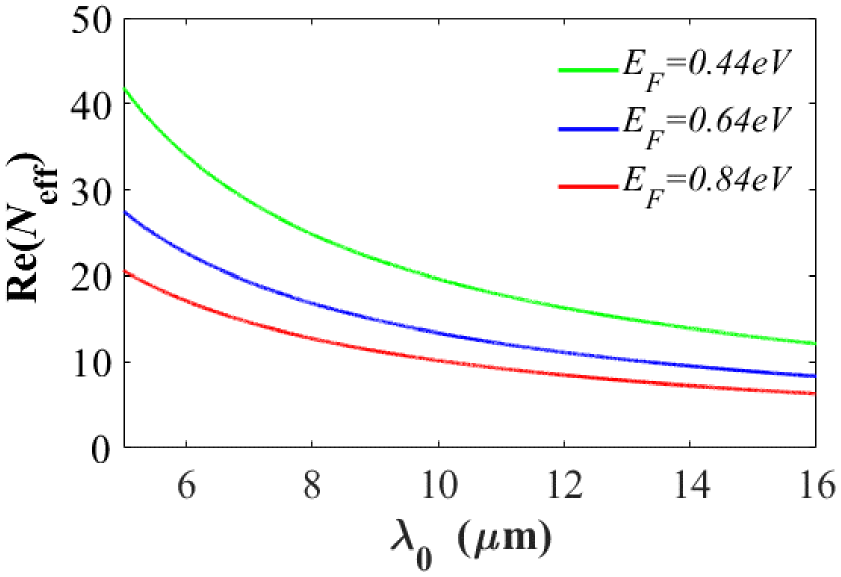

Figure 2.6: Dispersion Relation of Graphene Plasmonics. The system has a single layer of graphene suspended in the air, which means $\epsilon_1 = 1$ and $\epsilon_2 = 1$. Three doping conditions are presented here for comparison.

For the cases chosen ($E_F = 0.64\ eV$ and $\gamma = 1\ meV$) in this thesis, the prediction with the non-retarded approximation works extremely well. Indeed, when large doping cases are considered, the retardation effects can usually be neglected. The in-plane wavevector of the GP, β, is a complex number with the real and imaginary parts determining the GP wavelength, $\lambda_{spp} = 2\pi/Re\{\beta\}$, and the propagation length, $L_{spp} = 1/(2 \cdot Im\{\beta\})$. To investigate the properties of GPs, the effective refractive index (ERI) of the GP defined by the following equation is used

$$N_{\text{eff}} = \beta/k_0. \tag{2.10}$$

In Figure 2.6, we show the dispersion relation of GPs calculated from Equation (2.9). In the previous works, Equation (2.9) is the most commonly used dispersion relation. However, the assumption here is that the upper and lower spaces are infinite, which is usually not possible in reality. This will be discussed later and is one focus of this thesis.

2.4 Phonon Polaritons in Polar Dielectrics

In the first chapter, we introduce the first kind of polaritons – plasmon polaritons. In this section, we bring another kind of polaritons – phonon polaritons. This kind of polariton results from the coupling of the electromagnetic field to the collective lattice vibrations of polar dielectrics at infrared frequencies [1, 89]. Here, the lattice vibrations of polar dielectrics are called phonons. When the crystal consists of more than one kinds of atoms, there exist vibrational modes that can be stimulated optically (because of the energy scale of optical phonons), and hence the name of optical phonons. All optical phonons can be categorize into two types in terms of the relation between the vibrational direction and the wave vector: One is called longitudinal optical (LO) phonons and the other one is called transverse optical (TO) phonons. Figure 2.7 shows the illustration of each type of phonon mode. One can find that in both modes, the movements of the neighbouring atoms have opposite directions. SPhPs, similar to SPPs, are the phonon polaritons that only exist at the interface between the dielectric and the polar dielectric. Certainly, the SPhP modes provide the ability of the confinement of light.

For polar dielectrics, there is a frequency window, referred to as the Reststrahlen band, bound by the LO and TO phonon frequencies. Within the Reststrahlen band, polar dielectrics act simliar to an optical metal however with lower optical losses due to the long phonon lifetime [90], as compared to their plasmonic counterparts. The dielectric function for polar dielectric crystals can be well described using a Lorentz oscillator model as follows

$$\epsilon(\omega) = \epsilon_\infty \left(1 + \frac{\omega_{LO}^2 - \omega_{TO}^2}{\omega_{TO}^2 - \omega^2 - i\omega\gamma}\right), \tag{2.11}$$

where ω_{LO} and ω_{TO} are the LO and TO phonon frequencies, respectively. SiC is a typical polar dielectric [90–94]. For SiC [95], we take the following values for the parameters: $\epsilon_\infty = 6.56$, $\omega_{LO} = 973\ cm^{-1}$, $\omega_{TO} = 797\ cm^{-1}$ and $\gamma = 4.76\ cm^{-1}$. Figure 2.8 shows the permittivity, the refractive index and the absorption of SiC. We find that the permittivity of a polar dielectric has a pole at the TO phonon frequency, and the value has a zero-point crossing at the LO phonon frequency. Within the Reststrahlen band, the real part of the permittivity is negative, resulting

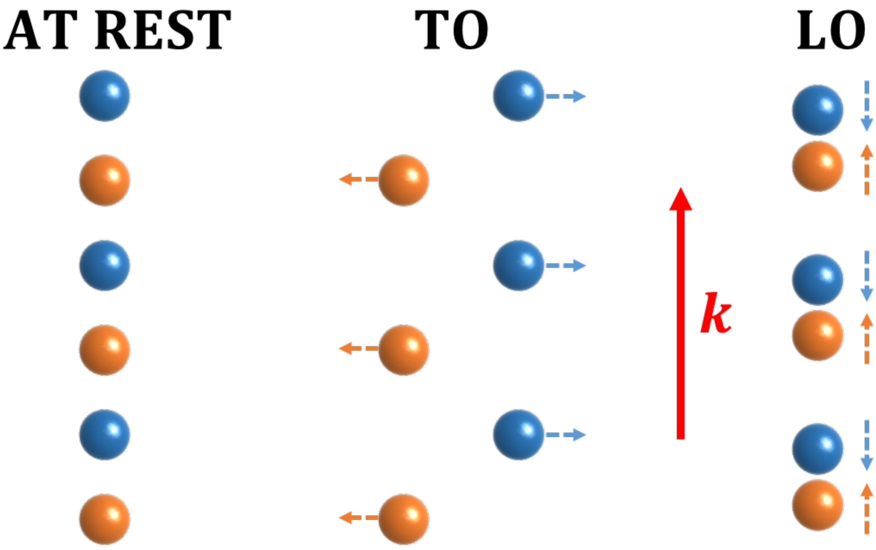

Figure 2.7: Schematic of longitudinal and transverse optical phonons: In this example, the system consists of a linear chain of two different types of atoms (represented by two different colors). The wave propagation direction is indicated by the red arrow. For longitudinal optical (LO) modes, the displacement direction of the adjacent atoms is parallel to the propagation direction, while for transverse optical (TO) modes, the adjacent atoms move perpendicularly to propagation direction. In optical phonons, the oscillations of adjacent atoms are out of phase.

in the strong reflection of incidence light. That is, SiC acts like metals within this band but without Ohmic losses because of the lack of the free charge carrier.

By comparing polar dielectrics and metals, we find that they all possess the negative real part of the permittivity due to one kind of particles. For polar dielectrics, the particles refer to atoms, while for metals, the particles are free electrons. Although the reasons for the negative real part of the permittivities are different, the optical performances are substantially the same. For this reason, the SPhPs could be recognized as an analogy of SPPs and they have the same behaviour. Thus, the expression form of the dispersion relations of SPhPs and SPPs is the same as Equation (1.41) shown. In Figure 2.9, the dispersion relation of the SPhPs of 4H-SiC is shown. The corresponding system consists of the air and SiC forming an interface between those two media. Similar to SPPs existing at the interface shown in Figure 1.4, SPhPs are confined at the air-SiC interface and are TM modes. Note that the SPhPs can only be supported in a relatively narrow spectral bandwidth (in the case of SiC around $176\ cm^{-1}$). This is because polar dielectrics only behave as metals within the Reststrahlen band, and are transparent to light outside of this band. Hence, there are three uncoupled dispersion branches formed at the whole frequency range: the upper branch, the bounded bounded branch and the lower branch. Not surprisingly, the upper branch represents the radiative modes with smaller wavevectors than the incident light, while the bounded branch represents the SPhP modes with larger wavevectors. However, when the

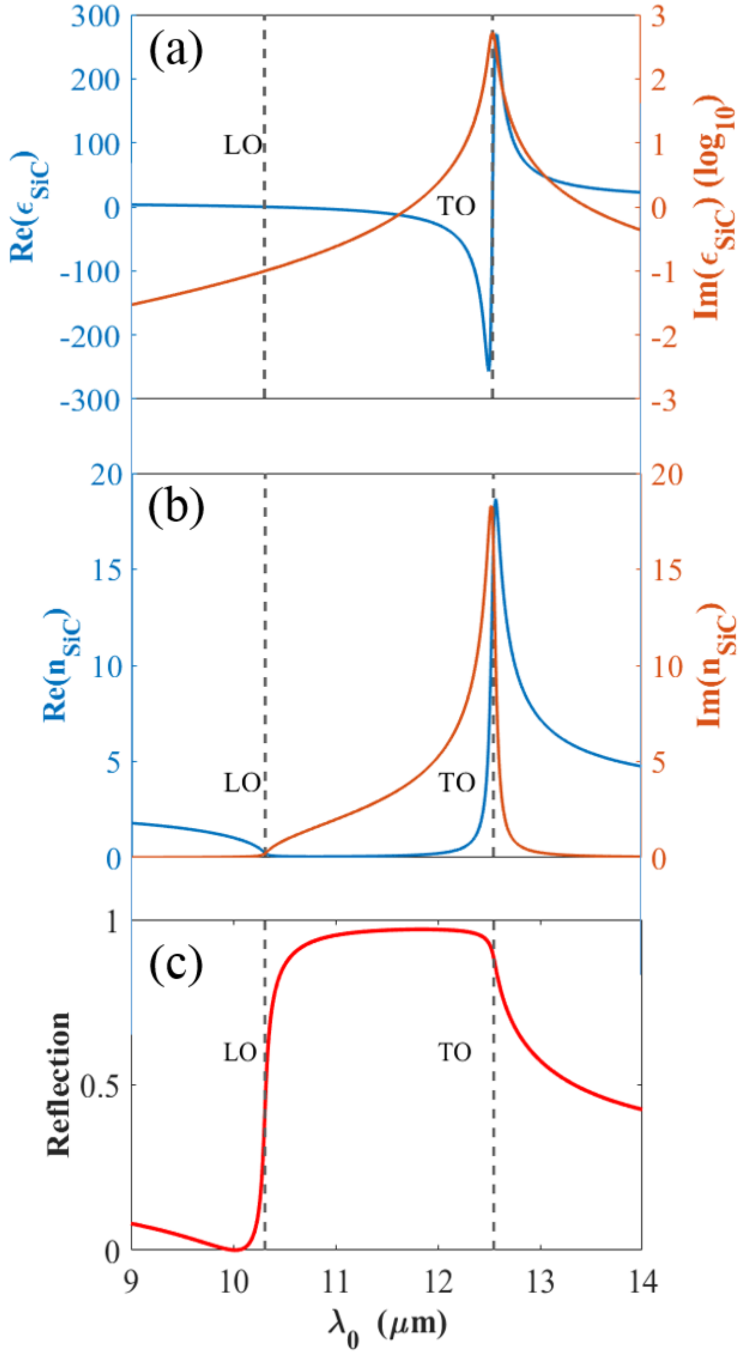

Figure 2.8: Material properties of bulk SiC. Real and imaginary parts of the permittivity (a), the refractive index (b), and the corresponding reflection (c) of bulk SiC are shown. The incident wavelength is in the range of $9\mu m$ to $14\mu m$, which is around the Reststrahlen band as the vertical line marks.. The absorption of a plain SiC substrate (within the Reststrahlen band) can be obtained via $1 - Reflection$, with an assumption that the substrate is infinite thick.

frequency is smaller than the TO frequency, the modes become the radiative modes as the same one represented by the upper branch.

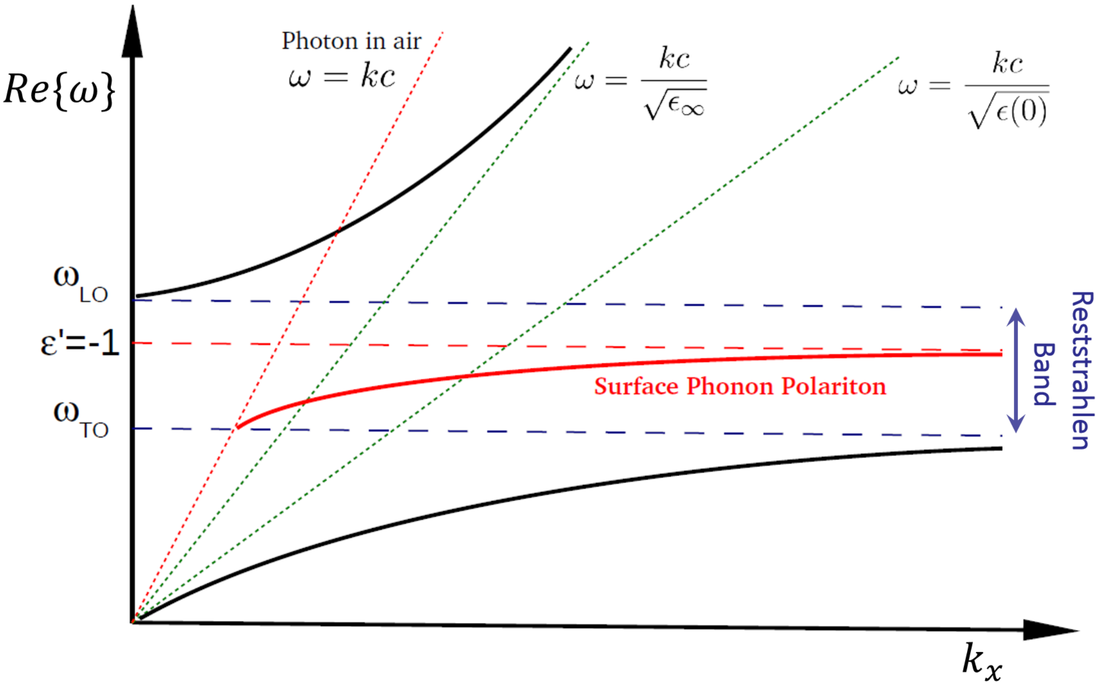

Figure 2.9: Dispersion relations of surface phonon polaritons for 4H-SiC. The black and red lines correspond to the bulk and surface phonon polaritons, respectively. The LO and TO phonon frequencies are represented by the dashed horizontal lines. Different dispersions of photons in different cases are are provided for comparison. $\epsilon(0) = \epsilon_\infty \frac{\omega_{LO}^2}{\omega_{TO}^2}$. It should be noted that this plot is obtained by considering complex frequencies and real wavevectors. More detail can be found in Reference [96].

In the Reststrahlen band, the polar dielectrics can achieve field enhancement and confinement at the interface via the SPhP modes, but with lower optical losses due to the long phonon lifetime [90], as compared to their plasmonic counterparts. More recently, active modulation of the permittivity (and consequently the SPhP resonances) in nanostructured SiC has been realized by using the coupling of photoinjected carriers and optical phonons [97], and by using phase change materials [98]. All of these advantages, as well as high thermal, mechanical and chemical stability, make SiC highly suitable for multiple applications in mid-infrared photonics. In addition, the coupling between the SPhPs of polar dielectrics and the GPs could exist in the Reststrahlen band, paving the way for interactions between the two types of excitations.

CHAPTER 3

Graphene Plasmon Cavities: A Simple Model

3.1 Overview

We have already introduced graphene and SiC in Chapter 2. On the one hand, doped graphene has been considered as an outstanding alternative to noble metals in plasmonics, because it can support plasmonic modes that are characterized by extremely large field confinement [87] and strong field enhancement. In addition, graphene SPPs can be easily tuned via chemical doping or electrical gating, which is particularly appealing in nanophotonics. These extraordinary properties of GPs make it possible to design cheap, reliable and ultrafast optical modulators using graphene. On the other hand, as a typical polar dielectric, SiC supports sub-diffraction confinement of light due to the excitation of SPhPs [90]. Thanks to the long lifetime of phonons in polar dielectrics (on the order of picoseconds), as compared to scattering lifetime of electrons in metals (10 to 100 femtoseconds), SiC can be used to design systems with low loss, high quality factors and narrow linewidths [90]. Previous studies show that localised SPhPs with strong field confinement exist in nanostructures of SiC [99, 100]. In addition, SiC can be used in a number of applications due to its high thermal, mechanical and chemical stability.

We are particlularly interested in the coupling between localised SPhPs in SiC and SPPs in graphene. Such coupling can result in hybrid modes [101] which combine the advantages of both constituent modes - large light confinement and tunability of graphene SPPs and low loss of SiC SPhPs. In this chapter, we will focus on a simple model of graphene plasmon cavities, in which we apply the most commonly used assumptions (which will be discuss in the next section and in Chapter 4) and consider the simplest structure. As shown in Figure 3.1, the system contains monolayer graphene on top of a SiC cavity. It should be borne in mind that we consider the cavity as part of a grating. This is because a grating is convenient for fabrication and simulation. The scattering from the edges of the SiC cavity (rather than the grating diffraction) provides the necessary momentum mismatch between the incidence and SPPs of graphene. A numerical investigation of this system in the mid-infrared is reported. Within the Reststrahlen band, the SiC behaves like a perfect conductor. Plasmonic standing waves are formed at certain grating groove lengths, which can be well explained using a simple Fabry-Pérot model. This setup provides a simple way to efficiently excite localised graphene SPPs, and to realize strong absorption without using widely used structures such as nanoribbons.

Strong-coupling is a hot topic in modern physics. If two subsystems couple strongly, two new hybrid modes (as the eigenmodes of the new system) emerge, due to the qualitative modification of the dynamics. We can find a characteristic anti-crossing which appears in the frequency domain. This splitting is also known as Rabi splitting. Therefore, whether such splitting is visible can be used as the definition of strong-coupling [102]. The coupling of surface phonons and GPs has attracted wide attention [103–105]. This is particularly important at the mid-infrared band for typical polar dielectric substrates, such as SiC [106, 107] and SiO_2 [108–110]. Previous studies have already demonstrated this in graphene/h-BN heterostructures [87, 111–114], and surface absorbed polymers [115]. Recently, the strong-coupling between phonon-polaritons in a SiO_2 coating and localised plasmons in a gold antenna has been explored, and it is found that the splitting leads to a transparency window [116]. In addition, there is a lot of interest in the strong interaction of light and individual emitters. However, it is very challenging to achieve such strong-coupling in experiments. To overcome this challenge, we can appeal to two main approaches: First, cavities with high quality factor Q can be used. This is because light needs to travel many times in such cavities to acquire a high quality factor, and hence the interaction between light and the emitters can be boosted in this process. This approach often requires that the loss in both the cavity and emitter is small. Therefore, dielectric cavities and cryogenic temperatures are usually employed in this approach [117, 118]. Another approach is to minimize the effective volume V of cavities, so that the size mismatch between light and individual emitters can be compensated. SPPs are usually applied in this approach, because plasmons can be used to overcome the diffraction limit and to concentrate the electric field in small hot spots [119]. The strong field confinement and enhancement can also boost the interaction between light and matter. Both approaches have advantages and disadvantages: dielectric cavities often have a high quality factor but with weak field confinement. Plasmons can be used to achieve strong field confinement, but its quality factor is very low because of the high loss. Thus, the ratio of Q/V is usually used to qualify the strength of the interaction.

In this chapter, we will also study the strong-coupling between the localized SPhPs in SiC and the SPPs in graphene around the LO phonon frequency. We find that a Rabi splitting appears due to this coupling, which indicates that there is a coherent energy transfer between the two original systems [120]. In addition, we combine the two mentioned approaches together to boost the value of Q/V. This work offers a possibility to effectively excite coupling modes with confinement and manipulation of light, and pushes the potential for enhanced, broadly tunable spectroscopy into the mid-infrared and terahertz range [95]. In addition, high quality factor and small modal volume make the system very suitable for inducing and exploring the strong interaction between light and matter.

The Fabry-Pérot model in this chapter was established by myself. The simulation results discussed in this chapter were obtained by Dr Ke Li and myself. The theoretical analysis was performed by Jamie M Fitzgerald and myself. The materials discussed in this chapter was previously published [121]. The figures in this chapter are either reproduced or adapted from this publication, with permission granted by the American Chemical Society.

3.2 System Setup and Theory

The system we considered in this chapter is shown in Figure 3.1. It is composed of a single layer of graphene suspended on and in contact with a SiC grating. The grating has a periodicity in the x direction. The meaning of parameters are shown in the caption of Figure 3.1b. In order to excite the SPPs of graphene, a TM incidence propagates in the y direction from air and is normal to the surface of the structure. In this simulation, the graphene thickness is $0.5\ nm$, which we have checked is converged for all results. All other simulation conditions, including the details of the model for graphene, can be found in Chapter 2.

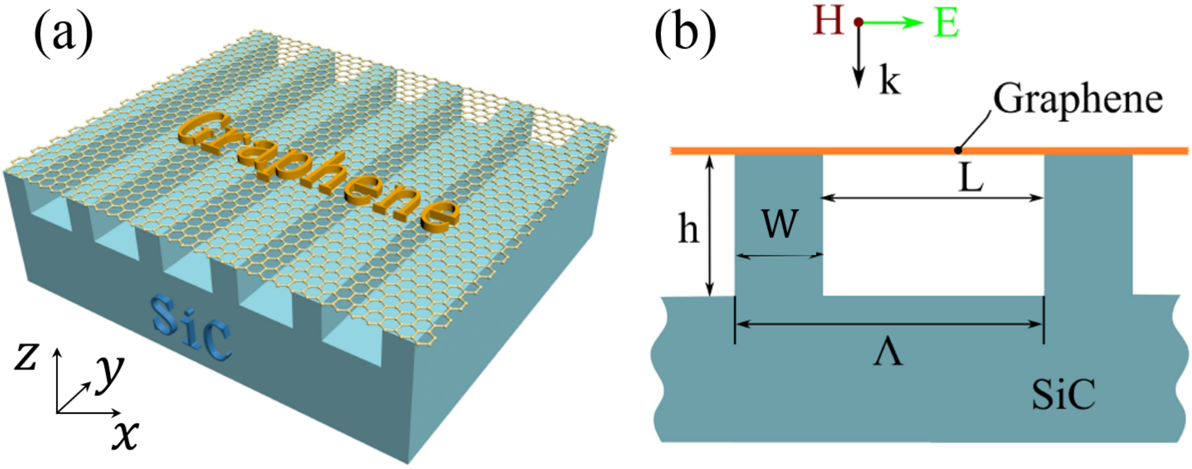

Figure 3.1: Schematics of the SiC-graphene plasmonic system. (a) Three-dimensional view and (b) cross-sectional view of the structure. The geometrical parameters of the system are as follows: Λ is the grating period, W is the width of the grating ridge, L is the width of the grating groove, and h is the grating height. The illumination is TM polarized as shown in (b) and is normal incident from the air.

Despite the impressive advantages of SPPs in graphene, efficiently exciting these plasmonic waves is still challenging due to the large momentum mismatch between the incident light and GPs. Grating coupling [122, 123] (GPs are excited by diffraction effects owing to the grating periodicity), cavity coupling [121, 124] (localized cavity modes are excited by scattering of cavity ridges), near-field coupling [36, 125–127], and excitation by scattering of random structures [128] are widely used schemes to achieve phase matching. Among them, grating coupling and cavity coupling are convenient because, as well as assisting the coupling between excitations and incident light, these structures also can be used as a gate electrode to tune the resonance frequency over a wide spectral range, allowing the system to act as a very tunable optical filter. We apply the commonly used assumptions that interband transitions can be ignored (see Equation (2.3)) and that the zero-temperature limit is considered (see Equation (2.9)). Then, we can obtain the dispersion relation of the plasmon waves [33, 86, 121, 122]

$$\beta = \frac{\pi\hbar^2\epsilon_0(\epsilon_1+\epsilon_2)}{e^2E_F}\left(1+\frac{i}{\omega\tau}\right)\omega^2. \tag{3.1}$$

Equation (3.1) means that a monolayer graphene is sandwiched between two infinite half-spaces with the relative permittivities ϵ_1 and ϵ_2. The wavelength of GPs against with the incident wavelength is plotted in Figure 3.2a for a graphene sheet in vacuum ($\epsilon_1 = 1$ and $\epsilon_2 = 1$) with various doping levels. These curves demonstrate that the wavelength of GPs is on the order of 10-100 times smaller than the wavelength of the incidence, which indicates the strong field confinement ability of graphene. This also leads to the huge momentum mismatch between the incidence and the GPs which demonstrates the challenges in efficient coupling. Unless otherwise stated, the Fermi energy is set as $0.64\ eV$ throughout this chapter. It should be noted that β will be written as k_{spp}. In this thesis, β will be used when we derive the dispersion relations, while k_{spp} or k_{spp}^h will be used when such relations are used to build models. This does not change any physics involved.

3.3 Optical Properties of a SiC Grating

The absorption is applied to investigate the optical properties of the system. In this section, we numerically calculate the absorption in different structures. Unless otherwise stated, we fix the grating height and the width of the grating ridge to be $1\ \mu m$ throughout this chapter. In the following, the change in the cavity length is equal to the change of the grating period. The structures studied here can be divided into two classes, the bare SiC structure and the SiC-graphene structure. In the simulation, the SiC substrate is assumed to have infinite thickness below the grating to switch off the transmission channel of the system and simplify analysis. We consider the incidence with wavelengths in the range of $10\ \mu m$ to $14\ \mu m$ and grating periods in the range of $1.1\ \mu m$ to $5\ \mu m$, respectively.

We begin by studying the bare SiC grating without the graphene layer and numerically calculating its absorption as shown in Figure 3.2b. In comparison with the plain SiC case (we could get

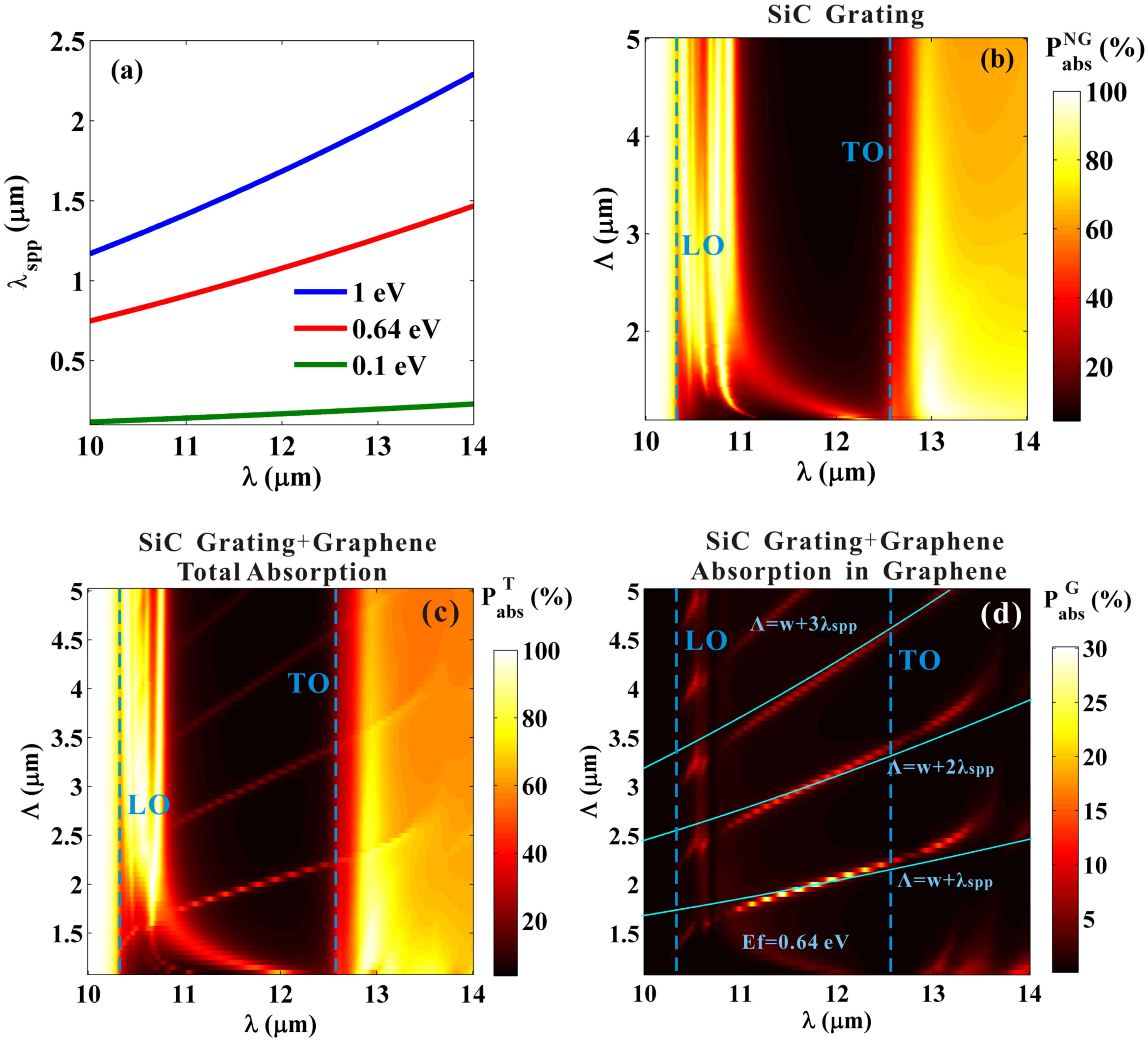

Figure 3.2: (a) The wavelength of graphene SPPs for various Fermi energies. (b) Total absorption (P^{NG}_{abs}) versus grating period (Λ) and excitation wavelengths (λ) for a bare SiC grating (with no graphene layer) structure. (c) Total absorption (P^{T}_{abs}) versus grating period and excitation wavelength for the SiC-graphene structure. (d) Graphene layer absorption (P^{G}_{abs}) vs grating period and excitation wavelength. The system is the same as the one in (c). A fit to a simple Fabry-Pérot model for a phase shift of $-\pi$ (see Equation (3.2)) is indicated by the blue curves. The other geometrical parameters of the system are fixed as follows $W = h = 1\ \mu m$.

the absorption of the plain SiC using $1 - Reflection$ as shown in the bottom of Figure 2.8), there exist a number of peaks within the Reststrahlen band when the SiC grating is considered. This is because the existence of the grating allows the excitation of SPhPs in bulk SiC [100]. We observe that there is a region in which large absorption occurs and the frequencies are close to the LO frequency. However, above this region but within the Reststrahlen band the absorption is very low, because in this region the SiC acts as a perfect reflector and absorbs low energy. Outside the Reststrahlen band, where the frequencies are larger than ω_{LO} and less than ω_{TO}, the SiC grating has behaviour similar to a plain SiC surface which can be found in Figure 2.8.

3.4 Excitation of Plasmonic Standing Waves

Now we focus on the SiC-graphene structure, in which a graphene layer is added on top of the grating. Two relevant quantities are considered here: the total absorption (sum of the absorption of the SiC grating and the graphene layer), P_{abs}^{T}, shown in Figure 3.2c, and the absorption in graphene layer, P_{abs}^{G}, shown in Figure 3.2d. As compared to the bare SiC grating case, the most striking difference here is that strong absorption peaks appear in the previously low absorbing region of the Reststrahlen band. Such high absorption peaks occurs only for certain grating period lengths, so we could take a guess that they are related to the standing waves. The similar behaviours of these peaks as shown in Figures 3.2c and d suggest that they exist in the graphene layer. These guesses can be confirmed by looking at the near field plots as shown in Figure 3.3. The modes are excited at integer numbers of L/λ_{spp}, and the electric field is concentrated in the graphene sheet in the region directly over the air. We also find that plasmon modes are antisymmetric (we refer to the z-component of the electric field). This can be understood by noted that SiC behaves like a perfect conductor within the Reststrahlen band, which can screen out the electric fields very efficiently at the boundaries. Therefore, the z-component of the electric field is forced to be fully reflected and the phase is put to zero at the boundaries. The normal incidence excites graphene plasmonic waves at the edge which are out of phase, and only odd modes will be formed by constructive interference [129]. To confirm this, the absorption with different cavity lengths (for a fixed wavelength $\lambda = 12\ \mu m$) and the near field plots for each peak are shown in Figure 3.3. It can be seen that each peak in the absorption corresponds to the antisymmetric plasmonic modes. Figure 3.4 shows the illustration of plasmonic standing waves. Of course, the symmetric plasmonic modes can be generated when the oblique incidence exists (because the oblique incidence will break the symmetry of the system), which will be mentioned in the next chapter. It should be noted that there is a very weak field (consequently low absorption) in the regions of the graphene layer located at the top of the SiC. This is still because that for this frequency the SiC behaves like a perfect electric conductor and can screen out any external field very effectively. As a result, the plasmon standing waves are established in the cavity, and the parts of the graphene layer located at the top of the SiC have no effect on the optical behaviour reported here. In other words, the graphene layer can be replaced by graphene ribbons that only cover the cavity, and the phenomenon and the explanation are the same as the ones shown here. The near field in Figure 3.3 also reveals another feature that a small peak located near $L/\lambda_{SPP} = 0$ exists. This is a localised SPhP mode that can also be visible without graphene (see Figure 3.2b). Its appearance is due to near-field coupling between the two SiC slabs when the cavities is small enough.

We emphasis again that the excitation of the graphene plasmonic modes is not due to diffraction of the grating. The mismatch of the momentum between the plasmon modes and the incidence

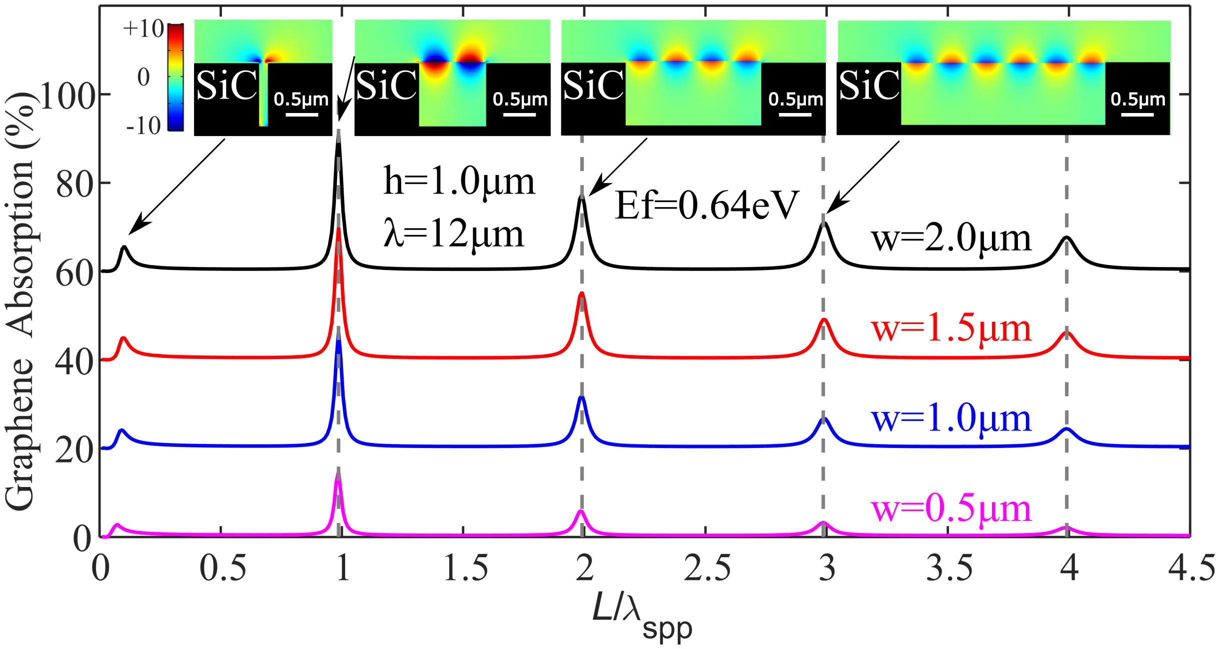

Figure 3.3: Absorption of graphene layer against different geometrical parameters L/λ_{spp} of SiC grating. The repeated peaks existing at integer numbers of L/λ_{spp} correspond to standing waves of the graphene SPPs, which can be indicated by the z-component of the electric field for each peak. The electric field is normalised to the incident field magnitude and goes to zero at the edges of the cavity demonstrating the antisymmetry of the plasmonic modes.

is compensated from the scattering from the edges of the cavity, not from the gating periodicity. There are two pieces of evidence to prove this: First, the plasmonic modes we explore here are not reproduced by the grating equation $k_{spp} = N\frac{2\pi}{\Lambda}$ where N is the diffraction order and Λ is the grating period. Second, the peak position stays the same for different perodicities Λ when the cavity length is fixed. Therefore, these modes are localised cavity modes and not modes that are excited by diffraction effects of the grating [130]. There are two main reasons that we consider a grating here: First, it simplifies the numerical calculations, because the reflection and the absorption can be easily defined. Second, the grating would be convenient for the fabrication and experiments. We can obtain similar results, when a single cavity is employed. It is worth noted that the field enhancement in the simulations is rather modest, which is far below the maximum reported values. This is because we only focus on the physics behind the excitation of the standing wave modes. In the next chapter, we will reveal how to obtain an extremely high field enhancement using a similar system.

As mentioned, we attribute the existence of this repeated absorption feature in Figure 3.2 to the excitation of plasmon standing waves on the graphene layer in the cavity. In this section, we confirm our intuition about these modes using a simple Fabry-Pérot model along with the graphene dispersion in Equation (3.1). The Fabry-Pérot model reads

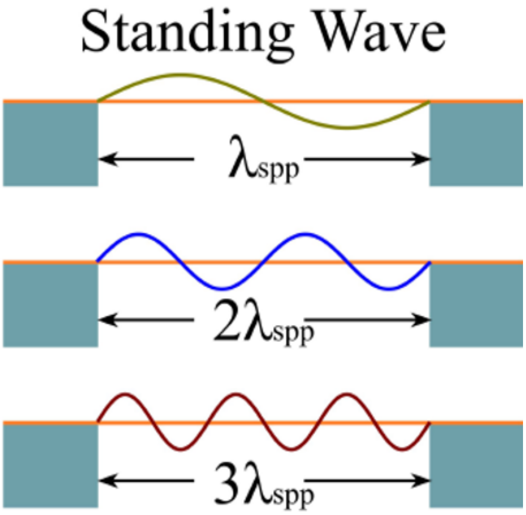

Figure 3.4: Sketch of the standing plasmonic waves of graphene SPP resonance. It should be noticed here that the cavity is assumed to be sufficiently deep ($h > 0.5\mu m$).

$$\delta\phi + \Re\{k_{spp}(\lambda)\}L = m\pi, m = 0, 1, 2, 3..., \tag{3.2}$$

where $\delta\phi$ is the phase shift introduced due to the contact between the graphene layer and SiC around the edges of the cavity, and m is a natural number denoting the resonance mode order. The phase shift here is a measure of the depth of plasmonic waves penetrating into the material of the grating. Of course, the phase shift can also be explained as the extra effective length of the Fabry-Pérot cavity that is larger than the actual cavity size. We find that when we take a phase shift of $-\pi$, the prediction from this model agrees well with the simulation results (as the blue lines indicated in Figure 3.2d) in the spectral region near the TO frequency. This is because that SiC behaves like a perfect electric conductor in this region, and thus the reflection from the walls of the cavity would be perfect. In this region, the plasmon standing waves are formed only in the cavity. However, at frequencies away from this region, the phase shift will show frequency dependence and will differ from $-\pi$. This can be understood by noted that SiC does not behave like a perfect reflector any more at these frequencies. Therefore, the electromagnetic field will be allowed to penetrate into the SiC and accumulate the extra phase shift. This interesting feature can be applied in applications where plasmonic resonators based on a graphene layer are tuned via manipulating the boundary conditions. It also should borne in mind that there will not be this feature when metals are used in the system, because metals will act as perfect conductors at mid-infrared frequencies that we consider in this thesis.

3.5 Possibility of Applications

So far, we have confirmed the excitation of plasmonic standing waves, and have provided proof for this. In the following, we will focus on the possibility of the system as a practical setup.

This system possesses several advantages over other reported systems and would be more suitable for a practical setup. For example, this system can be easily excited and provides high field enhancement, which facilitates potential applications in molecular sensing. In an experiment, the geometric parameters would not change, once the sample is fabricated. Thus, it would be more natural to explore the features of the spectra to investigate these standing wave modes for a fixed geometric parameters. Figure 3.5a shows the absorption spectra for the same geometry $L = 1.06\ \mu m$, $W = 2.0\ \mu m$ and $h = 1\ \mu m$. To demonstrate the tunability of such system, different Fermi energies are considered. It can be seen from the figure that the absorption peak exhibits blueshift with the increase of the Fermi energy and its intensity increases. This can be understood by noted that a larger Fermi energy means an increase in carrier concentration causing greater restoring force and thus a blue-shifted plasma frequency. The increase in carrier concentration also results in greater oscillation intensity and hence the growth of the absorption intensity. The tunability of the graphene is significant to this system, which boosts the practicality of the platform.

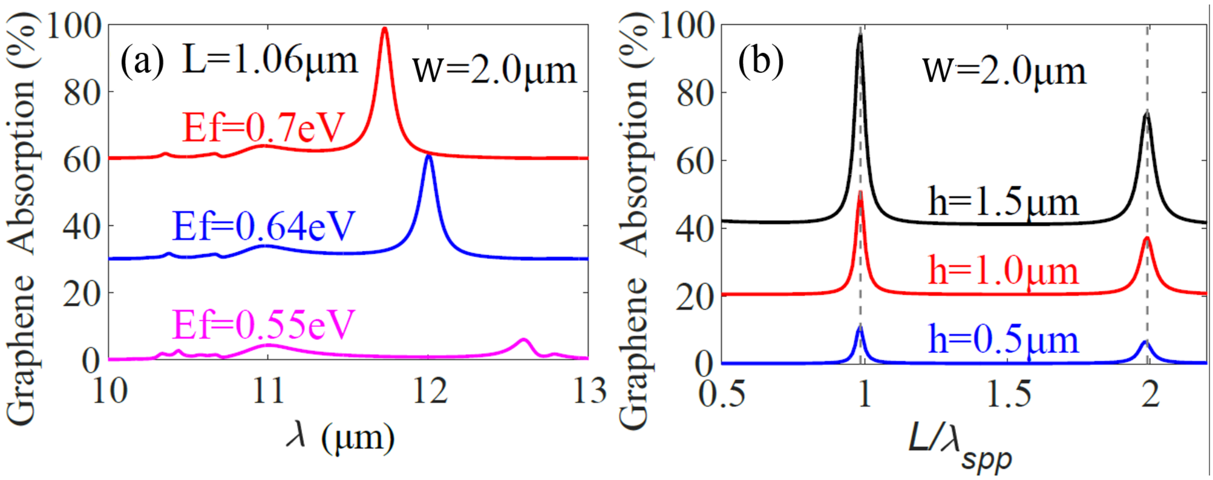

Figure 3.5: (a) The absorption in the graphene layer against the incident wavelength with fixed geometrical parameters $L = 1.06\ \mu m$, $W = 2.0\ \mu m$ and $h = 1\ \mu m$. Different Fermi energies are shown. (b) The absorption in the graphene layer against different geometric parameters L/λ_{spp} for several grating heights h with $E_F = 0.64\ eV$.

It is very interesting to study the effect of the grating height on the optical properties of the system. Figure 3.5b shows the calculated graphene absorption with varying cavity height. We observe that the resonance position is independent of the cavity height, however, the absorption intensity exhibits strong height dependence. This is because the peak positions depend only on the width of the cavity due to the Fabry-Pérot resonance, and are not perturbed by the cavity height when h is sufficiently large ($h > 500\ nm$ here) as confirmed by Equation (3.1). However, higher absorption is due to the formation of another Fabry-Pérot cavity in the vertical direction. When we increase the height, the first Fabry-Pérot resonance is approached, leading to higher absorption. This will be described in detail in the next chapter.

It is worth quantifying the applicability of the cavity as an experimental platform for strong light-matter interactions, such as for molecular detection. As mentioned, the ratio of the quality factor to the volume (Q/V) is considered as the appropriate evaluation parameter. This ratio is also know as the Purcell factor. A square cavity (with sides of length L) is considered here to calculate the volume. The width of the grating ridge is set as $1\ \mu m$, and the side length is calculated using a period of a plasmon standing wave. We take the out-of-plane decay, δ_z, of the plasmon as the dimension perpendicular to the graphene layer. This value is given by $\delta_z \sim 1/\Re[k_{spp}(\omega)]$ [131] for large field confinement $k_{spp} >> 2\pi/\lambda$. When the incident wavelength is at $12\ \mu m$, this distance is equal to $0.17\ \mu m$. The quality factor is estimated by considering $Q \approx \omega/\Delta\omega$ where we apply a Lorentzian fit to calculate the linewidth $\Delta\omega$. For $12\ \mu m$ excitation wavelength, a value of $Q/V = 8 \times 10^5/\lambda_0^3$ is found. This is comparable to the ones reported for other graphene nanoresonators [87]. However, this system has a much simpler structure and operates within a different frequency band.

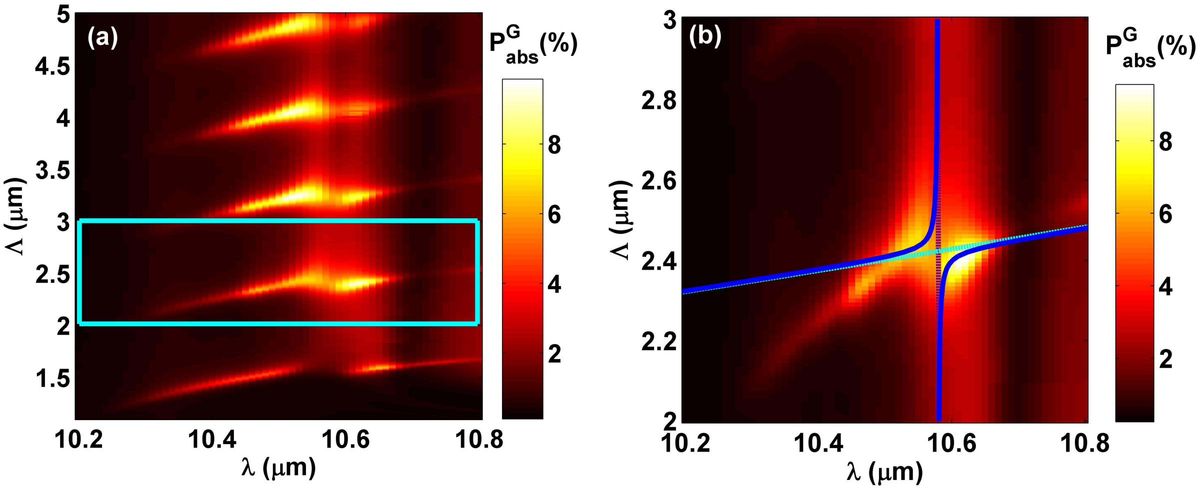

Figure 3.6: (a) Zoomed-in view of the graphene absorption (for $W = h = 1\ \mu m$) in the Figure 3.2d around the LO frequency of SiC highlighting the Rabi-splitting for different modes. (b) Zoomed-in view for $m = 3$ mode. The LSPhP wavelength and the graphene SPP dispersion are presented by the purple dashed line and the cyan dashed line, respectively. The dispersion of graphene SPP is obtained by using the Fabry-Pérot model with a phase shift of -0.35π. The resulting splitting of the hybrid mode is indicated by the blue curves.

3.6 Rabi Splitting

In this section, we will focus on another interesting feature that is revealed in Figure 3.2d and provided in more detail in a further zoomed-in view in Figure 3.6. We observe that a set of anti-crossing points exist in the absorption spectrum close to the LO phonon frequency, which demonstrates a set of GP modes and a localised SPhP mode in SiC [100] are strongly coupled. Such strong coupling can be intuitively understood by considering a classical model of two coupled harmonic oscillators [120]. As highlighted in Figures 3.6a and b, the Rabi splitting possesses a particular shape, which results from the dispersive SPP in graphene layer and the localized SPhP in SiC at a fixed wavelength of $10.6\ \mu m$. The strong coupling regime highly depends on the level of the damping of the two subsystems. Therefore, to better observe the Rabi splitting, the linewidths of GPs and the SiC cavity localized SPhPs should be small. It should be noted that GPs becomes lossy because of the phonons of the substrate [87], when the frequencies are close to the LO phonon frequency. When the loss is too large, then the anti-crossing is invisible. This is because only when the difference in the real parts of the energies (shown below) is bigger than the widths of the new modes, the actual Rabi splitting can be visible. However, when the large loss is introduced, the two energies would have larger line-widths and the double peak maxima would essentially overlap and not be visible [120]. Fortunately, in the system discussed in this chapter, GPs are excited in the graphene layer which is free-standing in the cavity and not in contact with the substrate. The loss is not too large, and thus we should neglect this effect.

To quantitatively analyse the strength of coupling, we extract a slice of the graphene absorption and apply a fit to the curve using a sum of two Lorentzian functions in Figure 3.7. We find that the peak separation in the Rabi splitting, $\hbar\omega_R$, equals to $1\ meV$. This parameter can then be employed within a coupled harmonic oscillator model to describe the anti-crossing behaviour [132]

$$E_{\pm}(\omega) = \frac{\hbar\omega_{SPP} + \hbar\omega_{SPhP}}{2} \pm \frac{1}{2}\sqrt{(\hbar\omega_R)^2 + (\hbar\omega_{SPP} - \hbar\omega_{SPhP})^2}. \tag{3.3}$$

This model has been used heavily in the field related to plasmon and phonon polaritons. In this particular case, the localized SPhP energy is fixed with a value of $0.12\ eV$ and the GP energy can be obtained as following by using Equations (3.1) and (3.2)

$$\omega_{SPP} = \sqrt{\frac{(m\pi - \delta\phi)e^2 E_F}{L\pi\hbar^2\epsilon_0(\epsilon_1 + \epsilon_2)}}. \tag{3.4}$$

In this equation, both ϵ_1 and ϵ_2 are set as 1, the phase shift is regarded as the fitting parameter and it is not expected to be $-\pi$ at these frequencies any more. In order to get a good fit for the

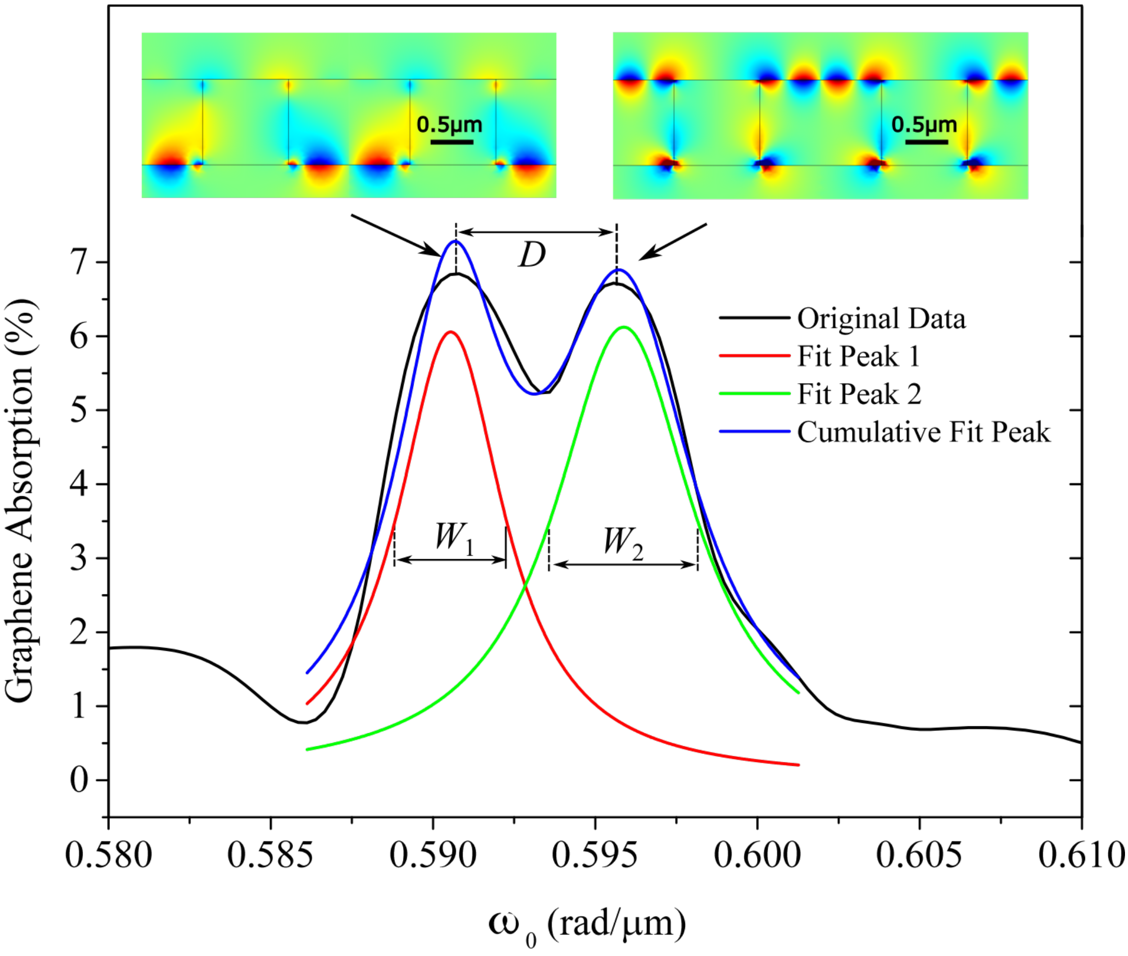

Figure 3.7: Spectra corresponding to the $L = 1.45\mu m$ (which means $\Lambda = 2.45\mu m$). These peaks are fitted by the summation of two Lorentz equations. The full widths at half maximum of these two peaks are $0.004\ rad/\mu m$ (W_1) and $0.005\ rad/\mu m$ (W_2), respectively. The distance of the splitting is $D = 0.005\ rad/\mu m$.

whole set of the GP modes shown in Figure 3.6, we obtain a phase shift of $\delta\phi = -0.35\pi$. This value clearly indicates that the SiC does not behave like a perfect reflector at these wavelengths.

We also show two near field plots corresponding to the two modes in Figure 3.7. These plots reveal the different nature of the hybrid mode, depending on the incident frequency. At lower frequencies, the field is situated at the bottom of the cavity, and introduces high absorption due to the phonons. Thus the mode is more phonon-polariton-like. At larger frequencies, the field is concentrated in the graphene layer on top (as we saw before) because of the graphene SPPs, and therefore the mode is more graphene-plasmon-like. This particular phenomenon is a consequence of strong coupling between modes, and can be used to realize spatial control of the near field distribution. This highly advantageous behaviour of the strong coupling has a high potential to be applied in phonon-polariton based switches. Of course, the cavity width and doping level can be used to achieve further manipulation of the relative contribution of each mode in the hybrid mode.

Finally, we quantify the strength of the coupling by comparing the linewidths of the constituent modes (W_1 and W_2) to the distance of the splitting (D). Considering the Rabi splitting to be experimentally observable, we conclude $D \gtrsim W$ [120]. The splitting is fitted using a sum of two Lorentz equations. The obtained values of the parameters are listed in the caption of Figure 3.7. When the largest linewidth is considered, we get $D/W = 1$ which demonstrates that the interaction of the two modes is strong coupling. It is obvious that the ratio of D/W is just on the threshold of the required value, and there are more possibilities of the definition of the strong coupling. However, this figure is expected to be improved by further optimisation of the system.

3.7 Conclusions

In this chapter, the graphene and SiC cavity system has been introduced. We have explored the coupling between the SPPs in graphene and the SPhPs in SiC, and have shown its suitability as an experimentally realisable, tunable cavity. We have demonstrated that a number of new modes (in the low absorption part of the Reststrahlen band) result from the hybridization of a graphene monolayer and a SiC grating. Such modes are antisymmetric plasmon standing waves that can be interpreted by a simple Fabry-Pérot model. The absorption peaks positions (corresponding to the Fabry-Pérot resonances) can be tuned by altering the Fermi energy of the graphene and the cavity width, which shows the tunability of this system. In the vicinity of LO frequency, we observe a hybrid mode resulting from the strong coupling between graphene SPP and local SPhP. This hybrid mode shows the characteristics of both component modes. Our results also provide the possibility for strong coupling with local trace level quantities of molecules. We find that, over a small frequency range in mid-infrared, the spatial profile of the hybrid modes can change significantly. The tunability, along with high quality factor and low modal volume, makes the system fit for cavity quantum-electrodynamics and molecular sensing.

CHAPTER 4

Cavity Height Dependence of Graphene Plasmons

In the previous chapter, we have introduced a simple system, where we can efficiently excite standing waves of graphene SPPs and have studied the coupling between the SPPs in graphene and SPhPs in SiC. A simple Fabry-Pérot model can be used to well explain the observed phenomenon. As shown in Equation (3.2), in this model the in-plane wavevector of GPs needs to be calculated, and thus we applied the most famous and most commonly used dispersion relation of SPPs in graphene (see Equation (3.1)). However, there is an assumption in this expression that will limit its scope of applications. In this chapter, we will address this issue first. In addition, we will explore the vertical properties of the SiC cavity and optimize the design to achieve total absorption and strong compression.

The content in this chapter was previously published by the author as a lead-author article in the journal titled 'Applied Materials Today', and thus, is credited to: Xiaofei Xiao, Xiaofeng Li, Joshua D Caldwell, Stefan A Maier, Vincenzo Giannini. "Theoretical analysis of graphene plasmon cavities." Applied Materials Today, 12, 283-293, 2018. Copyright Elsevier.

4.1 Overview

As we can see from Equation (3.1), the commonly used dispersion relation of a plasmonic wave in a continuous monolayer of graphene depends on the materials above and below the graphene film, as well as the properties of the graphene layer itself. For cavities such as the one shown in Figure 4.1, Equation (3.1) predicts the existence of standing waves which have been observed [33, 86, 121, 122]. One important feature of these investigated cavities, however, is that they have sufficiently deep ($> 0.5\mu m$) trenches h, so that the materials below the cavities have little impact on this relationship. Hence, Equation (3.1) provides a good approximation of the behaviour. This is not the case for a shallow cavity. Here, we explore the dependence of the dispersion relation on the height of the cavity in such systems.

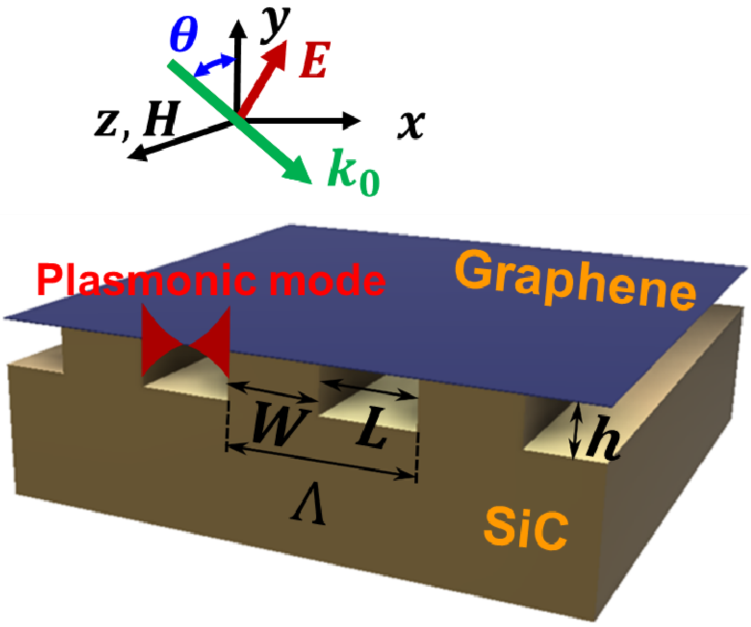

Figure 4.1: Schematic of a SiC grating-cavity-assisted GP excitation. The incident light is transverse magnetic polarized in air, where Λ, W, L, and h are the period, ridge width, trench length, and height of the grating, and θ is the incident angle. The incident light can be titled in this system, compared to the configuration shown in Figure 3.1.

In this chapter, we explore the dependence of the dispersion relation on the height of the cavity, and explore the coupling between SPhPs and GPs. We derive an analytical expression for the dispersion relation of the GP waves in a multilayer system, providing a useful tool to show the influence of the materials below the cavity on the dispersion relation. We consider a system comprising a single layer of graphene and a SiC grating with cavities (see Figure 4.1). The scattering from the sharp edges of the cavity overcomes the large mismatch between the GPs and the incident light. The absorption properties and field distributions of this system in the infrared range are investigated. The results show that the derived analytical description of the dispersion relation of the GPs can precisely predict the excitation of the cavity GP waves, while Equation (3.1) fails for systems with shallow cavities. Additionally, numerical results show total absorption can be achieved under certain parameters, which can be predicted precisely using a Fabry-Pérot model in the horizontal direction for GPs and a Fabry-Pérot model in the vertical direction for gap SPhPs. This means that the interaction of the SPPs and SPhPs can be used to tune the cavity resonances. High enhancement and extraordinary compression of GPs are realized under certain conditions. We further provide results for different doping levels and different substrates. Under normal incident excitation, only antisymmetric plasmon modes are excited because of the symmetry of the system. To excite symmetric plasmon modes, we adopt oblique incidence to break the system symmetry. Finally, a potentially simpler and more realistic configuration is outlined.

This section is structured as follows: in section 4.2, we derive the dispersion relation for the GP waves in multilayer systems. In section 4.3, we excite the standing waves using the Fabry-Pérot cavity effect in the horizontal direction, compare the predictions from the derived dispersion relation and the simulation results using FEM, and discuss the influence of the materials below the cavity on the dispersion relation. In section 4.4, we explore the cavity height-dependence of GPs, present the vertical Fabry-Pérot cavity effect, and discuss the coupling between SPhPs and SPPs in this system. In section 4.5, we further report the high enhancement and extraordinary compression of the GPs. In section 4.6, we present examples under different doping levels. In section 4.7, we demonstrate the possibility of exciting symmetric plasmon modes at oblique incidence. In section 4.8, we compare the effects of different substrates. In section 4.9, we outline the potentially simpler and more realistic configuration.

4.2 Graphene Plasmons in Multilayer Systems

We consider the most general three-layer system consisting of alternating conducting and/or dielectric films with non-source-free boundary conditions, as illustrated in Figure 4.2: Firstly, layer II, a slab of thickness t, is sandwiched between two infinitely thick claddings (layers I and III). The relative permittivities and permeabilities are ϵ_i and μ_i, respectively, where $i = 1, 2, 3$ represent materials I, II and III, respectively, and μ_i is equal to 1 for non-magnetic materials. Secondly, a complex surface conductivity σ_g is used to describe the property of the interface between media I and II. Hence, one can identify it as a I-G-II-III system, where I, II and III represent metal or dielectric materials, and G represents a 2D material (graphene in this example). In such a system, each single interface may sustain bound SPPs or SPhPs depending on the configuration. It is worth noting that previously studied metal-insulator-metal structures, insulator-metal-insulator structures, insulator-excitonic material-insulator structures, and insulator-insulator-insulator structures including 2D materials can be regarded as special cases of this system [1, 133, 134].

Since we are only interested in the lowest-order GP modes here, we begin by looking for the general TM solution. Using the coordinate system of Figure 4.2, we write the wavenumber of GPs as β, which corresponds to the component of the wavevector in the direction of propagation (x-direction). In source-free regions of space, the GP magnetic fields and electric fields can be expressed by the following sets of equations: In the upper space ($z > t/2$),

$$E_x = iA\frac{1}{\omega\epsilon_0\epsilon_1}k_{z1}e^{i\beta x}e^{-k_{z1}z}, \tag{4.1}$$

$$H_y = Ae^{i\beta x}e^{-k_{z1}z}, \tag{4.2}$$

$$E_z = -A\frac{\beta}{\omega\epsilon_0\epsilon_1}e^{i\beta x}e^{-k_{z1}z}, \tag{4.3}$$

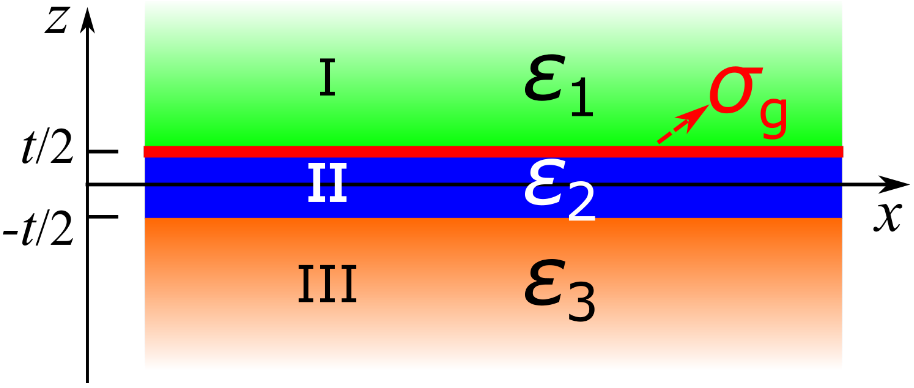

Figure 4.2: Geometry of a three-layer system consisting of a thin layer II (the middle space) sandwiched between two infinite half spaces I (the upper space) and III (the lower space) with an interface between media I and II characterized by a complex surface conductivity σ_g (representing graphene or, more generally, any conducting 2D material).

and in the middle space ($-t/2 < z < t/2$, the)

$$E_x = -iC\frac{1}{\omega\epsilon_0\epsilon_2}k_{z2}e^{i\beta x}e^{k_{z2}z} + iD\frac{1}{\omega\epsilon_0\epsilon_2}k_{z2}e^{i\beta x}e^{-k_{z2}z}, \tag{4.4}$$

$$H_y = Ce^{i\beta x}e^{k_{z2}z} + De^{i\beta x}e^{-k_{z2}z}, \tag{4.5}$$

$$E_z = C\frac{\beta}{\omega\epsilon_0\epsilon_2}e^{i\beta x}e^{k_{z2}z} + D\frac{\beta}{\omega\epsilon_0\epsilon_2}e^{i\beta x}e^{-k_{z2}z}, \tag{4.6}$$

and in the lower space ($z < -t/2$)

$$E_x = -iB\frac{1}{\omega\epsilon_0\epsilon_3}k_{z3}e^{i\beta x}e^{k_{z3}z}, \tag{4.7}$$

$$H_y = Be^{i\beta x}e^{k_{z3}z}, \tag{4.8}$$

$$E_z = -B\frac{\beta}{\omega\epsilon_0\epsilon_3}e^{i\beta x}e^{k_{z3}z}, \tag{4.9}$$

where k_0 is the wavenumber in free space as usual, A, B, C and D are the field amplitudes satisfying the boundary conditions, $k_{zi} \equiv k_{i,z}$, denotes the z-components of the wavevectors in the three materials, which reads $k_{zi}^2 = \beta^2 - k_0^2\epsilon_i$ for $i = 1, 2, 3$.

By applying the boundary conditions, the following requirements should be satisfied at the interfaces between non-magnetic materials: at the upper interface at $z = t/2$

$$E_x^1 = E_x^2, \tag{4.10}$$

$$H_y^1 - H_y^2 = -\sigma_g E_x^2, \tag{4.11}$$

and in the lower interface at $z = -t/2$

$$E_x^2 = E_x^3, \tag{4.12}$$

$$H_y^2 = H_y^3. \tag{4.13}$$

Solving this system of linear equations results in an implicit expression for the dispersion relation linking β, t, and ω via

$$e^{-2k_{z2}t} = \frac{k_{z2}/\epsilon_2\delta + k_{z1}/\epsilon_1}{k_{z2}/\epsilon_2\delta - k_{z1}/\epsilon_1}\frac{k_{z2}/\epsilon_2 + k_{z3}/\epsilon_3}{k_{z2}/\epsilon_2 - k_{z3}/\epsilon_3}, \tag{4.14}$$

where

$$\delta = 1 + \frac{i\sigma_g}{\omega\epsilon_0\epsilon_1}k_{z1}. \tag{4.15}$$

The impact of the material not in contact with the graphene layer is fully considered in the derived dispersion relation, which will show a significant distinction for shallow cavity assisted structures. It should be noted that Equation (4.14) is valid for both real and complex ϵ_i. The considered system represents a variety of configurations under some assumptions, such as $\sigma_g = 0$. Additionally, this expression implies that β cannot be written in an explicit form. We note that when t is sufficiently large, Equation (3.1) is a good approximation of Equation (4.14). Finally, the GP magnetic and electric fields are obtained from Equation (4.1)-Equation (4.9)

$$A = D\frac{2k_{z1}/\epsilon_1\delta}{k_{z1}/\epsilon_1\delta + k_{z3}/\epsilon_3}e^{(k_{z3}-k_{z1})t/2}, \tag{4.16}$$

$$B = D\left[\frac{k_{z1}/\epsilon_1\delta - k_{z3}/\epsilon_3}{k_{z1}/\epsilon_1\delta + k_{z3}/\epsilon_3}e^{(k_{z2}-3k_{z1})t/2} + e^{(k_{z1}+k_{z2})t/2}\right], \tag{4.17}$$

$$C = D\frac{k_{z1}/\epsilon_1\delta - k_{z3}/\epsilon_3}{k_{z1}/\epsilon_1\delta + k_{z3}/\epsilon_3}e^{-k_{z1}t}. \tag{4.18}$$

The in-plane wavevector of the GP, β, is a complex number with the real and imaginary parts determining the GP wavelength and the propagation length. To investigate the properties of GPs, the ERI of the GP defined will be used. In the following, β will be written as k_{spp}^h (where $k_{spp}^h = N_{\text{eff}}k_0$) to explicitly show the height dependence of the wavevector of the GPs. We should borne in mind that in most cases, we expect strong field confinement and long propagation length. It is worth noted that the superscript in k_{spp}^h denotes the height dependence, which is different from the k_{spp} mentioned in Chapter 3.

4.3 Plasmonic Standing Waves in Shallow Cavities

As we mentioned, the plasmonic waves in graphene have extremely high field confinement, which enable us to build devices with dimensions well beyond the diffraction limit. However, to excite the GPs with a free-space optical wave is still very challenging due to the large differences in wavevector. Here we still use one of the most widely used schemes – scattering from the sharp edges of cavities, as shown in Figure 4.1, to provide the necessary additional momentum and efficiently facilitate the excitation, whilst we still consider the cavity as part of a periodic structure. As we confirmed in Chapter 3, it is the scattering by defects (sharp ridges, in our case) that generates a broad spectrum of wavevectors, in which a solution to the following coupling condition can be easily found

$$k_{spp}^{h}(\lambda_0) = \frac{2\pi}{\lambda_0} sin(\theta) + K. \tag{4.19}$$

Here θ is the incident angle, and K is the compensated wavevector generated from the scattering process. The superscript h is explicitly used to stress the dependence of the dispersion relation on the height of the cavity in Figure 4.1. For a normal incident wave ($\theta = 0°$), we easily obtain a simplified formula $k_{spp}^{h}(\lambda_0) = K$.

Although the wavevector mismatch is overcome by scattering, the condition for establishing standing waves in the cavity needs to be satisfied, because GPs are excited from both edges and the forward and backward launched waves must constructively interfere. This is still true in this chapter. Thus, the cavity length L needed for free-space wavelength λ_0 is still determined by a Fabry-Pérot equation

$$\delta\phi + \Re\{k_{spp}^{h}(\lambda_0)\}L = m\pi, m = 0, 1, 2, 3..., \tag{4.20}$$

where $\delta\phi$ and m have their usual meanings. However, it should be noted that the k_{spp}^{h} has the height dependence now, compared to k_{spp} in Equation (3.2). In this chapter, the cavity height does not change the boundary conditions. Thus, the tangential component of the electric field at the edges still needs to vanish as a consequence of the electric field boundary conditions, resulting in a phase shift of $-\pi$ for the plasmon waves. Figure 4.3 shows the height-dependent standing waves of the GPs supported on the cavity.

For a TM wave, the plasmonic waves in graphene are excited when the cavity length L matches Equation (4.20) and the optical energy is dissipated due to the Ohmic loss while the plasmonic wave propagates in the graphene monolayer. At normal incidence, the GP waves originated from the two edges of the cavity are out-of-phase, and thus, antisymmetric plasmon modes associated with odd-mode order in Equation (4.20) can occur. At oblique incidence, the odd

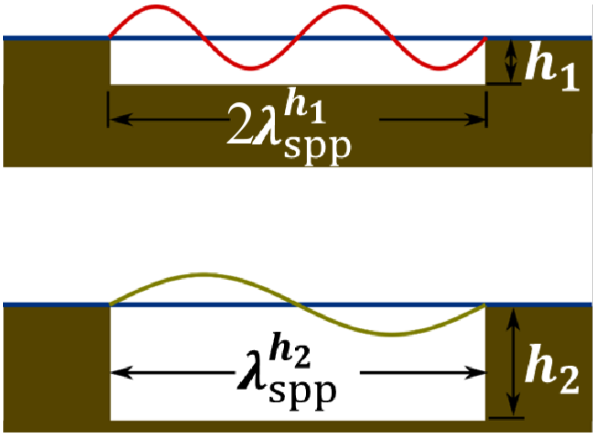

Figure 4.3: Sketch of the standing waves of GP resonances with height dependence.

modes can be excited from two edges, and thus, the plasmons with even-mode order can be excited. Here we simulate the optical response of the structure shown in Figure 4.1 using FEM. Unless specified, the incident light is TM polarized and incident from the air side, normal to the surface. Our study [121] shows that the ridge width does not change the essence of the proposed theory used to precisely predict the excitation of cavity GP waves, and that the ridge width does have influence on the excitation efficiency of the graphene absorption. To obtain a high efficiency for this work, we have fixed the ridge width at $2\mu m$.

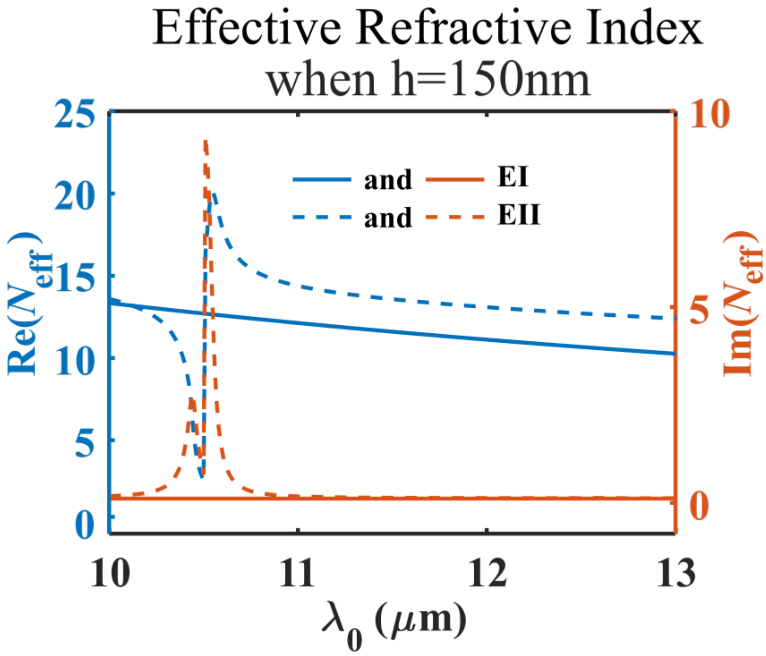

Figure 4.4: Real and imaginary parts of the ERI for different values of the incident wavelength λ_0 obtained from both Equation (4.14) (marked as EII) and Equation (3.1) (marked as EI), where media I and II are air, medium III is SiC, $E_F = 0.64eV$, and $h = 0.15\mu m$.

To validate our model we begin by considering the short grating height case. In the simulation, incident wavelengths and cavity lengths are in the range $10\mu m \rightarrow 13\mu m$ and $0.1\mu m \rightarrow 2.5\mu m$, respectively, with a grating height fixed at $0.15\mu m$. The SiC substrate is infinitely thick below the grating to switch off the transmission channel and simplify the analysis. Figure 4.4 shows the ERI for different values of the incident wavelength λ_0 obtained from Equation (4.14), where media I and II are air, and medium III is SiC (in Figure 4.2a). One striking feature is the abrupt change of the ERI with incident wavelength around $10.5\mu m$. This can be understood by noting the change of the refractive index of SiC. It can be seen that real and imaginary parts of ERI decrease dramatically at first and then slowly with increasing incident wavelength, when $\lambda_0 > 10.5\mu m$. The ERI obtained from Equation (3.1) is also shown in Figure 4.4 (solid lines). The difference between these two results shows the essential distinction between the calculations with and without considering the influence of the material below the cavity.

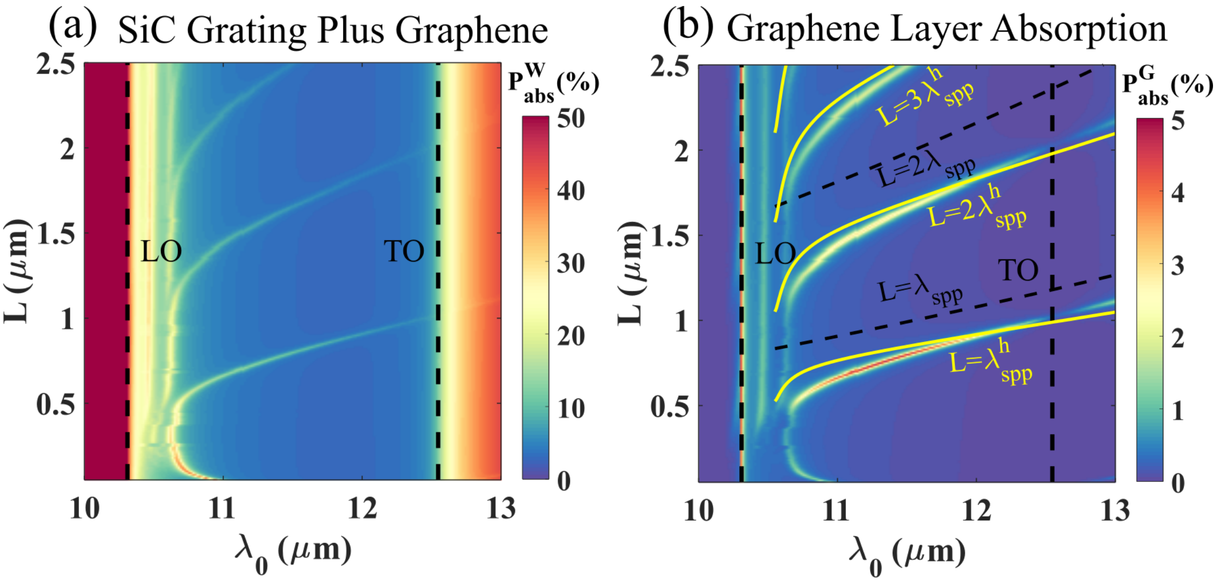

Figure 4.5: (a) Under TM polarized normal incident light, whole absorption (P^W_{abs}) for the SiC grating plus graphene structure versus the trench length (L) and the incident wavelength (λ_0), when $W = 2\mu m$, and $h = 0.15\mu m$. (b) Graphene layer absorption (P^G_{abs}) for the same structure used in (b). The yellow and black curves indicate a fit to a Fabry-Pérot model for a phase shift of $-\pi$ (see Equation (4.20)) using Equation (4.14) and Equation (3.1), respectively.

We calculate the whole absorption (P^W_{abs}, representing the sum of the absorption of the SiC grating and the graphene layer) of a SiC grating with graphene sheet present versus the trench length (L) and the incident wavelength (λ_0) shown in Figure 4.5a, when $W = 2\mu m, h = 0.15\mu m$. The strong absorption peaks around the SiC LO frequency are mainly due to the excitation of SPhPs in the SiC grating [121]. Graphene layer absorption (P^G_{abs}) in the SiC grating plus graphene structure is also shown in Figure 4.5b. The appearance of the absorption peaks in the low absorption region of the Reststrahlen band for certain cavity lengths, shown in Figure

4.5a and b, is evidence of the excitation of the GP. The electromagnetic field is concentrated on the graphene layer and the plasmon modes are antisymmetric plasmon standing waves at normal incidence. These findings have similarities with published work on the excitation of GP modes using a grating or cavity [121, 124]. However, because the cavities used in those works are very deep, Equation (3.1) is sufficient to predict the peak positions for these systems. To show how Equation (4.14) and Equation (3.1) contrast, both equations are used to theoretically predict the absorption peak positions in our system, as shown in Figure 4.5b. The remarkable agreement between the results from Equation (4.14) (compared with the ones from Equation (3.1), indicated by the black dashed curves) and the ones from the numerical simulation indicates that: (i) the material below the cavity has a distinct influence on the dispersion relation of the plasmonic wave on the graphene layer when the cavity is shallow, and (ii) the localized cavity modes are excited by the scattering from the cavity edge rather than by diffraction effects owing to the grating periodicity [121, 130], since the peak position does not change with varying Λ (for a fixed cavity length, see reference [121] for more details).

To reveal the mechanism of the cavity height dependence of the dispersion relation in our system, we investigate the system by varying the cavity height for a fixed wavelength $\lambda_0 = 12\mu m$, as shown in Figure 4.6. The ERI against the grating height is calculated using Equation (4.14) shown in Figure 4.6a. We find that the real and imaginary parts of the ERI begin to drop drastically until the height reaches $0.3\mu m$. After h exceeds sizes larger than $0.5\mu m$, the difference between the ERIs calculated from different equations is negligible. This is because when h is large ($h > 0.5\mu m$ here), Equation (3.1) is a good approximation of Equation (4.14), which means now k_{spp}^{h} depends only on the material directly above and below the suspended graphene (in this case, air). These findings are demonstrated more clearly by the good agreement between the analytical results from Equation (4.14) and those from the FEM simulations for the SiC grating plus graphene structure as shown in Figure 4.6b. The field distribution for different peaks shows that antisymmetric modes are excited. We emphasize again the dependence of λ_{spp}^{h} on the cavity height, in contrast to previous works. In Figure 4.6c and Figure 4.6d, we plot the near-fields for two systems with the same geometry, with the only exception being the different cavity heights ($h = 0.032\mu m$ and $h = 0.284\mu m$), showing that we are able to excite two different modes by only varying the cavity height. This is pictorially shown in Figure 4.3. We also show the near-field distribution for another pair of systems with the same geometry, except for differences in the trench length ($L = 1.03\mu m$ and $L = 2.07\mu m$) in Figure 4.6d and Figure 4.6e. These findings enable us to tune the cavity resonances by varying the geometric parameters. Specifically, the cavity height can be used to tune the wavelength of the plasmonic waves on the graphene. The tunability of these geometric parameters make this system very versatile.

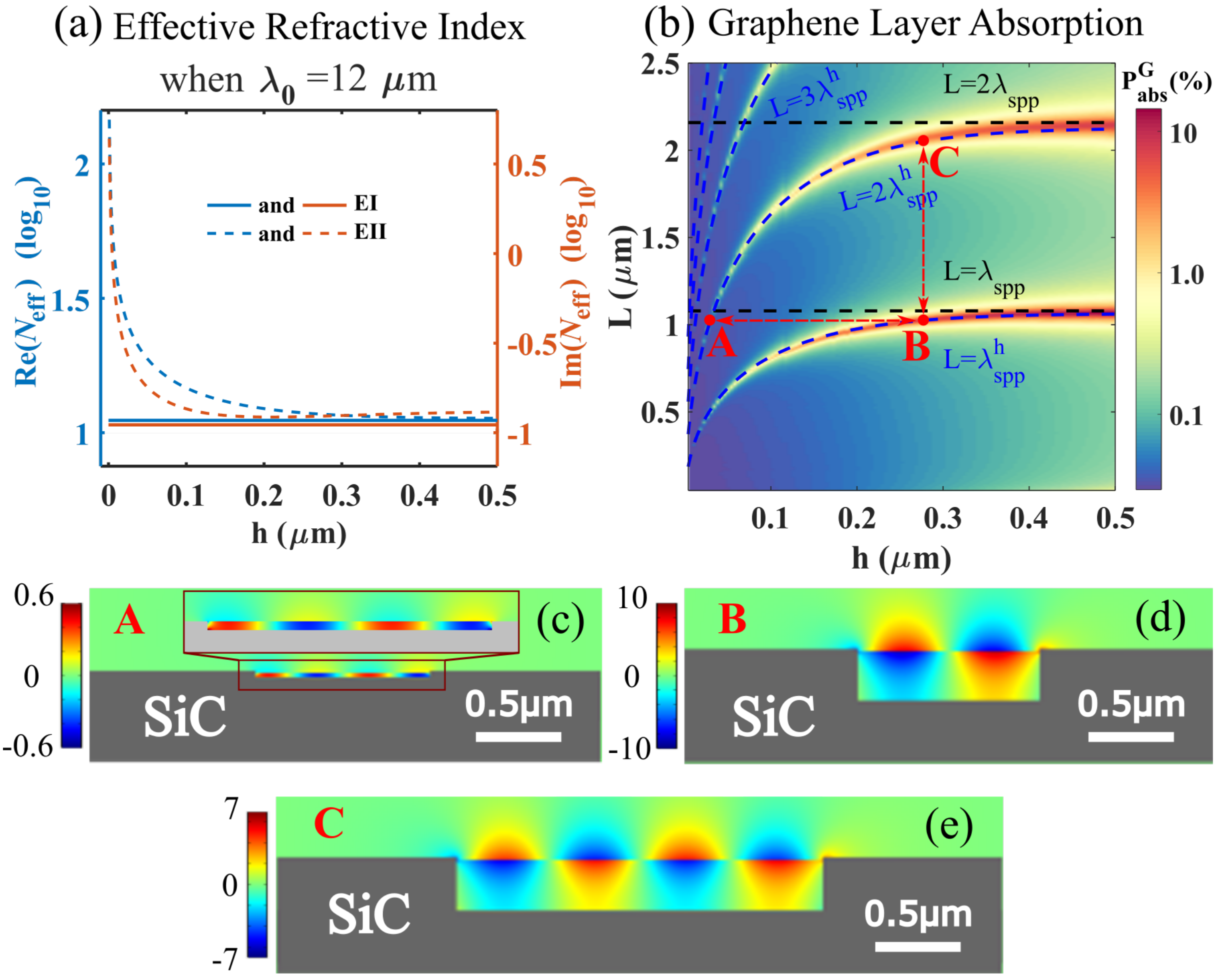

Figure 4.6: (a) Real and imaginary parts of the ERI from Equation (4.14) (marked as EII) and Equation (3.1) (marked as EI) against the grating height (h) for a TM polarized, normal incidence at a fixed wavelength $\lambda_0 = 12\mu m$, where media I and II are air, medium III is SiC, and $E_F = 0.64eV$. (b) Graphene layer absorption (P^G_{abs}) for the SiC grating plus graphene structure versus the trench length (L) and the grating height (h). The blue and black curves indicate a fit to a Fabry-Pérot model for a phase shift of $-\pi$ (see Equation (4.20)) when using Equation (4.14) and Equation (3.1), respectively. (c-e) Near-field distribution of E_z for three cases marked as points A, B, and C in (b). (c) A second-order mode with $h = 0.032\mu m$ and $L = 1.03\mu m$. The zoomed-in view is given as well. (d) A first-order mode with $h = 0.284\mu m$ and $L = 1.03\mu m$. (e) A second-order mode with $h = 0.284\mu m$ and $L = 2.07\mu m$. The electric field distribution verifies the height dependence of the standing waves supported on the cavity. The electric field is normalised to the incident field magnitude. Different colorbars are used.

To further confirm these findings, Figure 4.7a shows the graphene absorption varying with cavity length (for a fixed wavelength $\lambda_0 = 12\mu m$). The peaks at integer multiples of L/λ^h_{spp} correspond to the standing waves of the GPs as indicated by the near-field distribution plots in Figure 4.7b-e. The peak position does not change for different values of the grating period because of the independence of the excitation of the localized cavity modes on the grating effect. Comparison of the predictions from Equation (4.14) and Equation (3.1) demonstrates that the former provides more accurate results.

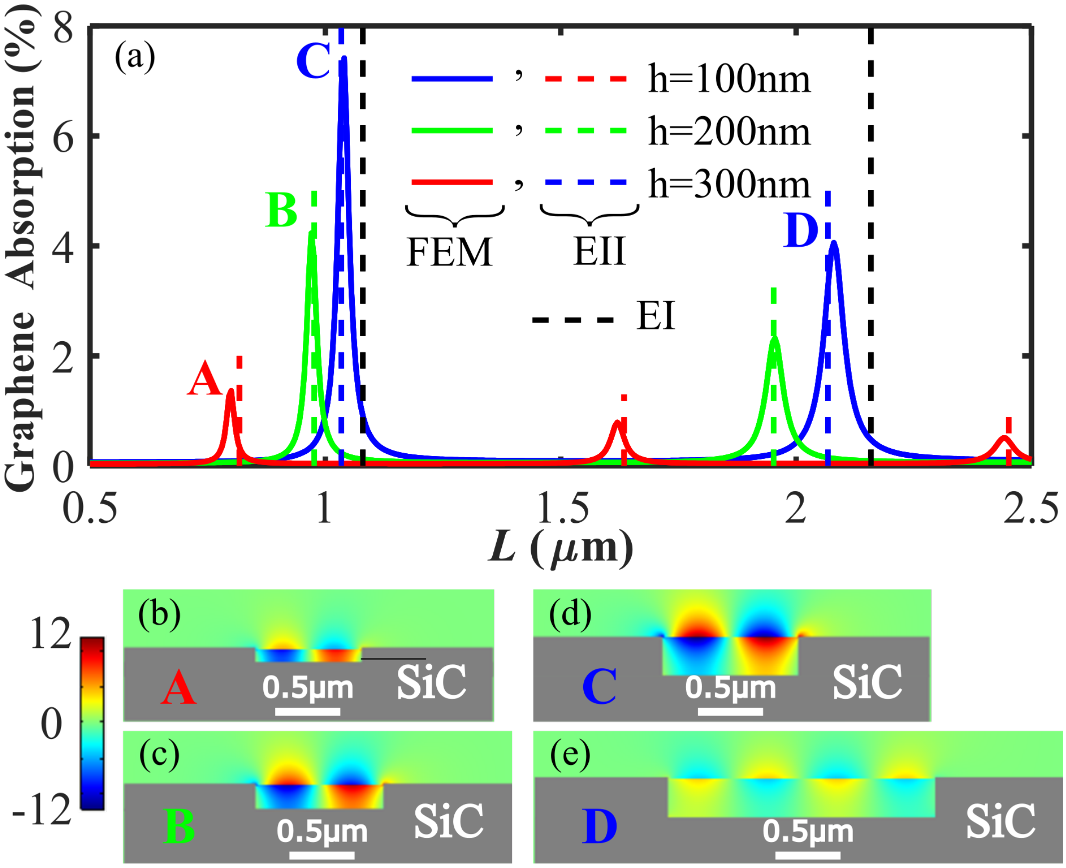

Figure 4.7: (a) Graphene absorption for different geometric parameters (h and L) of the SiC grating. Predictions of peak positions obtained from Equation (4.14) (marked as EII) are indicated by the vertical, colorized, dashed lines. Predictions from Equation (3.1) (marked as EI) are also given. (b-e) The peaks correspond to standing waves of the GPs as indicated by the near-field plots of E_z for peaks A ($h = 0.1\mu m$ and $L = 0.8\mu m$), B ($h = 0.2\mu m$ and $L = 0.97\mu m$), C ($h = 0.3\mu m$ and $L = 1.04\mu m$), and D ($h = 0.3\mu m$ and $L = 2.04\mu m$). The electric field goes to zero at the boundaries meaning the plasmon modes must be antisymmetric.

4.4 Simultaneous Excitation of Graphene Plasmon Cavity Modes and Vertical SiC Fabry-Pérot Cavity Modes

The above work derives the dispersion relation of GP waves in multilayer systems, confirms the influence of the materials below the cavity on the dispersion relation, and demonstrates the Fabry-Pérot cavity effect in the horizontal direction. In this part we explore the vertical property of the system. In Figure 4.6b, it is worth noting that the absorption is weak ($< 15\%$) when the cavity is very shallow, although becomes stronger as the cavity height h increases. Considering the fact that in this region of the spectrum SiC acts, to a good approximation, as a perfect electric conductor, it would seem that Fabry-Pérot resonances could be achieved in the vertical direction of the cavity for certain parameters .

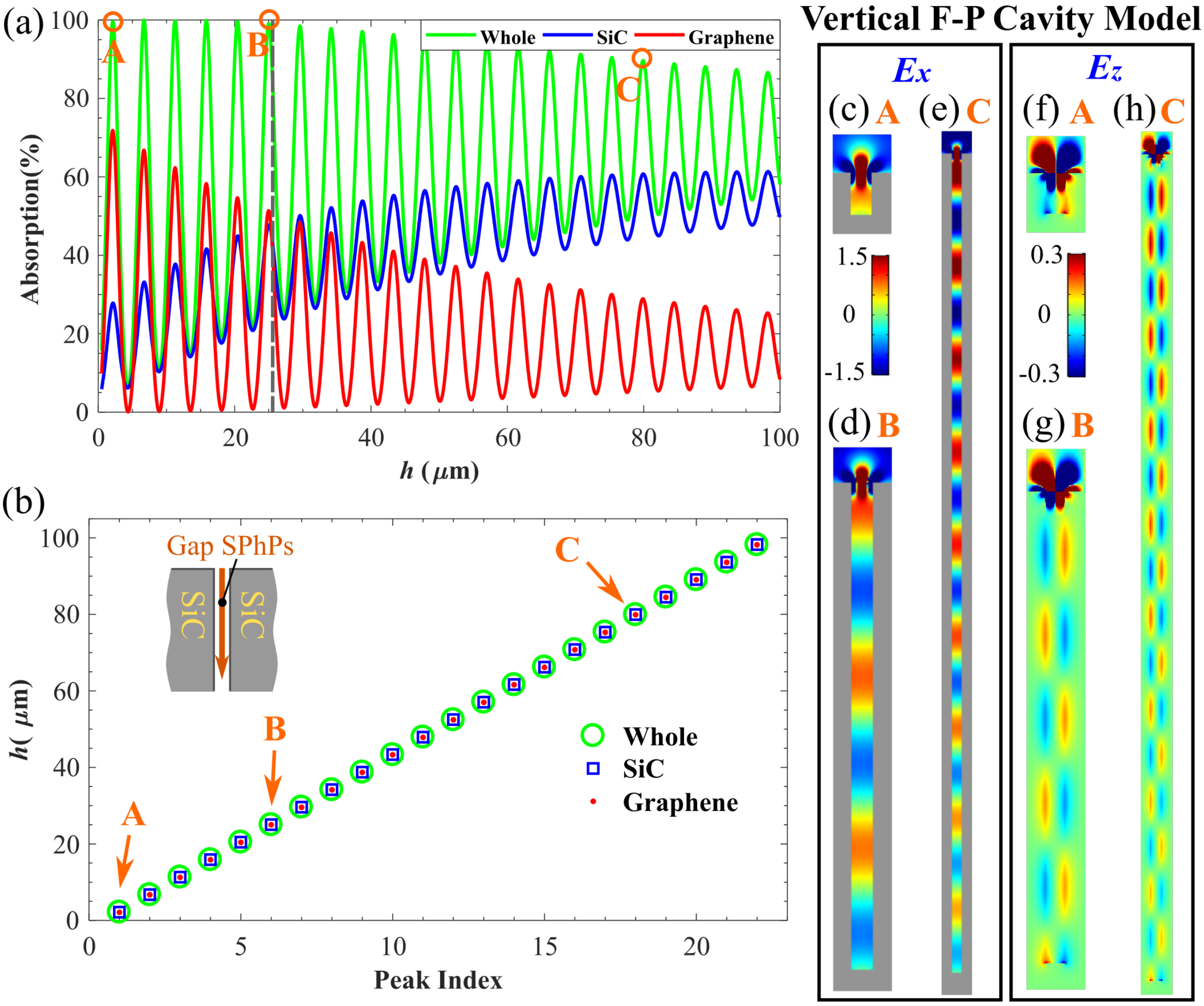

Figure 4.8: Vertical Fabry-Pérot Cavity Model. (a) Whole absorption, SiC absorption, and graphene layer absorption of the SiC grating plus graphene structure (with $W = 2\mu m$ and $L = 1.06\mu m$) as functions of the grating height at incident wavelength of $\lambda_0 = 12\mu m$. (b) Peak positions of these three types of absorptions. The peak positions for the three types of absorptions coincide. The peaks are periodically spaced as a function of the grating height. The inset shows the schematic of an air slab sandwiched between two infinite half spaces (SiC), which is a special case of the structure in Figure 4.2a. Gap SPhPs are generated in this structure. The distributions of x- and z-components of the electric field (E_x and E_z, respectively) corresponding to the points marked A, B, and C in (a) and (b) are shown for $h = 2.13\mu m$ (c and f), $h = 25\mu m$ (d and g), and $h = 79.9\mu m$ (e and h). The same colorbar is used for each component, while the scales in (e and h) are half of the ones used in (c),(d), (f), and (g). The peaks correspond to standing waves of the gap SPhPs supported in the vertical direction of the SiC cavity as indicated by the near-field plots of E_x in (c-e). The fundamental symmetric gap SPhP eigenmode propagating along the y-axis supported by the cavity is clearly seen in (c-h). The gray dashed line in (a) indicates a boundary, after which the graphene absorption is smaller than the SiC absorption.

To prove this hypothesis, in Figure 4.8a, we investigate the whole absorption of the complete system, the SiC absorption and the graphene absorption varying with the cavity height h (for a fixed wavelength $\lambda_0 = 12\mu m$ and trench length $L = 1.06\mu m$). Note that all curves in Figure 4.8a present stationary periodic oscillation behavior, which is also verified by the perfect linear relation of the peak positions shown in Figure 4.8b. The period is about $4.574\mu m$, which equals half of the effective wavelength in the cavity ($\lambda_0/\Re\{N_{\text{eff}}^{SPhP}\}/2 = 12/1.3131/2 = 4.569\mu m$. The definition of N_{eff}^{SPhP} and details of its calculation will be provided later.). This is understood by noting that there are SPhP modes excited on the cavity walls as indicated by the electromagnetic fields in Figure 4.8c-h. Similar to gap SPPs [135], for sufficiently small gap widths, the SPhPs associated with the two cavity walls interact with each other and form single gap modes, in which the fundamental symmetric eigenmode exhibits an even symmetry of the normal field component, E_x as shown in Figure 4.8c-e, and odd symmetry of the tangential electric field component, E_z as shown in Figure 4.8f-h. Similarly, these gap modes can be termed as gap SPhPs, although they are more accurately described as slot waveguide modes, having the ability to achieve strong mode confinement together with relatively low Ohmic dissipation. Similar to the wavelength and the propagation length of gap SPPs, the wavelength and the propagation length of gap SPhP are defined as $\lambda_{SPhP} = 2\pi/Re\{\beta_{SPhP}\}$ and $L_{SPhP} = 1/(2 \cdot Im\{\beta_{SPhP}\})$, respectively, where $\beta_{SPhP} = N_{\text{eff}}^{SPhP} \cdot k_0$ is the in-plane wavevector of the gap SPhP and N_{eff}^{SPhP} is the ERI of the gap SPhP. β_{SPhP} can be calculated using Equation (4.14). In our case, we assume that $\sigma_g = 0\mu S, t = 1.06\mu m$, medium I and III are SiC, and medium II is air.

The curves in Figure 4.8a divide into two parts, as shown by the grey dashed line. When the cavity height is smaller than $24.95\mu m$ (left part in Figure 4.8a), it is observed that total absorption can be achieved in the system for certain cavity heights. This indicates the critical coupling condition is satisfied [136], and a standing wave is formed. This can be understood by noted that the reflection of the front of the graphene film can be completely cancelled by the leaked wave from the cavity formed by the graphene layer and back mirror (the bottom material). Meanwhile, the graphene absorption (even 72% is achievable) dominates the whole absorption of the system. Figure 4.8c-e show clearly that the standing waves are formed in the vertical direction of the cavity. Thus, the Fabry-Pérot cavity hypothesis in the vertical direction is verified. When the cavity height is larger than $24.95\mu m$ (right part in Figure 4.8a), total absorption of the system cannot occur, and the SiC absorption becomes the main part of the whole absorption in the system. The increasing SiC absorption is mainly due to the increasing area of the SiC walls in the cavity. Because of the increase of the SiC absorption, the intensity of the reflected waves from the bottom decreases, and thus reduces the excitation efficiency of the plasmonic modes on the graphene. Meanwhile, the reflection of the front of the graphene layer cannot be completely cancelled, and consequently total absorption cannot be achieved. All three absorptions approach constant values (the constant values of the total system absorption, the SiC absorption and the graphene absorption are about 70%, 55% and 15%, respectively) when the cavity height is significantly (about five times) larger than half the characteristic propagation length of the gap SPhP ($L_{SPhP}/2 = 76.4\mu m$), because in this case most of the energy of the gap SPhPs is absorbed by the cavity walls. The proposed configuration can achieve an efficient coupling of photons to GPs and gap SPhPs, as well as provide strong coupling between GPs and gap SPhPs, for the development of future devices.

4.5 High Enhancement and Extraordinary Compression of Graphene Plasmons

In Figure 4.9, we show the intensity distributions for two special cases. This figure reveals that the most striking features are the strong intensity (the highest enhancement is ~ 4000 in Figure 4.9a) when the total absorption in the system occurs, and the extraordinary confinement (the compression factor is 375 in Figure 4.9b) of the electromagnetic field. In Figure 4.9a, the extremely high field enhancement (~ 4000) is compressed on the graphene layer providing high potential for applications in molecular sensors. This is in contrast to the grating system in the aforementioned references [121, 130] where the field enhancement is limited. Figure 4.9b shows the ability for trapping GPs in an extremely small gap. This confinement can be even stronger when using a much shallower cavity. However, the graphene absorption will get smaller with the reduction of h, when h is sufficiently small (in the case of Figure 4.8a, $h < 2.13\mu m$). Thus, we need to balance the confinement and the intensity of the field, when we try to design the system. Another interesting feature is that the intensity distribution for the total absorption case shown in Figure 4.9a is different from the one shown in Figure 4.9b. This is because the intensity has two contributions, the x- and z-components of the electric field. The x-component contribution is dominated by the vertical Fabry-Pérot effect, while the z-component contribution is dominated by the horizontal Fabry-Pérot effect. In Figure 4.9a, both contributions are strong, which can be clearly seen in Figure 4.8c and Figure 4.8f. However, in Figure 4.9b the z-component contribution dominates the intensity. Interestingly, the energy in Figure 4.9b is mainly trapped in the cavity.

4.6 Electrostatic Tuning of the Graphene Plasmons

Plasmonic modes are particularly appealing in graphene due to the ultra-broad and fast tunability of the Fermi energy via chemical doping or electrical doping. Optical gaps of up to $2eV$ (which corresponds to $E_F \sim 1eV$) can be achieved [137]. Thus, the peak positions in the absorption spectra can be tuned by electrical or chemical doping. Figure 4.10a shows graphene absorption with different Fermi energies for a normal TM incidence. Figure 4.10a shows the trench length corresponding to each peak increases with the increase of the Fermi energy. This is because the GP wavelength goes up as the Fermi energy rises. This paves the way to build cheap, reliable, ultra-fast and highly tunable optical modulators. The predictions from Equation (3.1) and

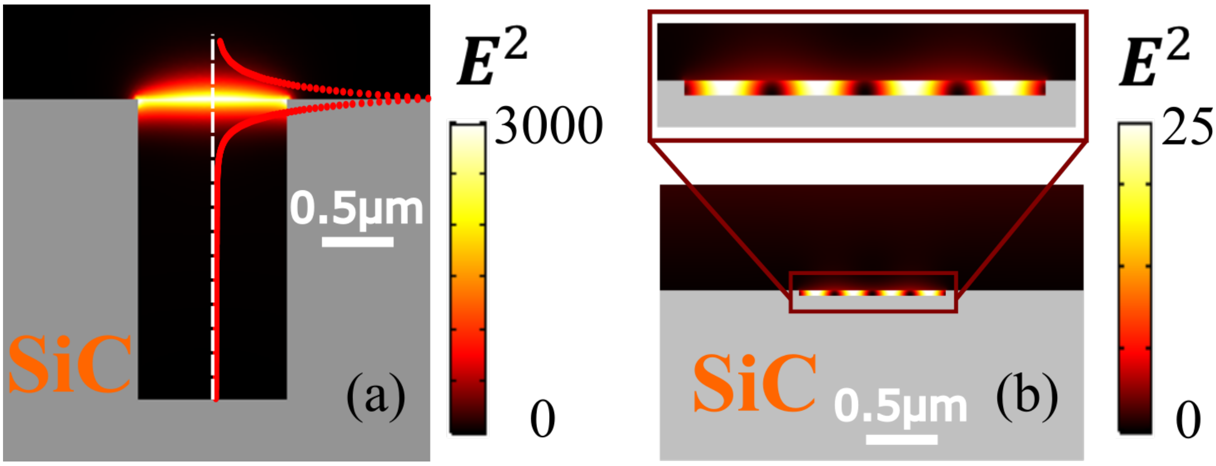

Figure 4.9: (a) High intensity (E^2) distribution for the first total absorption peak at $h = 2.13\mu m$ and $L = 1.06\mu m$ marked as point A in Figure 4.8a. Distribution of the intensity along the gray dashed line at the center of the cavtiy is given as well. The enhancement around the graphene layer in this case is about 4000. (b) Intensity (E^2) distribution of the extraordinary compressed plasmonic waves trapped in the cavity with $h = 0.032\mu m$ and $L = 1.03\mu m$ marked as point A in Figure 4.6b. The compression factor of λ_0/h in this case is 375.

the ones from Equation (4.14) indicate again that the latter equation reveals the cavity height dependence of the dispersion relation. The near-field plots of E_z for peaks marked as A-D are given in Figure 4.10b-d and Figure 4.7c.

4.7 Symmetric Plasmon Modes Excited at Oblique Incidence

The previous discussions only consider the normal TM incidence, where only antisymmetric modes are excited in the cavity. Under a TM polarized source at oblique incidence, it is expected that the incident light breaks the symmetry of the system, and consequently stimulates symmetric plasmon standing waves. In Figure 4.11, we show the properties of our system under this case for a fixed incident wavelength and fixed geometric parameters. Compared with Figure 4.7a, Figure 4.11a exhibits additional absorption peaks corresponding to the symmetric plasmonic modes, when the incidence angle is fixed at 30° with varying the trench length. The predictions from Equation (4.14) shown as black dashed lines and red dashed lines in Figure 4.11a, which agree well with the simulation results. The peaks predicted by vertical black lines correspond to antisymmetric plasmon modes confirmed by Figure 4.11c and Figure 4.11e, while the ones predicted by red lines correspond to the symmetric plasmon modes confirmed by Figure 4.11b and Figure 4.11d. It is worth noting that the GP modes of different cavities in the same grating structure are out-of-phase due to the oblique incidence, clearly indicated by the near-field of peak D for five grating periods in Figure 4.11f.

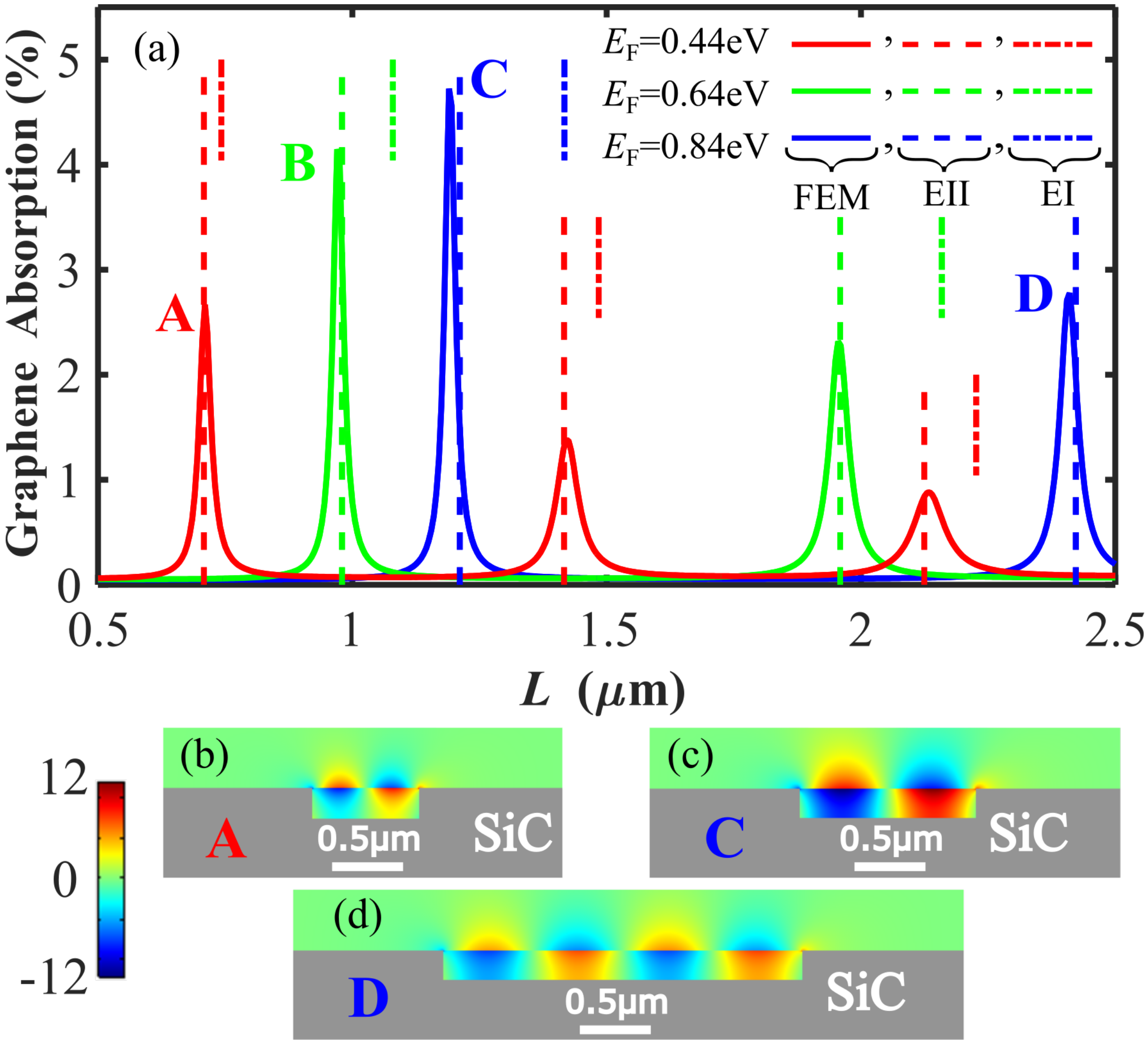

Figure 4.10: (a) Graphene layer absorption for different Fermi energies (E_F) and trench lengths (L) of the SiC grating when $h = 0.2\mu m$, $W = 2.0\mu m$, and $\lambda_0 = 12\mu m$. Predictions of peak positions from Equation (4.14) (marked as EII) are indicated by the vertical, colorized, dashed lines. Predictions from Equation (3.1) (marked as EI) are also given. (b-d) The peaks correspond to standing waves of the GPs as indicated by the near-field plots of E_z for peaks A ($E_F = 0.44eV$ and $L = 0.71\mu m$), C ($E_F = 0.84eV$ and $L = 1.19\mu m$), and D ($E_F = 0.84eV$ and $L = 2.41\mu m$). The near-field for peak B ($E_F = 0.64eV$ and $L = 0.97\mu m$) can be found in Figure 4.7c.

4.8 Comparison Between SiC and Metallic Substrates

The substrate of the configuration we considered previously is SiC, which acts, to a good approximation, as a perfect electric conductor at the frequencies of interest. However, it is expected that there is still some difference between SiC and the perfect electric conductor model.

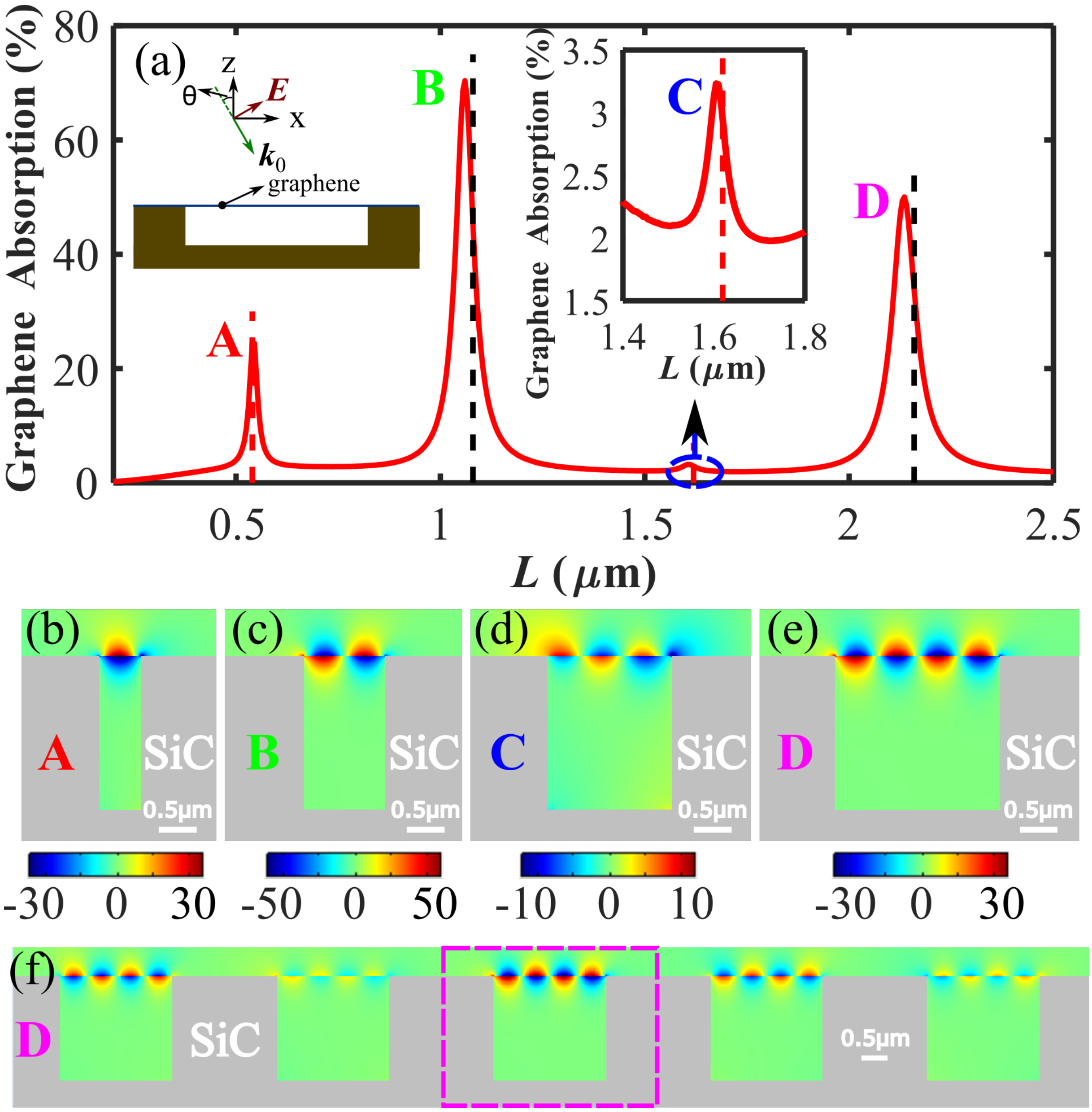

Figure 4.11: (a) Graphene layer absorption against the trench length (L) under a TM polarized oblique incidence at a incident angle of $\theta = 30°$ for fixed geometric parameters $\lambda_0 = 12\mu m$, $h = 2\mu m$, and $W = 2.0\mu m$. The insets are the schematic of a configuration with a metallic substrate and a zoomed-in plot of the third peak shown by the blue dashed line. Predictions of peak positions obtained from Equation (4.14) are indicated by the vertical dashed lines. (b-e) The peaks correspond to standing waves of the GPs as indicated by the near-field plots of E_z (here normalised to the incident field magnitude) for peaks A ($L = 0.54\mu m$), B ($L = 1.06\mu m$), C ($L = 1.61\mu m$), and D ($L = 2.135\mu m$). The peaks predicted by vertical black lines correspond to antisymmetric plasmon modes as shown in (c) and (e), while the ones predicted by red lines correspond to the symmetric plasmon modes as shown in (b) and (d). (f) Near-field plots of E_z for peak D for five grating periods. The pink dashed box showing the position of the plot in (e).

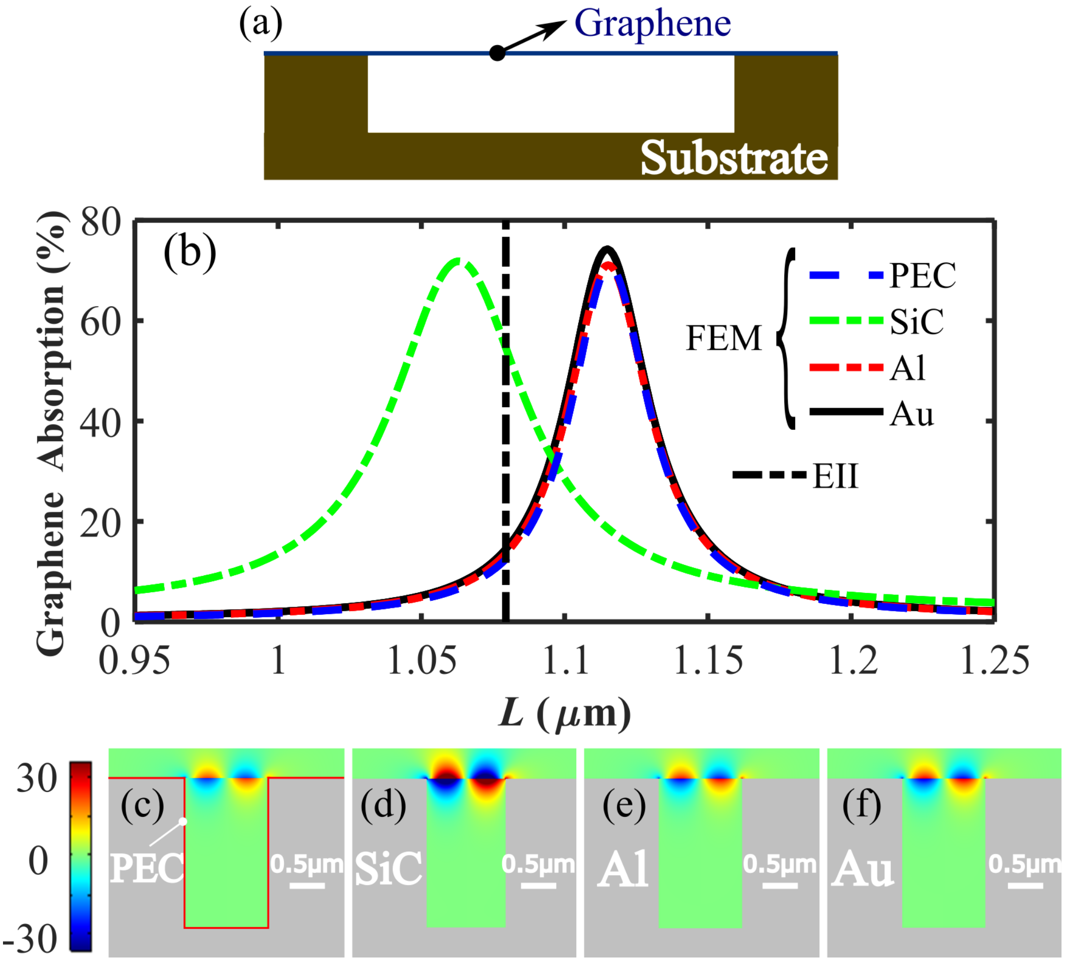

Figure 4.12: (a) Schematic of a configuration with different substrates. PEC represents perfect electric conductor. (b) Graphene layer absorption as a function of the grating trench length (L) when $h = 2.0\mu m$, $W = 2.0\mu m$, and $\lambda_0 = 12\mu m$. Predictions of peak positions obtained from Equation (4.14) (marked as EII) are indicated by the vertical black dashed lines. (c-f) The near-field plots of E_z for different substrates shown in (b). The trench length $L = 1.115\mu m$ is for (c) and (e-f), while $L = 1.063\mu m$ is for (d).

In this part, we study the effects of different substrates by changing the substruate material of the configuration shown in Figure 4.12a. In Figure 4.12b, we show the graphene absorption of the system with different substrates for fixed incident wavelength and fixed geometric parameters under the normal TM incidence. The results show that the simulations with the perfect electric conductor model and metallic materials (aluminium [138] and gold [139] here) give the qualitatively same behaviour. The behaviour is modified for the system with SiC. This can be understood by viewing the optical properties of SiC and the metallic materials. We find that metallic materials, compared with SiC, acts more like a perfect electric conductor at the frequencies of interest. It is also worth noting that the whole absorption of the system (not shown) with SiC substrate is much higher than the other three cases. One the other hand, there is a little difference between the prediction from Equation (4.14) and the peak position for perfect electric conductor model. This is because in this work we do not consider the near-field distribution around the sharp edges shown in Figure 4.12c. Figure 4.12d-f show the near-field distribution of other cases. Additionally, based on the derived equations in this study, we could predict the most appropriate range of the permittivity for the substrate that may help generate the strongest electric fields on the graphene surface.

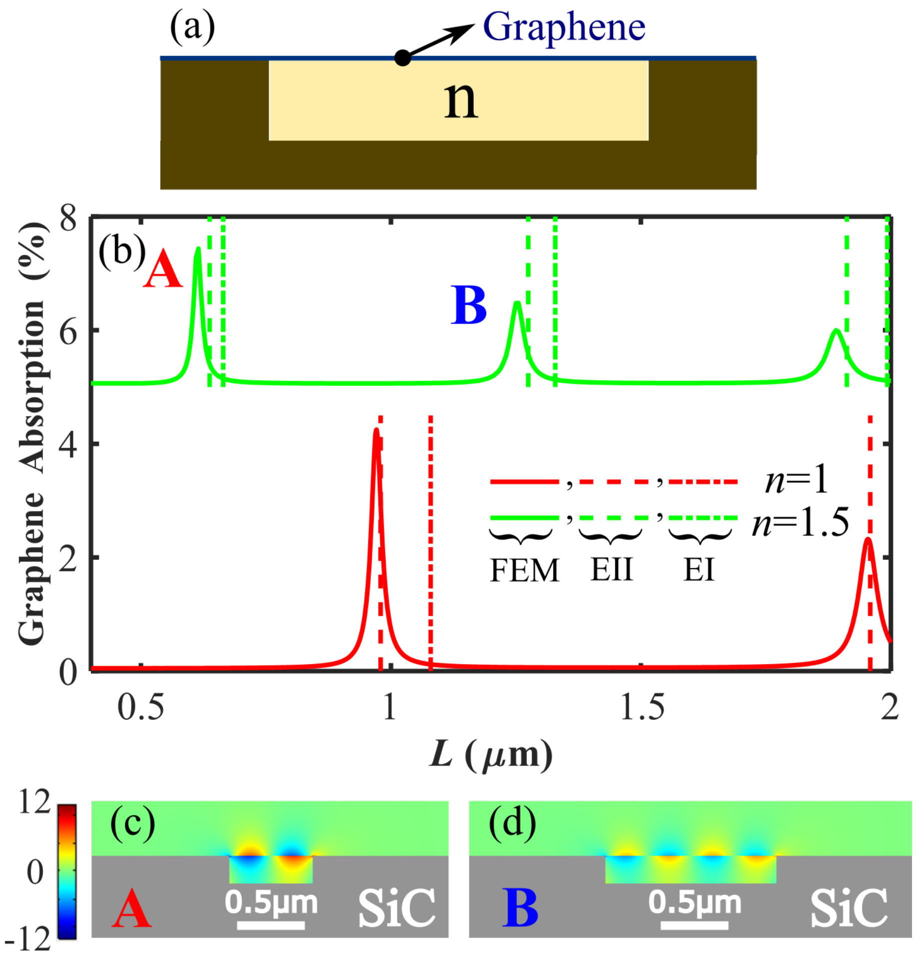

Figure 4.13: (a) Schematic of a realistic configuration with a dielectric material (n is its refractve index) filling in the cavity. (b) Graphene layer absorption as a function of the trench length (L) of the SiC grating for different values of the refractive index (n) of the cavity, when $h = 0.2\mu m$, $W = 2.0\mu m$, and $\lambda_0 = 12\mu m$. Predictions of peak positions obtained from Equation (4.14) (marked as EII) are indicated by the vertical dashed lines. Predictions from Equation (3.1) (marked as EI) are also given by the vertical dash-dot lines. The green curve has been offset. (c-d) The near-field plots of E_z for peaks A ($L = 0.612\mu m$) and B ($L = 1.252\mu m$) marked in (b).

4.9 Extension Toward Applications

In this chapter, all scenarios considered until this point are free-standing graphene layer and spaced by air cavities that served to simplify discussion and our understanding of the modes. We consider now simpler and more realistic configurations. First, we fill the cavity with a dielectric medium with the refractive index n, shown in Figure 4.13a, which can be easily achieved by deposition of oxides or an organic layer.

As an example, we analyse the modes exhibited by peak A and peak B shown in Figure 4.13b. As expected, the peak positions agree with the predictions from Equation (4.14) shown in Figure 4.13b, while the predictions obtained from Equation (3.1) are not precise. Clearly, there is a small difference between the simulated results from FEM and the predictions from Equation (4.14). This is because, although a phase shift of $-\pi$ is always used to get a fit of Fabry-Pérot model, there should be small difference between the phase shift for different configurations, which can be found by looking at the near-field around the edges. A surprising feature is that the predictions from Equation (4.14) remains very good as the number of the peaks increases, while the ones from Equation (3.1) become worse. This can be understood by noting that the additional length between peak A and peak B is one GP wavelength (as shown in Figure 4.13c and Figure 4.13d), and the difference between the simulated peak positions and their predictions from Equation (4.14) remains the same. This feature is also found in Figure 4.7 and Figure 4.10. This finding confirms the precision of Equation (4.14). In addition, by comparing the results under different n (as shown in Figure 4.13b), we find that when the refractive index of the cavity increases, the difference between the results from Equation (3.1) and Equation (4.14) reduces, and the graphene layer absorption decreases.

Apart from the refractive index of the cavity, the shape of the cavities also has an influence on the graphene surface plasmon. For example, Figure 4.14a shows a realistic configuration with rounded cavity edges with radius R and we calculate its graphene absorptions with different values of R as shown in Figure 4.14b. The resonances under rounded edges are redshifted with respect to the sharp edges case, and the shift get larger with the increase of the radius R. This is because the effective trench length increases. Also, new peaks appear due to the different reflection at the edges.

We foresee experimental demonstrations of the existence and manipulation of the cavity modes in such simple geometries. Their extraordinary confinement and strong enhancement could make the system as an ideal interface for sensing and integrated optics.

4.10 Conclusions

In this chapter, we have analysed the SPPs supported on graphene cavities made of SiC or metallic cavities. An analytical expression for the dispersion relation of GP waves in a multilayer system have been derived. This simple analytical expression is a useful tool showing the cavity height dependence of the dispersion relation of the GPs. Total absorption of the system can be achieved under certain parameters, which can be predicted precisely using two Fabry-Pérot

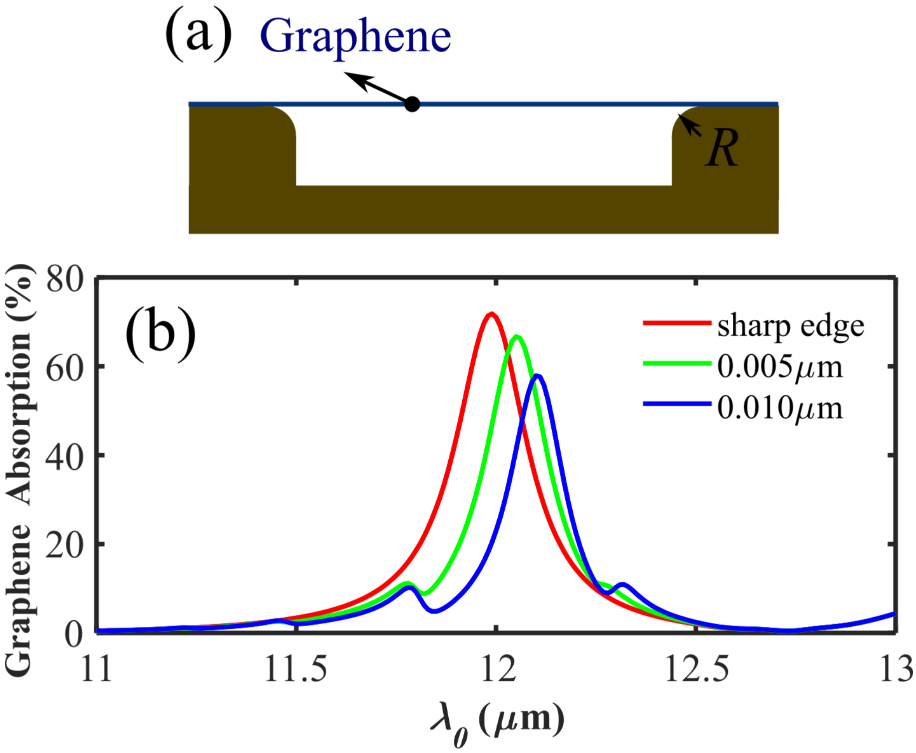

Figure 4.14: (a) Schematic of a realistic configuration with rounded cavity edges with radius R. (b) Graphene absorption for different shapes of the cavity edge, when $L = 1.06\mu m$, $h = 2.0\mu m$, and $W = 2.0\mu m$. The green and blue lines represent results with $R = 0.005\mu m$ and $R = 0.010\mu m$, respectively. The red line shows the result under the sharp edges of the cavity.

models. One Fabry-Pérot model is in the horizontal direction for GPs, while the other one is in the vertical direction for gap SPhPs. The interaction of the SPPs and SPhPs can be used in order to tune the cavity resonances. The tunability of Fermi energy and geometric parameters of the cavities, along with the substrate, make the design of this system very flexible. High enhancement and extraordinary compression of GPs have also been realized under certain conditions. Under oblique incidence, symmetric plasmon modes have been excited. Plasmon cavity modes make this an ideal system for molecular sensing and integrated optics.

CHAPTER 5

Plasmons in Suspended Graphene

In the previous chapter, we have derived an analytical expression for the dispersion relation of graphene plasmon waves in a multilayer system (see Equation (4.14)), which is a useful tool showing the cavity height dependence of the dispersion relation of the GPs. Unlike the commonly used dispersion relation (see Equation (3.1)), this new analytical expression is valid for cavities with any height, greatly expanding the scope of the dispersion relation. In this chapter, we will extend this work further to establish a model for plasmonic cavities with a suspended graphene layer upon the SiC cavity by using this new relation.

5.1 Overview

In the previous chapters, we have stated the advantages of graphene and its plasmonic waves. Due to the unique mechanical, electric, magnetic and thermal properties of graphene [140–142], graphene has received much attention by academia and industry. In particular, GPs have attracted plenty of interest for applications in optics and electronics [52, 71, 79, 121, 143, 144], especially for improving optoelectronic device performances [145, 146] and the development of wearable devices [147, 148]. Its strong confined, long-lived, easily tunable GPs make graphene a very promising 2D plasmonic material for terahertz to mid-infrared applications. [82, 149, 150]

However, theories of GPs in a suspended graphene layer are insufficient. The major reason is that the commonly used dispersion relation of GPs in a continuous graphene monolayer fails when the gap is small [151]. It is because that the expression of this commonly used dispersion relation only includes the materials above and below the graphene film, and the properties of the graphene layer itself. In Chapter 4, we have derived a much more precise relationship, and demonstrated that the GPs in a graphene plasmon cavity can be easily tuned by varying the cavity height and the material of the substrate. The height dependence of the dispersion relation paves the way for the study of GPs in a suspended graphene layer. Another challenge in the field of GPs is that, although high enhancement and extraordinary compression of GPs could be realized under certain conditions [151], it is still very challenging to achieve both simultaneously, due to the mutual limitation of the field enhancement and compression in most cases.

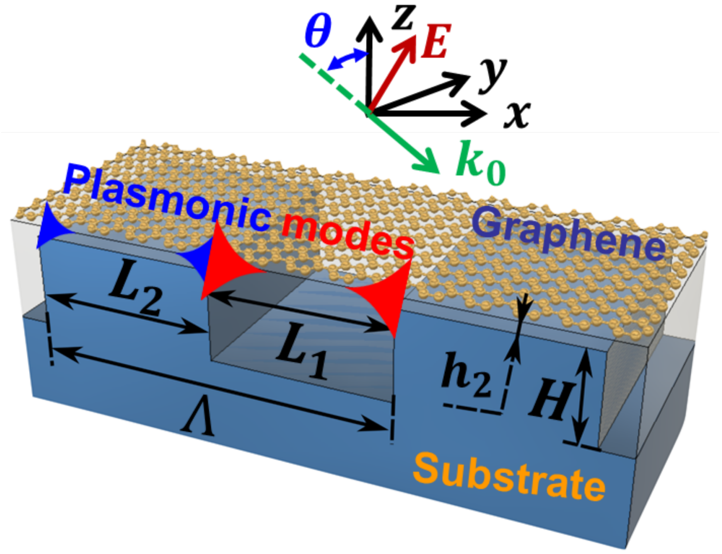

Figure 5.1: Schematic of a grating-assisted suspended graphene plasmon cavity. The incidence is TM polarized in air, where Λ, L_1, L_2, and H are the period, trench length, ridge length, height of the grating, h_2 is the gap thickness, and θ is the incident angle. Thus, we have $h_1 = h_2 + H$. The gap and the trench are filled with a dielectric medium with the refractive index n. Compared to the systems in Figure 3.1 and Figure 4.1, this system includes a gap between the graphene layer and the grating, which will introduce a huge difference.

In this chapter, we explore the optical properties of plasmons in suspended graphene such as the system shown in Figure 5.1. The investigated system consists of a continuous graphene monolayer on top of a SiC cavity with a gap space. The GPs are launched because of the scattering from the sharp edges of the cavity, which overcomes the large mismatch between the GPs and the incident light. We establish a model of the suspended graphene plasmon cavities, in which the Fabry-Pérot equation and the dispersion relation of GPs in a general multilayer system are applied. To confirm the validation of the proposed model, the graphene absorption is calculated using a numerical method. The excellent agreement between the theoretical predictions of the position of the graphene absorption peaks and the numerical results confirms the accuracy of the proposed model. Remarkably, the extremely high field enhancement and extraordinary compression of GPs occur simultaneously, thanks to the combination of a shallow cavity and a deep cavity in the same configuration. Finally, we analyse the tunability of the Fermi energy and geometric parameters of the cavities. This enables us to optimize the device to achieve potential applications by using the combination of the two cavities with different heights.

5.2 Theoretical Background

In the previous chapter, we derived a dispersion relation of GPs (see Equation (4.14)) in a general multilayer system (as shown in Figure 4.2), which will be used in this chapter to establish the model of suspended graphene plasmon cavities. To study the properties of GPs, the ERI of the GP, $N_{\text{eff}}^{h} = k_{\text{spp}}^{h}/k_0$ is introduced. Here, the superscript of N_{eff}^{h} is used to distinguish between different cavities with different heights.

The plasmonic waves in graphene have attracted numerous investigations, because of the extreme field confinement. However, efficient excitation of those plasmonic waves is still very challenging, because there is a large momentum mismatch between the incident light and GPs. In the previous two chapters, we have established a model to explain the excitation in a single graphene plasmon cavity. However, it should be borne in mind there are two different cavities in the current work, as shown in Figure 5.1: One is in the trench, and the other one is above the ridge. These cavities have different length (L_1 and L_2) and height (h_1 and h_2). In each cavity, the scattering by sharp ridges is used to generate a broad spectrum of wavevectors to compensate the momentum mismatch. The forward and backward launched plasmonic waves constructively interfere in the cavities to form standing waves. Thus, when the cavity length L_j (where $j = 1, 2$ represent the cavities in the trench and above the ridge, respectively) satisfies the Fabry-Pérot equation, the GPs could be excited. The Fabry-Pérot equation reads

$$\delta\phi_j + \Re\{k_{\text{spp}}^{h_j}(\lambda_0)\}L_j = m\pi,\ m = 0, 1, 2, 3...,\ j = 1 \text{ and } 2, \tag{5.1}$$

where $\delta\phi_j$ and m have their usual meanings. However, it should be noted that there are two cavities existing simultaneously, and hence $j = 1$ and 2. In previous chapters, we have showed that, when the substrate has metal-like behaviour and there is no gap space above the ridge, a phase shift of $-\pi$ for the plasmon waves exists in the cavity as a consequence of the electric field boundary conditions. This is still a good approximation in the case where there is a gap space. However, we will address this issue more rigorously by considering the coupling between GPs and a dipole mode. Under normal incidence, the excited plasmon modes are antisymmetric in each cavity, because of the symmetry of the system. Figure 5.2 shows a sketch of the standing waves of GP resonances supported in this system. While these waves propagate in the graphene layer, the optical energy is dissipated due to the Ohmic loss. In this chapter, we refer to this equation when we mention the Fabry-Pérot model. Different valuses of $\delta\phi_j$ will be used.

5.3 Configuration of Suspended Graphene System

To validate the established model of suspended graphene plasmon cavities, we will consider the configuration shown in Figure 5.1. The system is composed of a graphene monolayer deposited

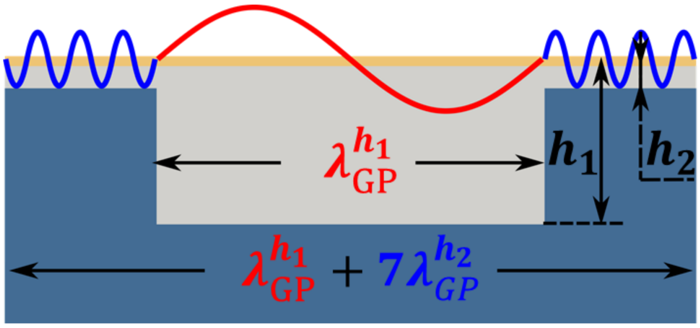

Figure 5.2: Sketch of the standing waves of GP resonances in two types of cavities in one grating period.

on a SiC grating, and we assume that there is a small gap between the two. The graphene layer is located on the x-y plane with the grating period in the x direction. The period, trench length, ridge length, and height of the grating are represented by the letters Λ, L_1, L_2, and H (see Figure 5.1). The gap thickness and the incident angle are represented by the letters h_2 and θ, respectively. The gap and the trench are filled with a dielectric medium with the refractive index n, which can be easily achieved by deposition of oxides or an organic layer. As mentioned, the graphene plasmon cavities supported by this system are two different types (see Figure 5.2). Here, we have $h_1 = h_2 + H$.

In this chapter, the incident source is TM polarized and incident from the air side, normal to the surface, and the material of substrate is SiC [96, 121, 152]. As before, the substrate is infinitely thick below the grating to switch off the transmission channel, and the material in the gap and trench is set as air (later, we will consider a more realistic configuration). The details of the properties of SiC and graphene can be found in Figure 2.8. The incident wavelength is set as $12\mu m$, since SiC acts, to a good approximation, as a perfect electric conductor at this wavelength. To obtain a high efficiency for this work, we have fixed the trench height (H) at $2\mu m$.

5.4 Varying Trench Length and Ridge Length

To investigate our system, we begin by calculating the graphene absorption varying with trench length (L_1) and ridge length (L_2) for a fixed gap thickness $h = 0.005\mu m$. The trench lengths and ridge lengths are in the range of $0.9\mu m$ to $2.6\mu m$ and $1.0\mu m$ to $2.5\mu m$. The corresponding ERIs (N_{eff}^{h}) calculated using Equation 4.14 are $56.3407 + 0.9354i$ and $11.2315 + 0.1315i$ with $h = 0.005\mu m$ and $h > 1m$, respectively, where media I and II are air, and medium III is SiC. The graphene absorption ($P_{\text{abs}}^{\text{G}}$) versus the trench length and the ridge length is shown in Figure 5.3. The strong absorption peaks exist in the low absorption region of the reststrahlen band for certain trench lengths and ridge lengths, because of the excitation of the GPs. This can be confirmed by looking at the z-component of the electric field for points labelled as A, B,C, and

D, as shown in Figure 5.4a-d. The electromagnetic field is concentrated on the graphene layer and has a fixed number of wavelengths in each cavity. The plasmonics modes are antisymmetric as a consequence of the electromagnetic field boundary conditions and the symmetry of the system. This is pictorially shown in Figure 5.2.

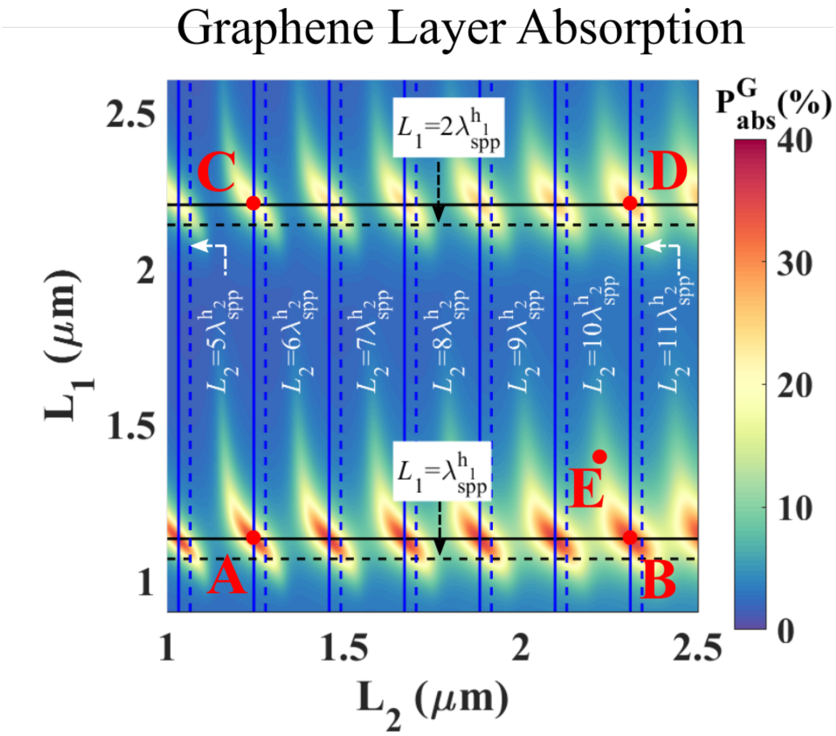

Figure 5.3: Graphene layer absorption ($P^{\mathrm{G}}_{\mathrm{abs}}$) for the SiC grating plus graphene structure versus the trench length (L_1) and the ridge length (L_2), when the gap thickness is $0.005\mu m$. The normal incidence is TM polarized at a wavelength $\lambda_0 = 12\mu m$, where media I and II are air, medium III is SiC, and $E_{\mathrm{F}} = 0.64eV$. The dashed lines indicate a fit to a Fabry-Pérot model for a phase shift of $-\pi$. The black solid lines indicate a fit to a Fabry-Pérot model for a phase shift of -1.12π, while the blue solid ones indicatie a fit to a Fabry-Pérot model for a phase shift of -0.69π.

In the earlier works, the graphene monolayer and the grating are in physical contact with one another. However, there is a gap between them in this study. This makes a striking difference, in that there exists a very strong field in the parts of the graphene which are located above the trench of the SiC grating, and consequently there is very strong absorption in these locations. In Figure 5.3, the local maximum values of the graphene absorption correspond to the excitation of both standing waves in both cavities. The predictions of those local peak positions are also given using the proposed model, as the crossing points of the black dashed lines (for the cavity in the trench) and the blue dashed lines (the cavity is above the ridge) shown in Figure 5.3. Although the reasonable agreement between the predictions and the numerical results confirms the validity of the proposed model, an apparent shift between the predictions and the real local peak positions exists. To understand this discrepancy, we did a simulation for a case without the graphene layer. Figure 5.4e shows the near field distribution for this case, where the dipole mode is excited. This always happens when the structure is much smaller than the incident wavelength. The incidence drives the positive and negative carriers to two ends of the ridge. The oscillations of those opposite carriers generate the electromagnetic field around the edges. It should be borne in mind that even if the material of the substrate is a perfect electric conductor, the dipole mode still exists. This dipole mode will couple to the graphene plasmonic modes, which could be observed clearly in the near-field plots shown in Figure 5.4a-d. As a consequence, we need to modify the Fabry-Pérot model by optimizing the phase shift $\delta\phi_j$ to be different from $-\pi$ to compensate for the difference. In the case of Figure 5.3, a phase shift of -1.12π for the plasmon waves exists for the type of cavities in the trench, while a phase shift of -0.69π for the plasmon waves exists for the other type of cavities above the ridge, as the solid lines show. However, it should be noted that the value of the phase shift $\delta\phi_j$ strongly depends on the gap thickness, the permittivities of the materials in the system, and the properties of the graphene layer. Using the modified model, we found excellent predictions as shown by the crossing points between the black solid lines (for the cavity in the trench) and the blue solid lines (the cavity is above the ridge) shown in Figure 5.3.

Due to the coupling between the GPs and the dipole mode, another interesting feature is that the strong absorption still exists, even though the conditions for establish standing waves in those two cavities are not fully satisfied individually. In addition, the shape of the strong absorption looks like a "Sigmoid function" with a rotation of 90 degrees. This is because the absorption would be still strong, as long as the boundary condition of the both cavities matches with each other, and the dipole mode would shift the absorption peak position. This was confirmed by the near-field plot (shown in Figure 5.4f) for the point marked as point E in Figure 5.3. The absorption becomes the strongest when the Fabry-Pérot resonance is satisfied in each cavities.

5.5 Gap Thickness Dependence

To show the gap thickness dependence of the dispersion relation, we investigate the system by varying the gap thickness and the ridge width as shown in Figure 5.5, Figure 5.6 and Figure 5.7. The real and imaginary parts of the ERI against the gap thickness calculated using Equation 4.14 is shown in Figure 5.5. As expected, both parts begin to drop drastically until the thickness reaches $0.3\mu m$. After the thickness exceeds sizes larger than $0.5\mu m$, both parts become constant. This is because when the thickness is larger than $0.5\mu m$, the dependence of the dispersion relation on the gap thickness and the materials of the substrate is negligible. This also could be easily verified by considering large value of the thickness of slab II in Equation 4.14. In Figure 5.6, the obtained data in simulations verify the dependence of the phase shift $\delta\phi_2$ on the gap thickness. As we can see from Figure 5.6, the phase shift follows the similar trend as

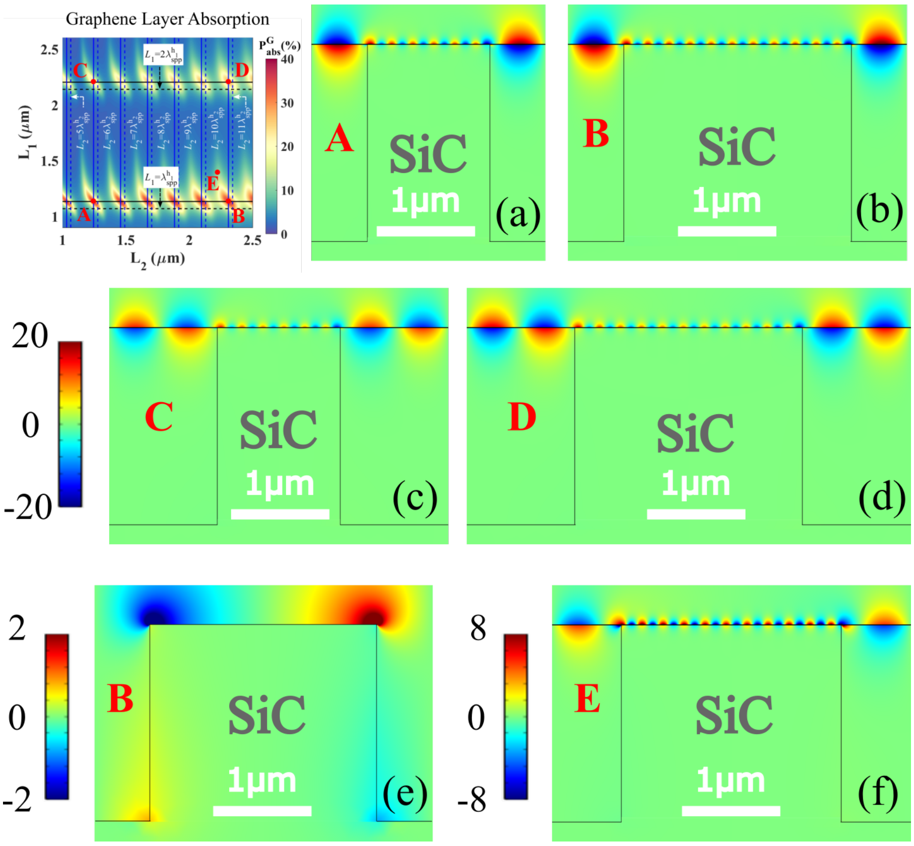

Figure 5.4: (a-d) Near-field distribution of E_z for three cases marked as points A, B, C, and D in Figure 5.3 which is re-sketched in this figure. The modes supported in the gap and the trench are different for those four cases. The corresponding parameters are as follows: (a) $L_1 = 1.135\mu m$ and $L_2 = 1.245\mu m$, (b) $L_1 = 1.135\mu m$ and $L_2 = 2.310\mu m$, (c) $L_1 = 2.205\mu m$ and $L_2 = 1.245\mu m$, (d) $L_1 = 2.205\mu m$ and $L_2 = 2.310\mu m$. The electric field is normalised to the incident field magnitude. The electric field distribution verifies the standing waves supported by the cavity. The same colorbar is used for those four plots. (e) Near-field distribution of E_z for the case marked as point B, but without the graphene layer, where $L_1 = 1.135\mu m$ and $L_2 = 1.245\mu m$. (f) Near-field distribution of E_z for the case marked as point E, where $L_1 = 1.410\mu m$ and $L_2 = 2.230\mu m$. The electric field is also normalised to the incident field magnitude. Different colorbars are used for the last two plots.

the behavior of the real part of ERI. In Figure 5.7a, we show the numerical results against the gap thickness and the ridge width. The accuracy of the proposed model was confirmed by the behavior graphene absorption. In this part, the gap thicknesses and ridge lengths are in the ranges of $0.001\mu m$ to $0.150\mu m$ and $1.00\mu m$ to $1.50\mu m$, respectively. As expected, the peak positions vary with the variation of the gap thickness and the ridge length. This confirms the dependence of the dispersion relation on the gap thickness and the proposed model. In Figure 5.7a, the strong graphene absorption still corresponds to the excitation of both standing waves in both cavities. This was confirmed by the near-field distributions for three cases with different geometries in Figure 5.7b-d. The predictions of strong absorption peak positions are also given using the proposed model (with and without modification), as the curves shown in Figure 5.7a.

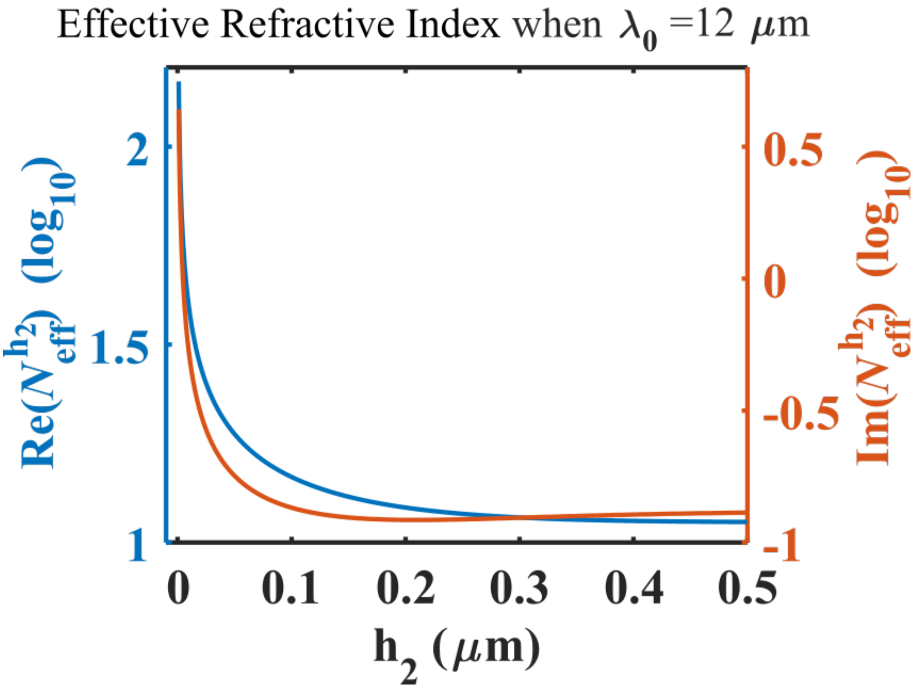

Figure 5.5: Real and imaginary parts of the ERI from Equation 4.14 against the gap thickness (h_2) for TM polarized, normal incidence light at a fixed wavelength $\lambda_0 = 12\mu m$, where media I and II are air, medium III is SiC, $L_1 = 1.135\mu m$ and $E_F = 0.64eV$.

The zoomed-in view confirms the accuracy of the theoretical prediction again. These findings enable us to make it possible to tune the cavity resonances by varying the geometric parameters, such as the trench length, ridge length, and gap thickness. In particular, the gap thickness can be used to efficiently tune the wavelength of the graphene plasmonic waves in the cavity above the gap. The tunability of such geometric parameters makes the system very versatile.

5.6 Simultaneous Implementation of Extremely High Enhancement and Extraordinary Compression

One interesting feature revealed in Figure 5.3 and Figure 5.4 is the extremely high enhancement and extraordinary compression of graphene plasmon waves in the cavity above the ridge. In Figure 5.8, we show the intensity distributions for three special cases. In the previous chapter, we have already shown that the electromagnetic field can be extraordinary compressed by being trapped in a very shallow cavity (the compression factor is about ~ 400) and high enhancement (~ 4000) of graphene plasmon waves could also be realized under certain conditions. However, those two phenomena could not appear in the same system. Thus, when designing the configuration in practice, we need to balance the confinement and the intensity of the field. In the current work, we achieve both extremely high enhancement (~ 10000) and extraordinary compression (the compression factor is about ~ 1000) in the same system. This

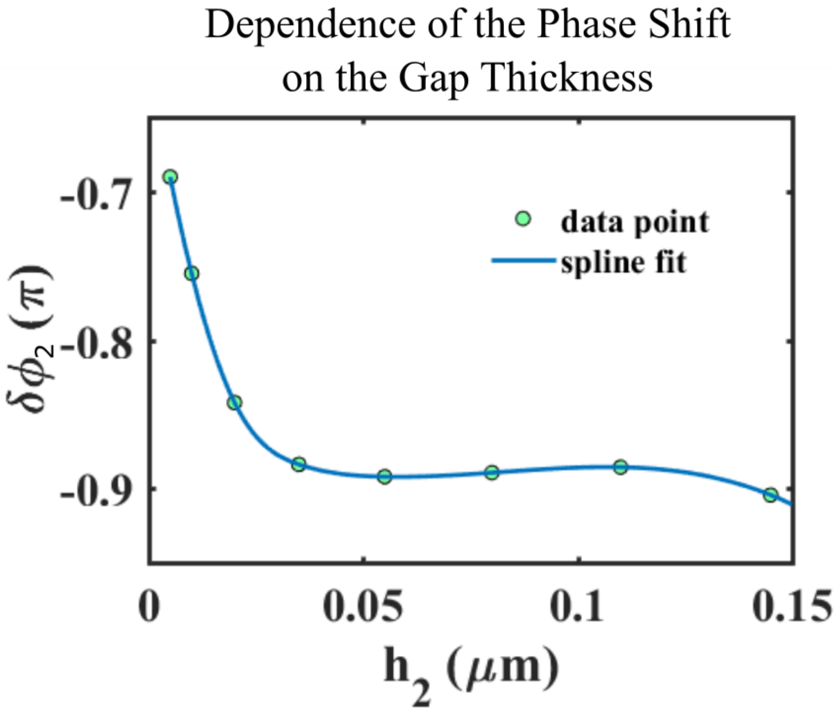

Figure 5.6: The dependence of the phase shift $\delta\phi_2$ on the gap thickness, for a TM polarized, normal incidence at a fixed wavelength $\lambda_0 = 12\mu m$, where media I and II are air, medium III is SiC, $L_1 = 1.135\mu m$ and $E_F = 0.64eV$. The data points are obtained from the numerical simulations. And the lines are obtained using the spline fit of the data points.

is because: (i) the very small gap above the ridge makes the extraordinary compression possible, and (ii) the optimized trench height hugely enhances the conversion efficiency. It should be noted that we could even achieve higher enhancement and more extraordinary compression by further optimizing the parameters of the system. Another interesting feature is that the intensity distributions in those two types of cavities (one is in the trench, and one is in the gap) are totally different. It can be understood that the electric intensity has two contributions, the x- and z-components of the electric field. From the previous study, we know that the vertical Fabry-Pérot effect dominates the contribution of the x-component, while the horizontal Fabry-Pérot effect dominates the contribution of the z-component. In the current work, both contributions in the trench cavity are strong, because of the optimized trench height. However, the contribution of the z-component dominates the intensity of the electric field in the gap above the ridge, because of the small gap thickness. This was confirmed by the intensity distribution in Figure 5.8. Interestingly, the energy is mainly trapped in the cavity above the ridge, even though the GPs in both types of cavities are excited. Most notably, compared to previous work, the extremely high field enhancement and extraordinary compression of GPs are achieved simultaneously, thanks to the combination of the shallow cavity and the deep cavity in the same configuration. The extremely high field enhancement is extraordinarily compressed in a very

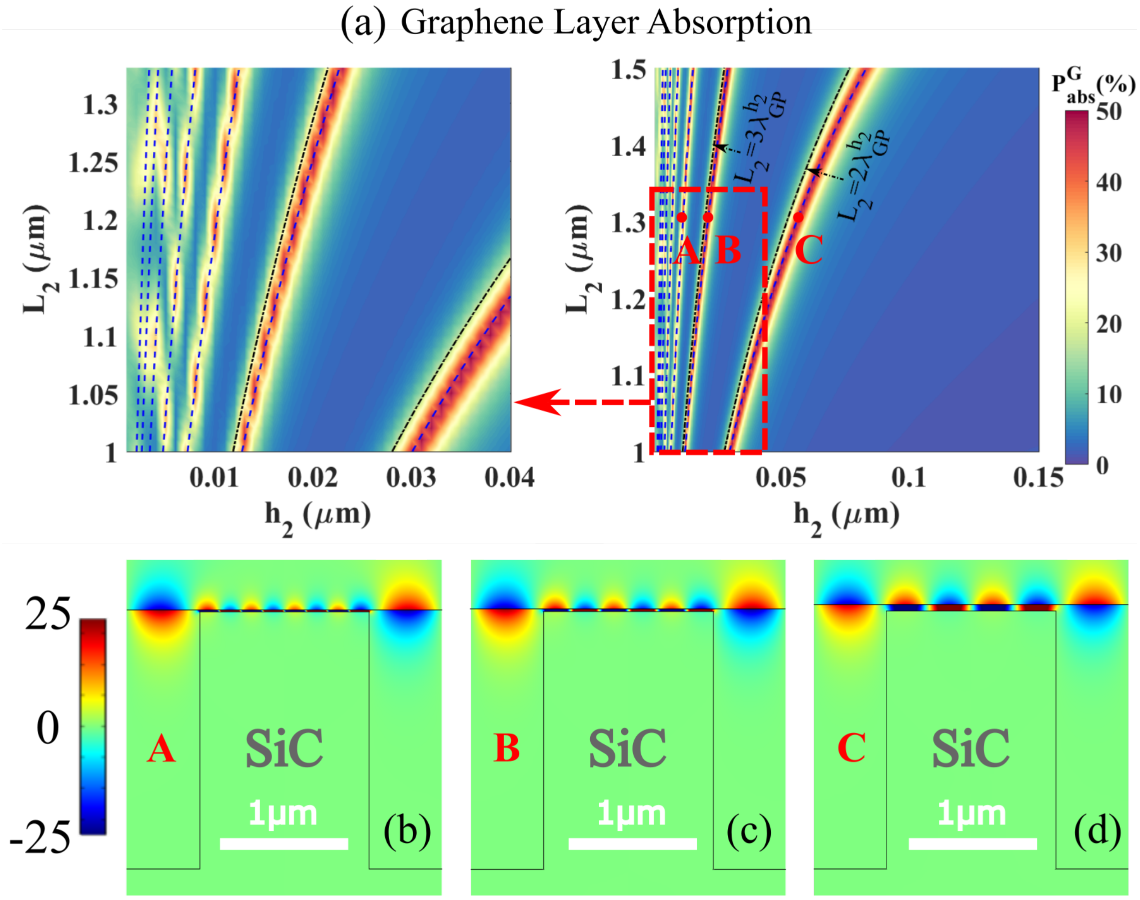

Figure 5.7: (a) Graphene layer absorption (P_{abs}^{G}) for the SiC grating plus graphene structure versus the ridge length (L_2) and the gap thickness (h_2). The black dash-dot curves indicate a fit to a Fabry-Pérot model for a phase shift of $-\pi$, while the blue dashed ones indicate a fit to a Fabry-Pérot model for a phase shift with values as Figure 5.6 shows. An zoomed-in view of the region in the red dashed box is also given. The blur is due to the step resolution in the simulation. (b-d) Near-field distribution of E_z for three cases marked as points A, B, and C in (a).The corresponding parameters are as follows: (b) $L_2 = 1.310\mu m$ and $h_2 = 0.012\mu m$, (c) $L_2 = 1.310\mu m$ and $h_2 = 0.022\mu m$, (d) $L_2 = 1.310\mu m$ and $h_2 = 0.058\mu m$. The electric field is normalised to the incident field magnitude. The same colorbar is used.

small region around the graphene layer providing high potential for applications in molecular sensors, solar cell and integrated optics.

5.7 Tunability of the Fermi Energy

Compared to the counterpart on the surface of metallic materials, graphene plasmonic modes are particularly appealing thanks to the ultra-broad and fast tunability of the Fermi energy via chemical doping or electrical doping. In this part, we will tune the peak positions in the absorption spectra by tuning the Fermi energy. The graphene absorption with a different Fermi energy is shown in Figure 5.9a. Compared to the results in Figure 5.3, one feature revealed in Figure 5.9a is that the ridge length and the trench length corresponding to each peak vary

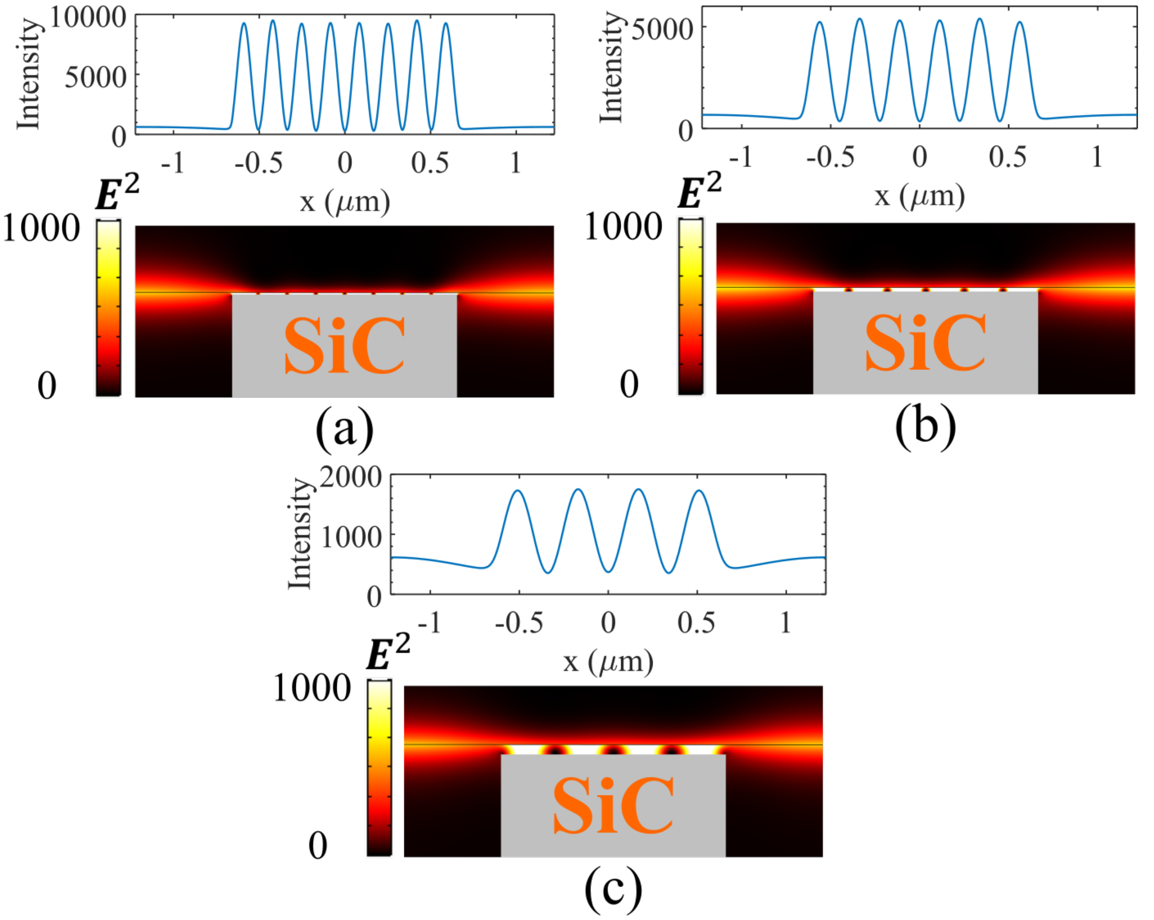

Figure 5.8: The extremely high intensity (E^2) distribution and the extraordinary compressed plasmonic waves trapped in the cavity above the ridge for three cases marked as points A, B, and C in Figure 5.6. The corresponding parameters are as follows: (a) $L_2 = 1.310\mu m$ and $h_2 = 0.012\mu m$, (b) $L_2 = 1.310\mu m$ and $h_2 = 0.022\mu m$, (c) $L_2 = 1.310\mu m$ and $h_2 = 0.058\mu m$. The enhancement around the graphene layer and the compression factor of λ_0/h_2 in those three cases are as follows: (a) 9521.0 and 1000, (b) 5408.2 and 545.5, (c) 1758.9 and 206.9. Distribution of the intensity along a line positioned at $0.5nm$ below graphene layer is given as well.

with the variation of the Fermi energy. This is because the dispersion relation of the graphene plasmonic waves strongly depends on the Fermi energy. The excellent agreement between the predictions and the numerical results confirms again the validation of the proposed model. It should be noted that the value of the phase shift $\delta\phi_i$ strongly depends on the Fermi energy of the graphene layer. The near-field plots for points marked as A and B in Figure 5.9a are given in Figure 5.9b and c. This feature makes the system a cheap, reliable, ultra-fast and highly tunable optical modulator.

5.8 Variation of the Refractive Index of the Filling Medium

The previous discussions only consider the free-standing graphene layer that served to simplify discussion and the understanding of the physical mechanism. In this part, we consider a simple

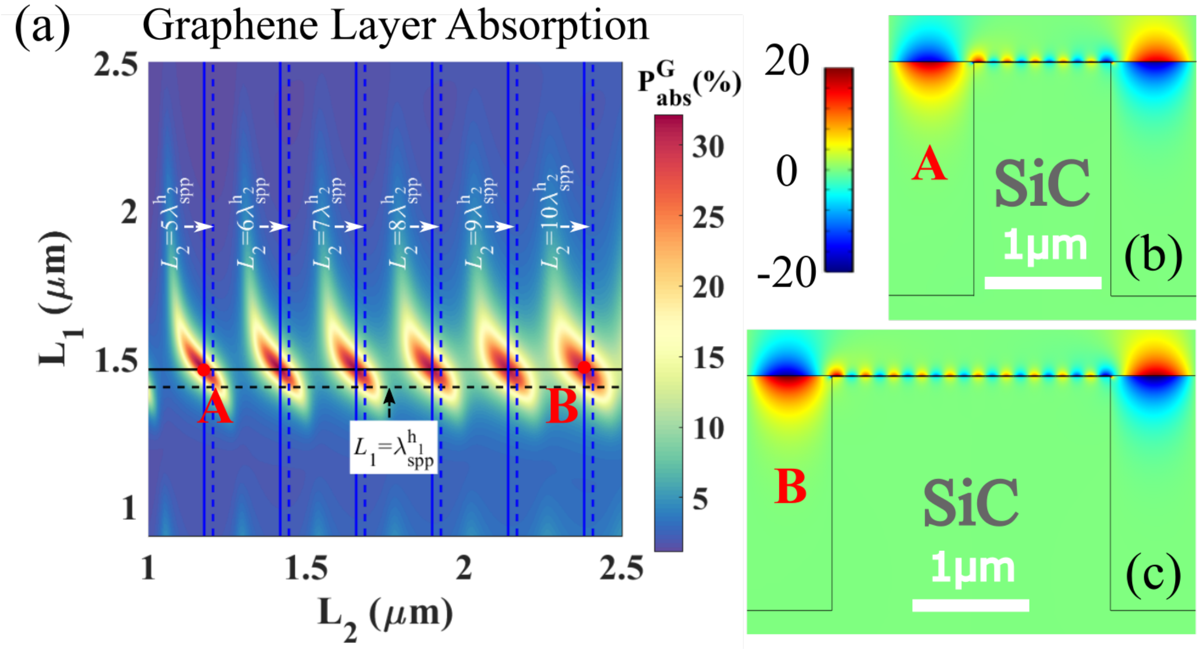

Figure 5.9: (a) Graphene layer absorption (P^G_{abs}) for the SiC grating plus graphene structure versus the trench length (L_1) and the ridge length (L_2), when the gap thickness is $0.005\mu m$. The normal incidence is TM polarized at a wavelength $\lambda_0 = 12\mu m$, where media I and II are air, medium III is SiC, and $E_{\mathrm{F}} = 0.84eV$. The dashed lines indicate a fit to a Fabry-Pérot model for a phase shift of $-\pi$. The black solid lines indicate a fit to a Fabry-Pérot model for a phase shift of -1.085π, while the blue solid ones indicate a fit to a Fabry-Pérot model for a phase shift of -0.77π. (b-c) Near-field distribution of E_z for three cases marked as points A and B in (a). The modes supported in the gap and the trench are different for those two cases. The corresponding parameters are as follows: (b) $L_1 = 1.461\mu m$ and $L_2 = 1.176\mu m$, (c) $L_1 = 1.461\mu m$ and $L_2 = 2.381\mu m$. The electric field is normalised to the incident field magnitude. The same colorbar is used.

but more realistic configuration: The gap above the ridge and the trench are filled with a dielectric medium with the refractive index n, which could be easily realized by depositing oxides or an organic layer in practice. As an example, we set $n = 1.5$, and analyze the graphene absorption and the excited modes, as shown in Figure 5.10. As expected, the peak positions still agree well with the predictions from Equation 4.14 shown in Figure 5.10a. It should be noted that the value of the phase shift $\delta\phi_i$ strongly depends on the refractive index n of the material in the gap and the trench. To verify the supporting modes, the near-field distribution of E_z for two cases marked as points A and B in Figure 5.10a is given in Figure 5.10b and c, which agrees excellently with the theoretical prediction. Another interesting feature is that the field intensity for those two cases is much lower than the case in Figure 5.3 and Figure 5.4 (where $n = 1$). This is mainly due to the fact that, in the trench, SPhPs are excited, and a vertical SiC Fabry-Pérot cavity is established. When the refractive index n of the dielectric medium changes, the condition (here, the trench height) of the Fabry-Pérot resonance would be different. When $n = 1$, the resonance exists for certain trench height, while the resonance disappears for the

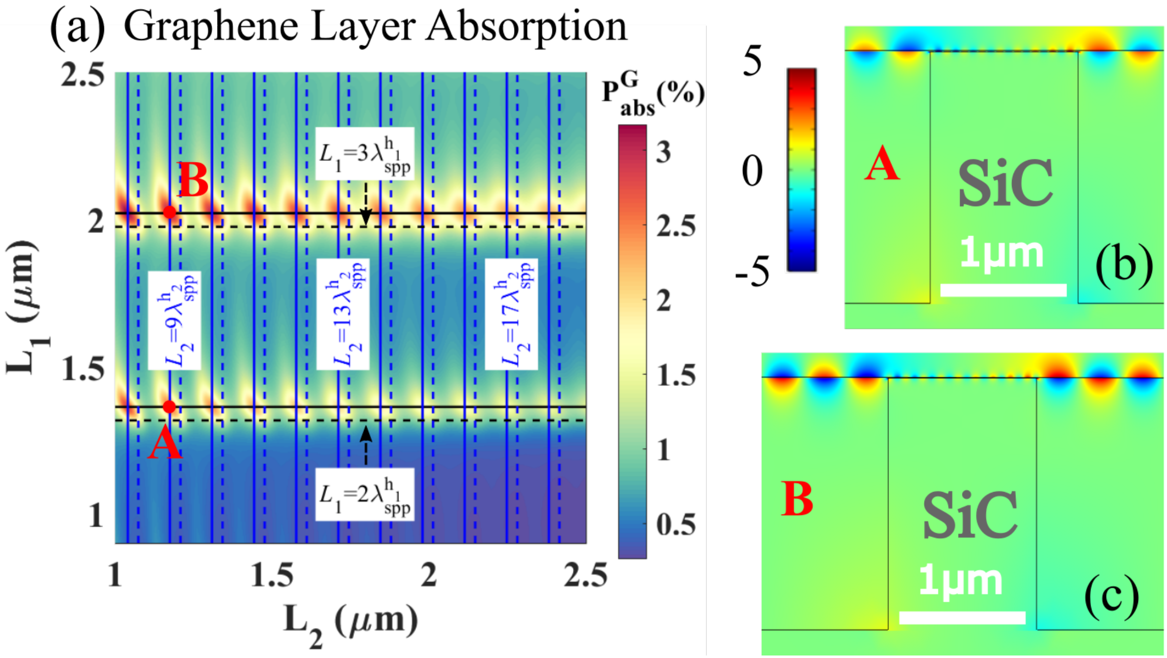

Figure 5.10: (a) Graphene layer absorption (P_{abs}^{G}) for the SiC grating plus graphene structure versus the trench length (L_1) and the ridge length (L_2), when the gap and the trench are filled with a dielectric medium with the refractive index $n = 1.5$. The normal incidence is TM polarized at a wavelength $\lambda_0 = 12\mu m$, where media I and II are air, medium III is SiC, $E_{\text{F}} = 0.64eV$, and the gap thickness is $0.005\mu m$. The dashed lines indicate a fit to a Fabry-Pérot model for a phase shift of $-\pi$. The black solid lines indicate a fit to a Fabry-Pérot model for a phase shift of -1.14π, while the blue solid ones indicatie a fit to a Fabry-Pérot model for a phase shift of -0.5π. (b) and (c) Near-field distribution of E_z for two cases marked as points A and B in (a). The corresponding parameters are as follows: (b) $L_1 = 1.363\mu m$ and $L_2 = 1.174\mu m$, (c) $L_1 = 2.021\mu m$ and $L_2 = 1.174\mu m$. The electric field is normalised to the incident field magnitude. The same colorbar is used those plots.

same trench height when $n = 1.5$. These findings confirm the validity of the established model, and could make the system a potential design for sensing and integrated optics.

5.9 Conclusions

In conclusion, we have established the model of suspended graphene plasmon cavities. In the proposed model, the Fabry-Pérot equation is used to predict the conditions for the GP resonance in two types of cavities (in the trench and above the ridge), and the dispersion relation of GPs in a general multilayer system is applied to calculate the GP wavelength at different values of the cavity height. The excellent agreement between the predictions from this proposed model and the numerical results confirms the validity of the proposed model. Remarkably, we also have achieved the extremely high field enhancement and extraordinary compression of GPs simultaneously, thanks to the combination of the shallow cavity and the deep cavity in the same configuration. The tunability of the Fermi energy and geometric parameters of the cavities make the design of this system very versatile. We expect the investigated system using the combination of the shallow and deep cavities to open up numerous potential applications in molecular sensors, solar cell and integrated optics.

CHAPTER 6

Conclusions & Future Outlook

6.1 Conclusions

In this section, we offer a summary of the work presented in this thesis.

First, we proposed tunable plasmonic cavities working at the mid-infrared frequencies using a monolayer of graphene deposited on a SiC grating. We observed that SiC behaves like a perfect conductor within the Reststrahlen band, providing a cavity effect to generate standing waves of graphene plasmon inside SiC cavities. We focused on establishing a simple model of such GPs cavities by considering a Fabry-Pérot model in the horizontal cavity direction. In this model, the commonly used dispersion relation of GPs was applied to calculate the wavevectors of GPs. In addition, we analysed the strong interaction between localized SPhPs of SiC and SPPs of graphene, revealed by a phenomenon called Rabi splitting.

Next, we revealed that there is an assumption in this commonly used dispersion relation: that the materials above and below the graphene layer are assumed to occupy the corresponding semi-infinite spaces. This assumption is valid when the SiC cavity is sufficiently deep ($> 500nm$), however, it fails when the cavity height is smaller than $500nm$. We derived an analytical expression for the dispersion relation in a multilayer system, illustrating the cavity height dependence. Base on this analytical expression, we improved the previously proposed Fabry-Pérot model in the horizontal direction. In addition, we observed a Fabry-Pérot effect in the vertical cavity direction. We even achieved complete absorption under certain parameters and realized the high enhancement and extraordinary compression of graphene plasmon waves.

Finally, we investigated the GPs in a graphene layer suspended above a SiC grating with a small gap between the two. Based on the derived dispersion relation, we established the model of the suspended graphene plasmon cavities, which was confirmed by the comparison between the theoretical results and the numerical ones. In addition, we successfully simultaneously excited

GPs with extremely high field enhancement and extraordinary field compression by combining a shallow cavity and a deep cavity in the same configuration.

All these findings pave the way to build simple tunable plasmonic structures, and make this system an ideal setup for various vital applications, such as photodetection, molecular sensing and integrated optics.

6.2 Outlook

On the basis of the existing work in this thesis, some of the most important research directions in this field are as follows:

1. **Explore new geometries and new frequencies.** Current studies usually focus on the simplest geometries such as rectangles and squares. However, because the optical behaviour of the system strongly depends on its structure, it is important to consider other geometries, such as Archimedean spiral slits [21] and closely spaced subwavelength apertures [153], that can be used to excite the GPs and to introduce special optical properties. On the other hand, metal plasmonics exist in the visible and near-infrared frequencies, enabling a number of applications, such as single molecule detection. Indeed, other ranges of frequencies could benefit from the high field enhancement and strong field confinement due to SPPs. For example, there is a high demand for molecular sensing at far-infrared frequencies [54, 154–156] and security detection at terahertz frequencies [157, 158]. Exploring new geometries and new frequencies could increase the versatility of plasmonic devices.

2. **Discover new material platforms.**

   The types of materials that are widely studied in plasmonics have largely fallen into two categories: noble metals and graphene. They work in different frequency ranges and exhibit different optical proprieties. Often, it is the use of a new material platform that enables existing technologies to find application in new domains. Therefore, there is still a great demand for discovering novel materials with distinguishing properties, such as low loss, high tunability and diffident operating frequencies, as constituents in plasmonics. For example, in the past few years, hexagonal boron nitride has emerged as a promising alternative. In addition, this material is a natural hyperbolic material, exhibiting an extreme optical property known as in-plane hyperbolicity. This material has great potential to lead to the highly integrated optical components in the infrared range.

3. **Investigate nonlinear effects in graphene plasmons.**

So far, metals are widely used in the study of nonlinear optical effects [159]. These nonlinear processes are usually intrinsically weak and strongly depend on the local field enhancement [160]. However, due to the nature of SPPs on metals, only the surface of the metals can be used and the field enhancement is very limited. There are two solutions: First, we could used the volume effect, which means dielectrics could be used to improve the conversion efficiency. However, this is out of the scope of this thesis. Second, we could hugely enhance the field enhancement by introducing new materials and new physical effects. As mentioned in this thesis, the extremely high field enhancement of GPs is observed, which could be applied in the study of nonlinear optical effects. It is worth noting that this strong enhancement could be extremely compressed in the gap, providing great nonlinear response (which could be used for the single-molecule detection).

4. **Propose applications and conduct experiments.**

   Certainly, practice is the sole criterion for testing truth. Current studies focus on the theoretical investigation, which could offer us the effective guidelines in the experiments. There exist some possible challenges: First, in the simulation, we did not consider the defects of graphene. However, until now the quality of graphene in the lab is still not perfect. Second, the fabrication of nanostructures is still very challenging, due to extreme hardness of the material used here (SiC is regarded as the second hardest material after diamond). Third, there is still less equipment in the detection in mid-infrared compared to the ones in visible. Overcoming these challenges will require the development of new technologies.

APPENDIX A

Finite Difference Time Domain

FDTD is a time domain method that is used to numerically solve Maxwell's equations with finite-difference approximations. It is intuitive to observe the evolution of fields over time and the transient response. In this appendix, we will introduce the main concept of this method.

A.1 Flow of Maxwell's Equations

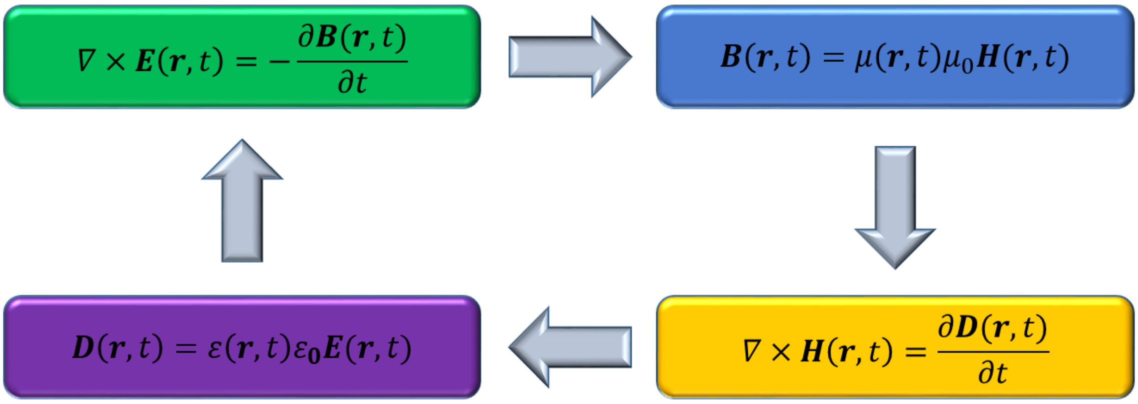

Figure A.1: Main concept of finite difference time domain. Here, we assume the materials involved in the system are linear, isotropic and non-dispersive. Otherwise, the permittivity and the permeability should be in the more general forms - the tensor forms ($[\epsilon(\mathbf{r},t)]$ and $[\mu(\mathbf{r},t)]$). In addition, the cases without external charge ($\rho_{ext} = 0$) and current ($\mathbf{J}_{ext} = 0$) densities are considered.

Maxwell's equations and constitutive relations provide a mathematical model of classical electromagnetism, forming the foundation of classical optics. In reality, the electric and magnetic fields are simultaneously coupled and evolving at the same time. However, in FDTD the evolution is approximated as a sequence of events as shown in Figure A.1: We will begin with the upper left box of the figure. First, we assume that the electric field $\mathbf{E}$ is known at a starting time point. Based on the Faraday's law, we update the magnetic induction $\mathbf{B}$ by calculating the curl of the electric field. Then, we calculate the magnetization field $\mathbf{H}$ through the constitutive relation. Later, the electric displacement $\mathbf{D}$ is updated by calculating the curl of the magnetization field, based on the Ampère's law. After that, the electric field $\mathbf{E}$ can be calculated by incorporating the material information through the constitutive relation. Now we know the electric field $\mathbf{E}$ again, however, it should be noted that this electric field $\mathbf{E}$ is at the next time point. We can carry on this process to evolve the fields forwards in time. Choosing a smaller time step can improve the accuracy of the evolution.

A.2 Approximating the Time-derivatives

In the previous section, we introduce the main concept of FDTD: the electric and magnetic fields are updated step by step. Here, we briefly describe how to approximate time-derivatives by applying finite-difference approximations. There are three forms of finite differences that are commonly used. They are forward, backward, and central differences. The central one is the most frequently selected one in FDTD. Therefore, the time derivatives of the magnetic induction and the electric displacement, $\frac{\partial \mathbf{B}}{\partial t}$ and $\frac{\partial \mathbf{D}}{\partial t}$, can be approximated by the following expressions in FDTD

$$\frac{\mathbf{B}(t+\frac{\Delta t}{2})-\mathbf{B}(t-\frac{\Delta t}{2})}{\Delta t}, \tag{A.1}$$

and

$$\frac{\mathbf{D}(t+\Delta t)-\mathbf{D}(t)}{\Delta t}. \tag{A.2}$$

The staggering of the magnetic induction and the electric displacement in time ensures that $\mathbf{B}$ and $\mathbf{H}$ exist at half time steps ($\Delta t/2$, $t+\Delta t/2$, $2t+\Delta t/2$,...), and $\mathbf{D}$ and $\mathbf{E}$ exist at integer time steps (0, Δt, $2\Delta t$,...).

Based on the Maxwell's equations, we can easily get the following "update equations"

$$\mathbf{B}|_{t+\Delta t/2} = \mathbf{B}|_{t-\Delta t/2} - \Delta t \nabla \times \mathbf{E}|_t, \tag{A.3}$$

and

$$\mathbf{D}|_{t+\Delta t} = \mathbf{D}|_t + \Delta t \nabla \times \mathbf{H}|_{t+\Delta t/2}, \tag{A.4}$$

Indeed, the curl of fields can also be treated using the finite-difference approximations. However, this is out the scope of this thesis, and thus it is not presented here.

A.3 Algorithm of Finite Difference Time Domain

In the previous section, we introduced the “update equations”, which are applied to calculate the fields at the next time step within the FDTD loop. There exist some other important parts in the FDTD algorithm, as shown in Figure A.2. At the very beginning, all fields are initialized to zero, and then we enter the FDTD loop. However, nothing interesting happens if there is no power enters the system. Therefore, we need to handle the electric and magnetic field sources at certain points during the simulation by overwriting some of the field values. Next, the simulation boundaries should be paid special attention according to different requirements. For example, it is very common to prevent reflections by padding the simulation with a fictional material that is both reflectionless and absorbing, known as a perfectly matched layer. Then, the simulation data must be recorded and the simulation status should be shown during the simulation. Once the condition of the cycle is satisfied, we should post-process the recoded data. We usually judge whether the condition is satisfied by judging whether the energy escapes from the simulation region. This is because in FDTD the source is a pulse and the energy must exist the system after some time. Thus, it is very inefficient for highly resonant devices. In the post-process, the Fourier transform is applied to the record data in order to get the results in the frequency domain.

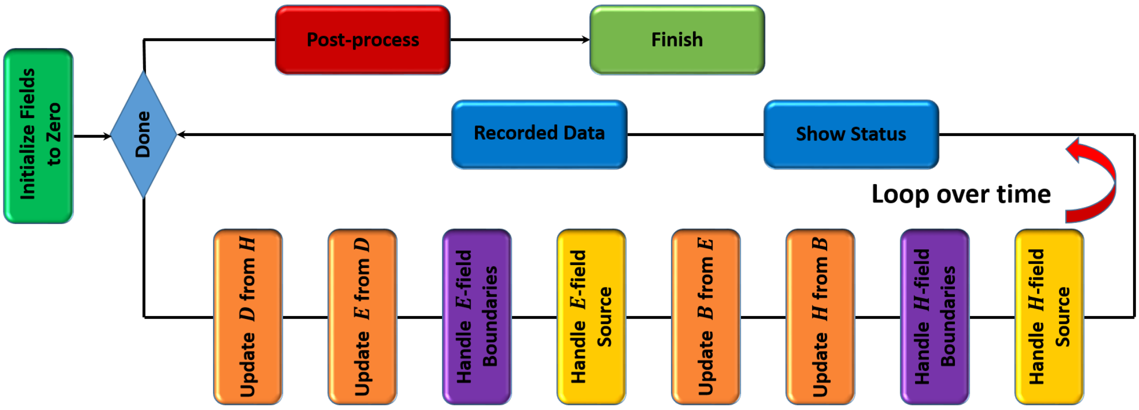

Figure A.2: Algorithm of finite difference time domain. The main concept of FDTD is shown in Figure A.1.

APPENDIX B

Finite Element Method

To describe laws of physics, scientists have established a number of mathematical models, which usually consist of partial differential equations. Although some analytical solutions exist (such as Mie theory for a sphere), these equations cannot be analytically solved. Therefore, different numerical approaches have been established to calculate approximate numerical solutions. Apart from FDTD, FEM is an excellent alternative and is frequently used to approximate solutions to boundary-value differential equations by discretizing the geometrical domain into a set of sub-domain elements. In this appendix, we will give an brief overview of FEM. Although FEM can also be used to solve time-domain problems, we will focus on frequency domain problems.

Although FEM is a versatile method that can be applied in a variety of fields, such as structural mechanics, heat transfer, fluid flow, acoustics, and chemical engineering, we illustrate the concept of FEM using a one-dimensional problem in electromagnetism here, as shown in Figure B.1. Considering the homogeneous material cases without external charge density ($\rho_{ext} = 0$) and considering the time-harmonic dependence of the electric field, we can combine the two curl-equations as follows

$$\nabla \times \nabla \times \mathbf{E} - \omega^2 \epsilon \epsilon_0 \mathbf{E} = i\omega \mathbf{J}. \tag{B.1}$$

Furthermore, when the invariance of the system in two directions is considered, this equation can be reduced to the following form

$$\frac{\partial^2 E_x}{\partial x^2} + \omega^2 \epsilon_x \epsilon_0 E_x = -i\omega J_x, \tag{B.2}$$

where E_x and ϵ_x are the x-component of the electric field and permittivity, respectively. Equation (B.2) is a strong form, because this equation holds for all points in the domain, Ω.

By assuming

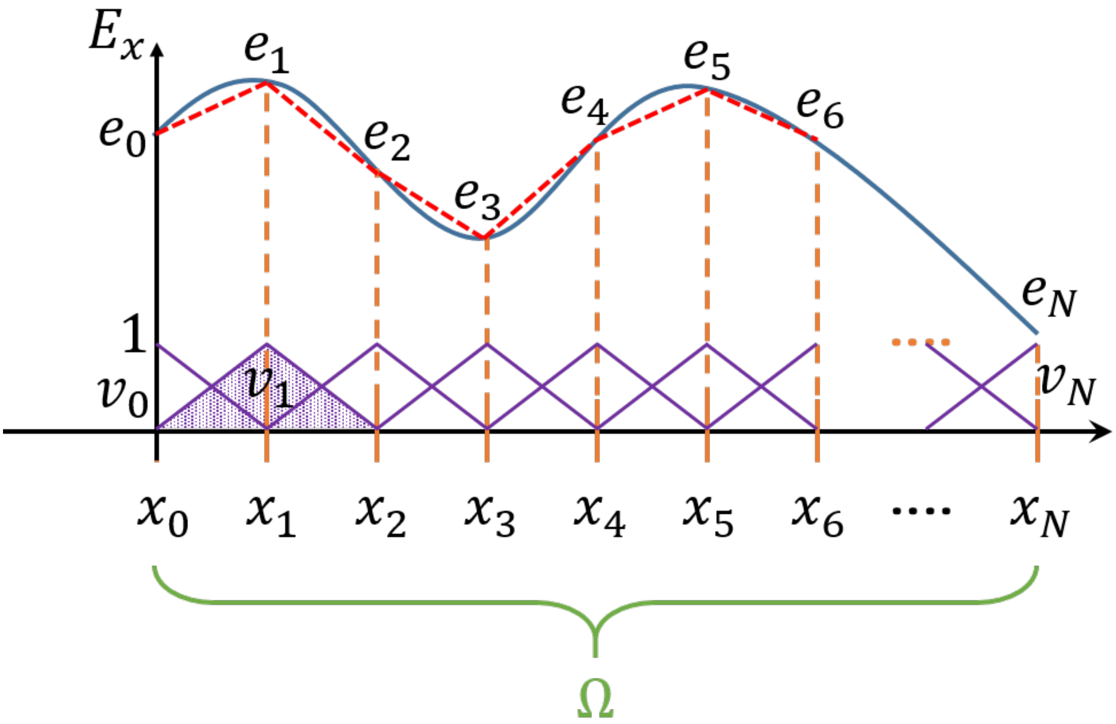

Figure B.1: Main concept of finite element method. The solid blue curve represents the exact solution that is denoted by a function E_x. The dashed red line represented by a approximation $\widetilde{E}_x$, which is a linear combination of a set of basis functions. These basis functions $\{v_i\}$ are denoted by the solid purple lines, and the coefficients are represented by $\{e_i\}$. The domain is denoted by a letter Ω.

$$\widetilde{E}_x \approx E_x, \tag{B.3}$$

we easily get

$$\frac{\partial^2 \widetilde{E}_x}{\partial x^2} + \omega^2 \epsilon_x \epsilon_0 \widetilde{E}_x + i\omega J_x = \mathrm{Res}(x) \neq 0, \tag{B.4}$$

where $\mathrm{Res}(x)$ denotes the residual. We assume that there exists a set of test functions $\{w_i\}$, and the projection of the residual onto the test functions vanishes

$$\int_\Omega \mathrm{Res}(x) \cdot w_i(x) \mathrm{d}x = 0. \tag{B.5}$$

By inserting the expression for $\mathrm{Res}(x)$, we get

$$\int_\Omega \left(\frac{\partial^2 \widetilde{E}_x}{\partial x^2} + \omega^2 \epsilon_x \epsilon_0 \widetilde{E}_x + i\omega J_x \right) w_i(x) \mathrm{d}x = 0 \tag{B.6}$$

We can split this equation into parts, and after integration by parts, we get

$$\omega^2 \int_\Omega \epsilon_x \epsilon_0 \widetilde{E}_x w_i \mathrm{d}x - \int_\Omega \frac{\partial \widetilde{E}_x}{\partial x}\frac{\partial w_i}{\partial x}\mathrm{d}x + [w_i \frac{\partial \widetilde{E}_x}{\partial x}]_{x_0}^{x_N} = -i\omega \int_\Omega J_x w_i(x)\mathrm{d}x. \tag{B.7}$$

This equation is a weak form, because this equation relaxes the requirements of Equation (B.2) by only requiring equality in an integral sense. With this weak formulation, we can transfer the mathematical model of this electromagnetism problem to a numerical model by discretizing the whole domain into sub-domains which is known as elements as shown in Figure B.1. This is why this method is known as the finite element method. We assume that $\widetilde{E}_x$ can be expressed as an expansion of a set of basis functions $\{v_i\}$

$$\widetilde{E}_x = \sum_{j=0}^{N} e_j v_j(x), \tag{B.8}$$

where e_j denotes the coefficients of the function. Once the coefficients here are calculated, the problem is solved. It should be noted that there are an infinite number of choices for the basis functions $\{v_i\}$ in theory. Therefore, we can get

$$\sum_{j=0}^{N}\left(\omega^2 \int_\Omega \epsilon_x \epsilon_0 w_i v_j \mathrm{d}x - \int_\Omega \frac{\partial w_i}{\partial x}\frac{\partial v_j}{\partial x}\mathrm{d}x + [w_i \frac{\partial v_i}{\partial x}]_{x_0}^{x_N}\right) e_j = -i\omega \int_\Omega J_x w_i(x)\mathrm{d}x. \tag{B.9}$$

This equation can be expressed in a matrix-form when considering

$$\mathbf{M} \rightarrow \{M_{ij}\}, \mathbf{S} \rightarrow \{S_{ij}\}, \mathbf{G} \rightarrow \{G_{ij}\}, \mathbf{e} \rightarrow \{e_j\}, \mathbf{F} \rightarrow \{F_j\}, \tag{B.10}$$

where

$$M_{ij} = \int_\Omega \epsilon_x \epsilon_0 w_i v_j \mathrm{d}x, \tag{B.11}$$

$$S_{ij} = \int_\Omega \frac{\partial w_i}{\partial x}\frac{\partial v_j}{\partial x}\mathrm{d}x, \tag{B.12}$$

$$G_{ij} = [w_i \frac{\partial v_i}{\partial x}]_{x_0}^{x_N}, \tag{B.13}$$

$$F_j = -i\omega \int_\Omega J_x w_i(x)\mathrm{d}x. \tag{B.14}$$

$\mathbf{M}$ consists of the material parameters of the system, and thus it is often referred to as the material matrix. $\mathbf{S}$ only contains the spatial derivative of the test and basis functions, and therefore it is called as the stiffness matrix. $\mathbf{G}$ includes the boundary conditions. $\mathbf{e}$ is the vector of unknowns, containing all the values of the electric field. $\mathbf{F}$ represents the source. Then, Equation (B.9) can be expressed in the following compact form

$$(\omega^2 \mathbf{M} - \mathbf{S} + \mathbf{G})\mathbf{e} = \mathbf{F}. \tag{B.15}$$

We note that this matrix-equation can be easily solved, because the elements of $\mathbf{M}$, $\mathbf{S}$, $\mathbf{G}$, and $\mathbf{F}$ are known quantities which can be easily calculated in most case, and the test and basis functions can be properly selected. Sometime, the source $\mathbf{F}$ is not known, Equation (B.15) can be simplified into a form for a generalized eigenvalue problem as follows

$$(\mathbf{S} - \mathbf{G})\mathbf{e} = \omega^2 \mathbf{M}\mathbf{e}. \tag{B.16}$$

According to the above, the basic step in FEM formulation can summarized as follows: First, a strong formulation is established. Second, we derive the weak formulation based on the strong formulation. Third, approximations for unknown functions is chosen. Fourth, basis functions are properly selected. Finally, we numerically compute the unknowns by solving the matrix-equation. Although there exist many technical details at each step, these are outside of the scope of this thesis.

APPENDIX C

Fabry-Pérot Model

In this appendix, we will briefly introduce the Fabry-Pérot cavity and the Fabry-Pérot model.

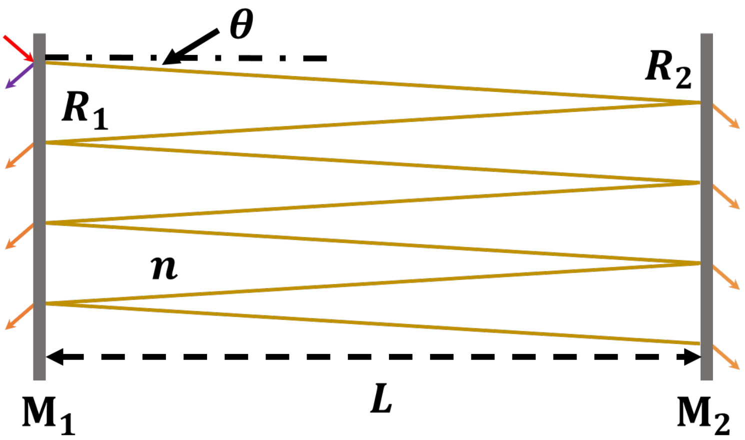

Figure C.1: Sketch of a Fabry-Pérot cavity: this cavity consists of two two optical reflectors, M_1 and M_2, with a distance L. The reflectivities of the two reflectors are R_1 and R_2, and the corresponding transmissions are given as $T_1 = 1 - R_1$ and $T_2 = 1 - R_2$. The cavity is filled with a material with the reflective index n and absorption coefficient α. A plane wave propagates with an angle θ relative to the reflector normal.

A Fabry-Pérot cavity, also known as a Fabry-Pérot resonator, a Fabry-Pérot interferometer, or a Fabry-Pérot interferometer etalon, is a linear optical cavity consisting of two plane parallel optical reflectors with high reflection as shown in Figure C.1. The two reflectors are denoted as M_1 and M_2 and with reflectivities R_1 and R_2. The cavity has a thickness L and is filled with a material with the reflective index n and absorption coefficient α. In Figure C.1, we consider a plane wave with a wavelength λ_0 propagating in the cavity at a angle θ relative to the reflector normal. Due to the multiple reflection at the surfaces of the two reflectors, those multiple reflected fields will interfere within the cavity. Assuming a electric field E_i is modified to become E_{i+1} after one round trip in the cavity, the two electric fields has the following relation

$$E_{i+1} = r\exp(i\Phi)E_i, \tag{C.1}$$

with

$$r = (R_1R_2)^{1/2}\exp[-2(\alpha/2)L/\cos\theta], \tag{C.2}$$

and

$$\Phi = \frac{2\pi}{\lambda_0}2nLcos\theta + \delta\phi_1 + \delta\phi_2, \tag{C.3}$$

where $\delta\phi_1$ and $\delta\phi_2$ are the phase changes due to the complex reflection amplitudes at the two reflectors. Considering the interference between the multiple reflections, we can get total field E inside the cavity as follows

$$E = \sum_{i=1}^{\infty} E_i = \frac{E_1}{1 - r\exp(i\Phi)}. \tag{C.4}$$

Therefore, we could easily obtain the field intensity inside the cavity

$$\begin{aligned} I &= |E|^2 && \text{(C.5)} \\ &= \frac{I_1}{(1 - r\cos\Phi)^2 + r^2\sin\Phi^2} && \text{(C.6)} \\ &= \frac{I_1/(1-r)^2}{1 + (2F/\pi)^2\sin^2(\Phi/2)}, && \text{(C.7)} \end{aligned}$$

with

$$F = \frac{\pi r^{1/2}}{1 - r}, \tag{C.8}$$

where F denotes the finesse of the Fabry-Pérot Cavity. This equation demonstrates that the field intensity I inside the cavity is a periodic function of Φ with a period 2π. When the finesse F is large enough, the intensity I becomes a periodic function with sharp peaks positioned at $\Phi = 2m\pi$, where m is an natural number denoting the resonance mode order. It should be noted that constructive interference occurs and standing waves form within the cavity when this condition is fulfilled.

In our case, the following assumptions are satisfied: First, there is no difference between the two reflectors, meaning $R_1 = R_2 = R$ and $\delta\phi_1 = \delta\phi_2 = \delta\phi$. Second, the refractive index in the cavity is indeed the effective reflective index $\Re\{N_{\text{eff}}\}$ in our case. Third, the wave inside the cavity propagates perpendicular to the surfaces of the two reflectors, meaning $\theta = 0^o$. Therefore, we arrive at the well-known Fabry-Pérot model,

$$\delta\phi + \frac{2\pi}{\lambda_0}\Re\{N_{\text{eff}}\}L = m\pi. \tag{C.9}$$

The transmission spectra through such Fabry-Pérot cavities exhibit sharp resonances, and hence the Fabry-Pérot cavity is often used as an optical filter. For example, it can be used in a optical spectrometer to improve the spectrum resolution of the setup.

Although the mirrors included in the strict definition of the Fabry-Pérot interferometer should be two planar mirrors, this term has already been frequently used for resonators with any curved mirrors. In addition, when the cavity is filled with gain materials, the amplitude of the field will be amplified. Indeed, the Fabry-Pérot model is a significantly important concept in the field of laser. However, this is out the scope of this thesis.

References

[1] Stefan Alexander Maier. *Plasmonics: fundamentals and applications*. Springer Science & Business Media, 2007.

[2] Surbhi Lal, Stephan Link, and Naomi J Halas. Nano-optics from sensing to waveguiding. *Nature photonics*, 1(11):641, 2007.

[3] Jon A Schuller, Edward S Barnard, Wenshan Cai, Young Chul Jun, Justin S White, and Mark L Brongersma. Plasmonics for extreme light concentration and manipulation. *Nature materials*, 9(3):193, 2010.

[4] Rashid Zia, Jon A Schuller, Anu Chandran, and Mark L Brongersma. Plasmonics: the next chip-scale technology. *Materials today*, 9(7-8):20–27, 2006.

[5] Amanda J Haes and Richard P Van Duyne. A unified view of propagating and localized surface plasmon resonance biosensors. *Analytical and bioanalytical chemistry*, 379(7-8):920–930, 2004.

[6] William L Barnes, Alain Dereux, and Thomas W Ebbesen. Surface plasmon subwavelength optics. *nature*, 424(6950):824, 2003.

[7] Xiaofei Xiao, Benfeng Bai, and Ninghan Xu. Dual-wavelength extinction method for fast sizing of metal nanosphere ensembles. *Applied optics*, 54(24):7160–7168, 2015.

[8] Dmitri K Gramotnev and Sergey I Bozhevolnyi. Nanofocusing of electromagnetic radiation. *Nature Photonics*, 8(1):13, 2014.

[9] Dmitri K Gramotnev and Sergey I Bozhevolnyi. Plasmonics beyond the diffraction limit. *Nature photonics*, 4(2):83, 2010.

[10] Jeffrey N Anker, W Paige Hall, Olga Lyandres, Nilam C Shah, Jing Zhao, and Richard P Van Duyne. Biosensing with plasmonic nanosensors. *Nature Materials*, 7(6):442–453, 2008.

[11] Peter Zijlstra, Pedro MR Paulo, and Michel Orrit. Optical detection of single non-absorbing molecules using the surface plasmon resonance of a gold nanorod. *Nature nanotechnology*, 7(6):379, 2012.

[12] D Derkacs, SH Lim, P Matheu, W Mar, and ET Yu. Improved performance of amorphous silicon solar cells via scattering from surface plasmon polaritons in nearby metallic nanoparticles. *Applied Physics Letters*, 89(9):093103, 2006.

[13] Harry A Atwater and Albert Polman. Plasmonics for improved photovoltaic devices. *Nature materials*, 9(3):205, 2010.

[14] S Pillai, KR Catchpole, T Trupke, and MA Green. Surface plasmon enhanced silicon solar cells. *Journal of applied physics*, 101(9):093105, 2007.

[15] Lingling Huang, Xianzhong Chen, Benfeng Bai, Qiaofeng Tan, Guofan Jin, Thomas Zentgraf, and Shuang Zhang. Helicity dependent directional surface plasmon polariton excitation using a metasurface with interfacial phase discontinuity. *Light: Science & Applications*, 2(3):e70, 2013.

[16] Nina Meinzer, William L Barnes, and Ian R Hooper. Plasmonic meta-atoms and metasurfaces. *Nature Photonics*, 8(12):889, 2014.

[17] Anatoly V Zayats and Igor I Smolyaninov. Near-field photonics: surface plasmon polaritons and localized surface plasmons. *Journal of Optics A: Pure and Applied Optics*, 5(4):S16, 2003.

[18] Xin Guo, Min Qiu, Jiming Bao, Benjamin J Wiley, Qing Yang, Xining Zhang, Yaoguang Ma, Huakang Yu, and Limin Tong. Direct coupling of plasmonic and photonic nanowires for hybrid nanophotonic components and circuits. *Nano letters*, 9(12):4515–4519, 2009.

[19] Zhenglong Zhang, Yurui Fang, Wenhui Wang, Li Chen, and Mengtao Sun. Propagating surface plasmon polaritons: towards applications for remote-excitation surface catalytic reactions. *Advanced Science*, 3(1):1500215, 2016.

[20] Vincenzo Amendola, Roberto Pilot, Marco Frasconi, Onofrio M Marago, and Maria Antonia Iati. Surface plasmon resonance in gold nanoparticles: a review. *Journal of Physics: Condensed Matter*, 29(20):203002, 2017.

[21] G Spektor, D Kilbane, AK Mahro, B Frank, S Ristok, L Gal, P Kahl, D Podbiel, S Mathias, H Giessen, et al. Revealing the subfemtosecond dynamics of orbital angular momentum in nanoplasmonic vortices. *Science*, 355(6330):1187–1191, 2017.

[22] Francesco Bonaccorso, Z Sun, Ta Hasan, and AC Ferrari. Graphene photonics and optoelectronics. *Nature photonics*, 4(9):611, 2010.

[23] Qiaoliang Bao and Kian Ping Loh. Graphene photonics, plasmonics, and broadband optoelectronic devices. *ACS nano*, 6(5):3677–3694, 2012.

[24] Philippe Tassin, Thomas Koschny, Maria Kafesaki, and Costas M Soukoulis. A comparison of graphene, superconductors and metals as conductors for metamaterials and plasmonics. *Nature Photonics*, 6(4):259, 2012.

[25] F Javier García de Abajo. Graphene nanophotonics. *Science*, 339(6122):917–918, 2013.

[26] Taiichi Otsuji, Vyacheslav Popov, and Victor Ryzhii. Active graphene plasmonics for terahertz device applications. *Journal of Physics D: Applied Physics*, 47(9):094006, 2014.

[27] Tobias Stauber. Plasmonics in dirac systems: from graphene to topological insulators. *Journal of Physics: Condensed Matter*, 26(12):123201, 2014.

[28] Naresh Kumar Emani, Alexander V Kildishev, Vladimir M Shalaev, and Alexandra Boltasseva. Graphene: a dynamic platform for electrical control of plasmonic resonance. *Nanophotonics*, 4(1):214–223, 2015.

[29] Shenyang Huang, Chaoyu Song, Guowei Zhang, and Hugen Yan. Graphene plasmonics: physics and potential applications. *Nanophotonics*, 6(6):1191–1204, 2016.

[30] Rong Wang, Xin-Gang Ren, Ze Yan, Li-Jun Jiang, EI Wei, and Guang-Cun Shan. Graphene based functional devices: A short review. *Frontiers of Physics*, 14(1):13603, 2019.

[31] Xiaoyong He. Tunable terahertz graphene metamaterials. *Carbon*, 82:229–237, 2015.

[32] Hugen Yan, Xuesong Li, Bhupesh Chandra, George Tulevski, Yanqing Wu, Marcus Freitag, Wenjuan Zhu, Phaedon Avouris, and Fengnian Xia. Tunable infrared plasmonic devices using graphene/insulator stacks. *Nature nanotechnology*, 7(5):330, 2012.

[33] Frank HL Koppens, Darrick E Chang, and F Javier García de Abajo. Graphene plasmonics: a platform for strong light–matter interactions. *Nano letters*, 11(8):3370–3377, 2011.

[34] Hugen Yan, Zhiqiang Li, Xuesong Li, Wenjuan Zhu, Phaedon Avouris, and Fengnian Xia. Infrared spectroscopy of tunable dirac terahertz magneto-plasmons in graphene. *Nano letters*, 12(7):3766–3771, 2012.

[35] Zhe Fei, AS Rodin, GO Andreev, W Bao, AS McLeod, M Wagner, LM Zhang, Z Zhao, M Thiemens, G Dominguez, et al. Gate-tuning of graphene plasmons revealed by infrared nano-imaging. *Nature*, 487(7405):82, 2012.

[36] J. N. Chen, M. Badioli, P. Alonso-Gonzalez, S. Thongrattanasiri, F. Huth, J. Osmond, M. Spasenovic, A. Centeno, A. Pesquera, P. Godignon, A. Z. Elorza, N. Camara, F. J. G. de Abajo, R. Hillenbrand, and F. H. L. Koppens. Optical nano-imaging of gate-tunable graphene plasmons. *Nature*, 487(7405):77–81, 2012.

[37] Stefan A Maier. *World Scientific Handbook of Metamaterials and Plasmonics*. World Scientific Publishing Company Pte. Limited, 2018.

[38] Andrea C Ferrari, Francesco Bonaccorso, Vladimir Fal'Ko, Konstantin S Novoselov, Stephan Roche, Peter Bøggild, Stefano Borini, Frank HL Koppens, Vincenzo Palermo, Nicola Pugno, et al. Science and technology roadmap for graphene, related two-dimensional crystals, and hybrid systems. *Nanoscale*, 7(11):4598–4810, 2015.

[39] Stefan A Maier, Mark L Brongersma, Pieter G Kik, Scheffer Meltzer, Ari AG Requicha, and Harry A Atwater. Plasmonics-a route to nanoscale optical devices. *Advanced Materials*, 13(19):1501–1505, 2001.

[40] Sung-Gyu Park, ChaeWon Mun, Xiaofei Xiao, Avi Braun, Sunho Kim, Vincenzo Giannini, Stefan A Maier, and Dong-Ho Kim. Surface energy-controlled sers substrates for molecular concentration at plasmonic nanogaps. *Advanced Functional Materials*, 27(41):1703376, 2017.

[41] Xiaokun Wang, Sung-Gyu Park, Juhui Ko, Xiaofei Xiao, Vincenzo Giannini, Stefan A Maier, Dong-Ho Kim, and Jaebum Choo. Sensitive and reproducible immunoassay of multiple mycotoxins using surface-enhanced raman scattering mapping on 3d plasmonic nanopillar arrays. *Small*, 14(39):1801623, 2018.

[42] Alexandra Boltasseva, Thomas Nikolajsen, Kristjan Leosson, Kasper Kjaer, Morten S Larsen, and Sergey I Bozhevolnyi. Integrated optical components utilizing long-range surface plasmon polaritons. *Journal of Lightwave technology*, 23(1):413, 2005.

[43] Allen Taflove and Susan C Hagness. *Computational electrodynamics: the finite-difference time-domain method*. Artech house, 2005.

[44] Karl S Kunz and Raymond J Luebbers. *The finite difference time domain method for electromagnetics*. CRC press, 1993.

[45] Raymond Rumpf. Design and optimization of nano-optical elements by coupling fabrication to optical behavior. 2006.

[46] Raymond C Rumpf. Simple implementation of arbitrarily shaped total-field/scattered-field regions in finite-difference frequency-domain. *Progress In Electromagnetics Research*, 36:221–248, 2012.

[47] Jian-Ming Jin. *The finite element method in electromagnetics*. John Wiley & Sons, 2015.

[48] Anastasis C Polycarpou. Introduction to the finite element method in electromagnetics. *Synthesis Lectures on Computational Electromagnetics*, 1(1):1–126, 2005.

[49] Kostya S Novoselov, Andre K Geim, Sergei V Morozov, D Jiang, Y_ Zhang, Sergey V Dubonos, Irina V Grigorieva, and Alexandr A Firsov. Electric field effect in atomically thin carbon films. *Science*, 306(5696):666–669, 2004.

[50] F Javier Garcia de Abajo. Graphene plasmonics: challenges and opportunities. *Acs Photonics*, 1(3):135–152, 2014.

[51] Chengzhou Zhu, Dan Du, and Yuehe Lin. Graphene and graphene-like 2d materials for optical biosensing and bioimaging: a review. *2D Materials*, 2(3):032004, 2015.

[52] Kin Fai Mak and Jie Shan. Photonics and optoelectronics of 2d semiconductor transition metal dichalcogenides. *Nature Photonics*, 10(4):216–226, 2016.

[53] Mohammad M Jadidi, Andrei B Sushkov, Rachael L Myers-Ward, Anthony K Boyd, Kevin M Daniels, D Kurt Gaskill, Michael S Fuhrer, H Dennis Drew, and Thomas E Murphy. Tunable terahertz hybrid metal–graphene plasmons. *Nano letters*, 15(10):7099–7104, 2015.

[54] Daniel Rodrigo, Odeta Limaj, Davide Janner, Dordaneh Etezadi, F Javier García De Abajo, Valerio Pruneri, and Hatice Altug. Mid-infrared plasmonic biosensing with graphene. *Science*, 349(6244):165–168, 2015.

[55] Hai Hu, Xiaoxia Yang, Feng Zhai, Debo Hu, Ruina Liu, Kaihui Liu, Zhipei Sun, and Qing Dai. Far-field nanoscale infrared spectroscopy of vibrational fingerprints of molecules with graphene plasmons. *Nature communications*, 7:12334, 2016.

[56] Zhe Fei, Gregory O Andreev, Wenzhong Bao, Lingfeng M Zhang, Alexander S. McLeod, Chen Wang, Margaret K Stewart, Zeng Zhao, Gerardo Dominguez, Mark Thiemens, et al. Infrared nanoscopy of dirac plasmons at the graphene–sio2 interface. *Nano letters*, 11(11):4701–4705, 2011.

[57] Andre Konstantin Geim. Graphene: status and prospects. *science*, 324(5934):1530–1534, 2009.

[58] IW Frank, David M Tanenbaum, Arend M van der Zande, and Paul L McEuen. Mechanical properties of suspended graphene sheets. *Journal of Vacuum Science & Technology B: Microelectronics and Nanometer Structures Processing, Measurement, and Phenomena*, 25(6):2558–2561, 2007.

[59] Phaedon Avouris. Graphene: electronic and photonic properties and devices. *Nano letters*, 10(11):4285–4294, 2010.

[60] AH Castro Neto, Francisco Guinea, Nuno MR Peres, Kostya S Novoselov, and Andre K Geim. The electronic properties of graphene. *Reviews of modern physics*, 81(1):109, 2009.

[61] Eun-Ah Kim and AH Castro Neto. Graphene as an electronic membrane. *EPL (Europhysics Letters)*, 84(5):57007, 2008.

[62] Yanwu Zhu, Shanthi Murali, Weiwei Cai, Xuesong Li, Ji Won Suk, Jeffrey R Potts, and Rodney S Ruoff. Graphene and graphene oxide: synthesis, properties, and applications. *Advanced materials*, 22(35):3906–3924, 2010.

[63] Jianing Chen, Michela Badioli, Pablo Alonso-González, Sukosin Thongrattanasiri, Florian Huth, Johann Osmond, Marko Spasenović, Alba Centeno, Amaia Pesquera, Philippe Godignon, et al. Optical nano-imaging of gate-tunable graphene plasmons. *Nature*, 487(7405):77, 2012.

[64] Alexander A Balandin, Suchismita Ghosh, Wenzhong Bao, Irene Calizo, Desalegne Teweldebrhan, Feng Miao, and Chun Ning Lau. Superior thermal conductivity of single-layer graphene. *Nano letters*, 8(3):902–907, 2008.

[65] Viktoryia Shautsova, Themistoklis Sidiropoulos, Xiaofei Xiao, Nicholas A Güsken, Nicola CG Black, Adam M Gilbertson, Vincenzo Giannini, Stefan A Maier, Lesley F Cohen, and Rupert F Oulton. Plasmon induced thermoelectric effect in graphene. *Nature communications*, 9(1):5190, 2018.

[66] Bin Shen, Wentao Zhai, and Wenge Zheng. Ultrathin flexible graphene film: an excellent thermal conducting material with efficient emi shielding. *Advanced Functional Materials*, 24(28):4542–4548, 2014.

[67] *https://www.cen.dtu.dk/research/projects/actual-high-resolution-tem-on-graphene*.

[68] EH Hwang and S Das Sarma. Dielectric function, screening, and plasmons in two-dimensional graphene. *Physical Review B*, 75(20):205418, 2007.

[69] Sukosin Thongrattanasiri, Alejandro Manjavacas, and F Javier García de Abajo. Quantum finite-size effects in graphene plasmons. *Acs Nano*, 6(2):1766–1775, 2012.

[70] Yan Francescato, Vincenzo Giannini, and Stefan A Maier. Strongly confined gap plasmon modes in graphene sandwiches and graphene-on-silicon. *New Journal of Physics*, 15(6):063020, 2013.

[71] Ashkan Vakil and Nader Engheta. Transformation optics using graphene. *Science*, 332(6035):1291–1294, 2011.

[72] Yu Yao, Raji Shankar, Mikhail A Kats, Yi Song, Jing Kong, Marko Loncar, and Federico Capasso. Electrically tunable metasurface perfect absorbers for ultrathin mid-infrared optical modulators. *Nano letters*, 14(11):6526–6532, 2014.

[73] Zhaoyi Li and Nanfang Yu. Modulation of mid-infrared light using graphene-metal plasmonic antennas. *Applied Physics Letters*, 102(13):131108, 2013.

[74] Yuanjian Zhang, Toshiyuki Mori, Li Niu, and Jinhua Ye. Non-covalent doping of graphitic carbon nitride polymer with graphene: controlled electronic structure and enhanced optoelectronic conversion. *Energy & Environmental Science*, 4(11):4517–4521, 2011.

[75] JR Williams, Tony Low, MS Lundstrom, and CM Marcus. Gate-controlled guiding of electrons in graphene. *Nature Nanotechnology*, 6(4):222, 2011.

[76] Ignacio Llatser, Christian Kremers, Albert Cabellos-Aparicio, Josep Miquel Jornet, Eduard Alarcón, and Dmitry N Chigrin. Graphene-based nano-patch antenna for terahertz radiation. *Photonics and Nanostructures-Fundamentals and Applications*, 10(4):353–358, 2012.

[77] SA Mikhailov and K Ziegler. New electromagnetic mode in graphene. *Physical review letters*, 99(1):016803, 2007.

[78] Rahul Raveendran Nair, Peter Blake, Alexander N Grigorenko, Konstantin S Novoselov, Tim J Booth, Tobias Stauber, Nuno MR Peres, and Andre K Geim. Fine structure constant defines visual transparency of graphene. *Science*, 320(5881):1308–1308, 2008.

[79] AN Grigorenko, Marco Polini, and KS Novoselov. Graphene plasmonics. *Nature photonics*, 6(11):749, 2012.

[80] L. Ju, B. S. Geng, J. Horng, C. Girit, M. Martin, Z. Hao, H. A. Bechtel, X. G. Liang, A. Zettl, Y. R. Shen, and F. Wang. Graphene plasmonics for tunable terahertz metamaterials. *Nature nanotechnology*, 6(10):630–634, 2011.

[81] Hua Zhang. Ultrathin two-dimensional nanomaterials. *ACS nano*, 9(10):9451–9469, 2015.

[82] Philippe Tassin, Thomas Koschny, and Costas M Soukoulis. Graphene for terahertz applications. *Science*, 341(6146):620–621, 2013.

[83] Tony Low and Phaedon Avouris. Graphene plasmonics for terahertz to mid-infrared applications. *ACS nano*, 8(2):1086–1101, 2014.

[84] Sanshui Xiao, Xiaolong Zhu, Bo-Hong Li, and N Asger Mortensen. Graphene-plasmon polaritons: From fundamental properties to potential applications. *Frontiers of Physics*, 11(2):117801, 2016.

[85] Tony Low, Andrey Chaves, Joshua D Caldwell, Anshuman Kumar, Nicholas X Fang, Phaedon Avouris, Tony F Heinz, Francisco Guinea, Luis Martin-Moreno, and Frank Koppens. Polaritons in layered two-dimensional materials. *Nature materials*, 16(2):182–194, 2017.

[86] Marinko Jablan, Hrvoje Buljan, and Marin Soljačić. Plasmonics in graphene at infrared frequencies. *Physical review B*, 80(24):245435, 2009.

[87] Victor W Brar, Min Seok Jang, Michelle Sherrott, Josue J Lopez, and Harry A Atwater. Highly confined tunable mid-infrared plasmonics in graphene nanoresonators. *Nano letters*, 13(6):2541–2547, 2013.

[88] Yan Francescato, Vincenzo Giannini, Jingjing Yang, Ming Huang, and Stefan A Maier. Graphene sandwiches as a platform for broadband molecular spectroscopy. *ACS Photonics*, 1(5):437–443, 2014.

[89] Sheng Shen, Arvind Narayanaswamy, and Gang Chen. Surface phonon polaritons mediated energy transfer between nanoscale gaps. *Nano letters*, 9(8):2909–2913, 2009.

[90] Joshua D Caldwell, Lucas Lindsay, Vincenzo Giannini, Igor Vurgaftman, Thomas L Reinecke, Stefan A Maier, and Orest J Glembocki. Low-loss, infrared and terahertz nanophotonics using surface phonon polaritons. *Nanophotonics*, 4(1):44–68, 2015.

[91] Thomas Taubner, Dmitriy Korobkin, Yaroslav Urzhumov, Gennady Shvets, and Rainer Hillenbrand. Near-field microscopy through a sic superlens. *Science*, 313(5793):1595–1595, 2006.

[92] Joshua D Caldwell, Orest J Glembocki, Yan Francescato, Nicholas Sharac, Vincenzo Giannini, Francisco J Bezares, James P Long, Jeffrey C Owrutsky, Igor Vurgaftman, Joseph G Tischler, et al. Low-loss, extreme subdiffraction photon confinement via silicon carbide localized surface phonon polariton resonators. *Nano letters*, 13(8):3690–3697, 2013.

[93] R Hillenbrand, T Taubner, and F Keilmann. Phonon-enhanced light–matter interaction at the nanometre scale. *Nature*, 418(6894):159, 2002.

[94] Yiguo Chen, Yan Francescato, Joshua D Caldwell, Vincenzo Giannini, Tobias WW Maß, Orest J Glembocki, Francisco J Bezares, Thomas Taubner, Richard Kasica, Minghui Hong, et al. Spectral tuning of localized surface phonon polariton resonators for low-loss mid-ir applications. *Acs Photonics*, 1(8):718–724, 2014.

[95] Yan Francescato. *New frequencies and geometries for plasmonics and metamaterials*. PhD thesis, Imperial College London, 2014.

[96] Joshua D Caldwell, Lucas Lindsay, Vincenzo Giannini, Igor Vurgaftman, Thomas L Reinecke, Stefan A Maier, and Orest J Glembocki. Low-loss, infrared and terahertz nanophotonics using surface phonon polaritons. *Nanophotonics*, 4(1):44–68, 2015.

[97] Bryan T Spann, Ryan Compton, Daniel Ratchford, James P Long, Adam D Dunkelberger, Paul B Klein, Alexander J Giles, Joshua D Caldwell, and Jeffrey C Owrutsky. Photoinduced tunability of the reststrahlen band in 4 h- sic. *Physical Review B*, 93(8):085205, 2016.

[98] Peining Li, Xiaosheng Yang, Tobias WW Maß, Julian Hanss, Martin Lewin, Ann-Katrin U Michel, Matthias Wuttig, and Thomas Taubner. Reversible optical switching of highly confined phonon–polaritons with an ultrathin phase-change material. *Nature materials*, 15(8):870, 2016.

[99] J. D. Caldwell, O. J. Glembocki, Y. Francescato, N. Sharac, V. Giannini, F. J. Bezares, J. P. Long, J. C. Owrutsky, I. Vurgaftman, J. G. Tischler, V. D. Wheeler, N. D. Bassim, L. M. Shirey, R. Kasica, and S. A. Maier. Low-loss, extreme subdiffraction photon confinement via silicon carbide localized surface phonon polariton resonators. *Nano letters*, 13(8):3690–3697, 2013.

[100] Y. G. Chen, Y. Francescato, J. D. Caldwell, V. Giannini, T. W. W. Mass, O. J. Glembocki, F. J. Bezares, T. Taubner, R. Kasica, M. H. Hong, and S. A. Maier. Spectral tuning of localized surface phonon polariton resonators for low-loss mid-ir applications. *ACS Photonics*, 1(8):718–724, 2014.

[101] Joshua D Caldwell, Igor Vurgaftman, Joseph G Tischler, Orest J Glembocki, Jeffrey C Owrutsky, and Thomas L Reinecke. Atomic-scale photonic hybrids for mid-infrared and terahertz nanophotonics. *Nature nanotechnology*, 11(1):9–15, 2016.

[102] P Törmä and William L Barnes. Strong coupling between surface plasmon polaritons and emitters: a review. *Reports on Progress in Physics*, 78(1):013901, 2014.

[103] Hugen Yan, Tony Low, Wenjuan Zhu, Yanqing Wu, Marcus Freitag, Xuesong Li, Francisco Guinea, Phaedon Avouris, and Fengnian Xia. Damping pathways of mid-infrared plasmons in graphene nanostructures. *Nature Photonics*, 7(5):394, 2013.

[104] Xiaolong Zhu, Weihua Wang, Wei Yan, Martin B Larsen, Peter Bøggild, Thomas Garm Pedersen, Sanshui Xiao, Jian Zi, and N Asger Mortensen. Plasmon–phonon coupling in large-area graphene dot and antidot arrays fabricated by nanosphere lithography. *Nano letters*, 14(5):2907–2913, 2014.

[105] Victor W Brar, Min Seok Jang, Michelle Sherrott, Seyoon Kim, Josue J Lopez, Laura B Kim, Mansoo Choi, and Harry Atwater. Hybrid surface-phonon-plasmon polariton modes in graphene/monolayer h-bn heterostructures. *Nano letters*, 14(7):3876–3880, 2014.

[106] Yu Liu and Roy F Willis. Plasmon-phonon strongly coupled mode in epitaxial graphene. *Physical Review B*, 81(8):081406, 2010.

[107] RJ Koch, Th Seyller, and JA Schaefer. Strong phonon-plasmon coupled modes in the graphene/silicon carbide heterosystem. *Physical Review B*, 82(20):201413, 2010.

[108] Z. Fei, G. O. Andreev, W. Z. Bao, L. F. M. Zhang, A. S. McLeod, C. Wang, M. K. Stewart, Z. Zhao, G. Dominguez, M. Thiemens, M. M. Fogler, M. J. Tauber, A. H. Castro-Neto, C. N. Lau, F. Keilmann, and D. N. Basov. Infrared nanoscopy of dirac plasmons at the graphene–sio2 interface. *Nano letters*, 11(11):4701–4705, 2011.

[109] Hugen Yan, Tony Low, Wenjuan Zhu, Yanqing Wu, Marcus Freitag, Xuesong Li, Francisco Guinea, Phaedon Avouris, and Fengnian Xia. Damping pathways of mid-infrared plasmons in graphene nanostructures. *Nature Photonics*, 7(5):394–399, 2013.

[110] Xiaolong Zhu, Weihua Wang, Wei Yan, Martin B Larsen, Peter Bøggild, Thomas Garm Pedersen, Sanshui Xiao, Jian Zi, and N Asger Mortensen. Plasmon–phonon coupling in large-area graphene dot and antidot arrays fabricated by nanosphere lithography. *Nano letters*, 14(5):2907–2913, 2014.

[111] Victor W Brar, Min Seok Jang, Michelle Sherrott, Seyoon Kim, Josue J Lopez, Laura B Kim, Mansoo Choi, and Harry Atwater. Hybrid surface-phonon-plasmon polariton modes in graphene/monolayer h-bn heterostructures. *Nano letters*, 14(7):3876–3880, 2014.

[112] Ingrid D Barcelos, Alisson R Cadore, Leonardo C Campos, Angelo Malachias, K Watanabe, T Taniguchi, Francisco CB Maia, Raul Freitas, and Christoph Deneke. Graphene/h-

bn plasmon–phonon coupling and plasmon delocalization observed by infrared nano-spectroscopy. *Nanoscale*, 7(27):11620–11625, 2015.

[113] S Dai, Q Ma, MK Liu, T Andersen, Z Fei, MD Goldflam, M Wagner, K Watanabe, T Taniguchi, M Thiemens, et al. Graphene on hexagonal boron nitride as a tunable hyperbolic metamaterial. *Nature nanotechnology*, 10(8):nnano–2015, 2015.

[114] Achim Woessner, Mark B Lundeberg, Yuanda Gao, Alessandro Principi, Pablo Alonso-González, Matteo Carrega, Kenji Watanabe, Takashi Taniguchi, Giovanni Vignale, Marco Polini, et al. Highly confined low-loss plasmons in graphene–boron nitride heterostructures. *Nature materials*, 14(4):421, 2015.

[115] Yilei Li, Hugen Yan, Damon B Farmer, Xiang Meng, Wenjuan Zhu, Richard M Osgood, Tony F Heinz, and Phaedon Avouris. Graphene plasmon enhanced vibrational sensing of surface-adsorbed layers. *Nano letters*, 14(3):1573–1577, 2014.

[116] Christian Huck, Jochen Vogt, Tomáš Neuman, Tadaaki Nagao, Rainer Hillenbrand, Javier Aizpurua, Annemarie Pucci, and Frank Neubrech. Strong coupling between phonon-polaritons and plasmonic nanorods. *Optics Express*, 24(22):25528–25539, 2016.

[117] MG Raizen, RJ Thompson, RJ Brecha, HJ Kimble, and HJ Carmichael. Normal-mode splitting and linewidth averaging for two-state atoms in an optical cavity. *Physical Review Letters*, 63(3):240, 1989.

[118] RJ Thompson, G Rempe, and HJ Kimble. Observation of normal-mode splitting for an atom in an optical cavity. *Physical Review Letters*, 68(8):1132, 1992.

[119] Rohit Chikkaraddy, Bart De Nijs, Felix Benz, Steven J Barrow, Oren A Scherman, Edina Rosta, Angela Demetriadou, Peter Fox, Ortwin Hess, and Jeremy J Baumberg. Single-molecule strong coupling at room temperature in plasmonic nanocavities. *Nature*, 535(7610):127, 2016.

[120] P Törmä and William L Barnes. Strong coupling between surface plasmon polaritons and emitters: a review. *Reports on Progress in Physics*, 78(1):013901, 2015.

[121] Ke Li, Jamie M Fitzgerald, Xiaofei Xiao, Joshua D Caldwell, Cheng Zhang, Stefan A Maier, Xiaofeng Li, and Vincenzo Giannini. Graphene plasmon cavities made with silicon carbide. *ACS Omega*, 2(7):3640–3646, 2017.

[122] Weilu Gao, Jie Shu, Ciyuan Qiu, and Qianfan Xu. Excitation of plasmonic waves in graphene by guided-mode resonances. *ACS nano*, 6(9):7806–7813, 2012.

[123] TM Slipchenko, ML Nesterov, L Martin-Moreno, and A Yu Nikitin. Analytical solution for the diffraction of an electromagnetic wave by a graphene grating. *Journal of Optics*, 15(11):114008, 2013.

[124] Bo Zhao and Zhuomin M Zhang. Strong plasmonic coupling between graphene ribbon array and metal gratings. *ACS Photonics*, 2(11):1611–1618, 2015.

[125] Z. Fei, A. S. Rodin, G. O. Andreev, W. Bao, A. S. McLeod, M. Wagner, L. M. Zhang, Z. Zhao, M. Thiemens, G. Dominguez, M. M. Fogler, A. H. Castro Neto, C. N. Lau, F. Keilmann, and D. N. Basov. Gate-tuning of graphene plasmons revealed by infrared nano-imaging. *Nature*, 487(7405):82–85, 2012.

[126] Achim Woessner, Mark B Lundeberg, Yuanda Gao, Alessandro Principi, Pablo Alonso-González, Matteo Carrega, Kenji Watanabe, Takashi Taniguchi, Giovanni Vignale, Marco Polini, James Hone, Rainer Hillenbrand, and Frank H L Koppens. Highly confined low-loss plasmons in graphene-boron nitride heterostructures. *Nature Materials*, 14(4):421–425, 2014.

[127] Jianing Chen, Maxim L Nesterov, Alexey Yu Nikitin, Sukosin Thongrattanasiri, Pablo Alonso-González, Tetiana M Slipchenko, Florian Speck, Markus Ostler, Thomas Seyller, Iris Crassee, et al. Strong plasmon reflection at nanometer-size gaps in monolayer graphene on sic. *Nano letters*, 13(12):6210–6215, 2013.

[128] P. Alonso-Gonzalez, A. Y. Nikitin, F. Golmar, A. Centeno, A. Pesquera, S. Velez, J. Chen, G. Navickaite, F. Koppens, A. Zurutuza, F. Casanova, L. E. Hueso, and R. Hillenbrand. Controlling graphene plasmons with resonant metal antennas and spatial conductivity patterns. *Science*, 344(6190):1369–1373, jun 2014.

[129] Luping Du, Dingyuan Tang, and Xiaocong Yuan. Edge-reflection phase directed plasmonic resonances on graphene nano-structures. *Optics express*, 22(19):22689–22698, 2014.

[130] J Gómez Rivas, G Vecchi, and V Giannini. Surface plasmon polariton-mediated enhancement of the emission of dye molecules on metallic gratings. *New Journal of Physics*, 10(10):105007, 2008.

[131] V Giannini, Y Zhang, M Forcales, and J Gómez Rivas. Long-range surface polaritons in ultra-thin films of silicon. *Optics express*, 16(24):19674–19685, 2008.

[132] Andrea E Schlather, Nicolas Large, Alexander S Urban, Peter Nordlander, and Naomi J Halas. Near-field mediated plexcitonic coupling and giant rabi splitting in individual metallic dimers. *Nano letters*, 13(7):3281–3286, 2013.

[133] David Woolf, Marko Loncar, and Federico Capasso. The forces from coupled surface plasmon polaritons in planar waveguides. *Optics express*, 17(22):19996–20011, 2009.

[134] V Giannini, Y Zhang, M Forcales, and J Gómez Rivas. Long-range surface polaritons in ultra-thin films of silicon. *Optics Express*, 16(24):19674–19685, 2008.

[135] Cameron LC Smith, Nicolas Stenger, Anders Kristensen, N Asger Mortensen, and Sergey I Bozhevolnyi. Gap and channeled plasmons in tapered grooves: a review. *Nanoscale*, 7(21):9355–9386, 2015.

[136] Jessica R Piper and Shanhui Fan. Total absorption in a graphene monolayer in the optical regime by critical coupling with a photonic crystal guided resonance. *ACS Photonics*, 1(4):347–353, 2014.

[137] C. F. Chen, C. H. Park, B. W. Boudouris, J. Horng, B. S. Geng, C. Girit, A. Zettl, M. F. Crommie, R. A. Segalman, S. G. Louie, and F. Wang. Controlling inelastic light scattering quantum pathways in graphene. *Nature*, 471(7340):617–620, 2011.

[138] Aleksandar D Rakić. Algorithm for the determination of intrinsic optical constants of metal films: application to aluminum. *Applied optics*, 34(22):4755–4767, 1995.

[139] Shaista Babar and JH Weaver. Optical constants of cu, ag, and au revisited. *Applied Optics*, 54(3):477–481, 2015.

[140] Matthew J Allen, Vincent C Tung, and Richard B Kaner. Honeycomb carbon: a review of graphene. *Chemical reviews*, 110(1):132–145, 2009.

[141] Robert J Young, Ian A Kinloch, Lei Gong, and Kostya S Novoselov. The mechanics of graphene nanocomposites: a review. *Composites Science and Technology*, 72(12):1459–1476, 2012.

[142] Alexander A Balandin. Thermal properties of graphene and nanostructured carbon materials. *Nature materials*, 10(8):569, 2011.

[143] F Javier Garcia de Abajo. Graphene plasmonics: challenges and opportunities. *Acs Photonics*, 1(3):135–152, 2014.

[144] Vasilios Georgakilas, Jitendra N Tiwari, K Christian Kemp, Jason A Perman, Athanasios B Bourlinos, Kwang S Kim, and Radek Zboril. Noncovalent functionalization of graphene and graphene oxide for energy materials, biosensing, catalytic, and biomedical applications. *Chemical reviews*, 116(9):5464–5519, 2016.

[145] Sukjae Jang, Euyheon Hwang, Youngbin Lee, Seungwoo Lee, and Jeong Ho Cho. Multifunctional graphene optoelectronic devices capable of detecting and storing photonic signals. *Nano letters*, 15(4):2542–2547, 2015.

[146] Xiangjian Wan, Yi Huang, and Yongsheng Chen. Focusing on energy and optoelectronic applications: a journey for graphene and graphene oxide at large scale. *Accounts of chemical research*, 45(4):598–607, 2012.

[147] Liang Kou, Tieqi Huang, Bingna Zheng, Yi Han, Xiaoli Zhao, Karthikeyan Gopalsamy, Haiyan Sun, and Chao Gao. Coaxial wet-spun yarn supercapacitors for high-energy density and safe wearable electronics. *Nature communications*, 5:3754, 2014.

[148] Yuning Meng, Yang Zhao, Chuangang Hu, Huhu Cheng, Yue Hu, Zhipan Zhang, Gaoquan Shi, and Liangti Qu. All-graphene core-sheath microfibers for all-solid-state, stretchable fibriform supercapacitors and wearable electronic textiles. *Advanced materials*, 25(16):2326–2331, 2013.

[149] Diego Correas-Serrano and J Sebastian Gomez-Diaz. Graphene-based antennas for terahertz systems: A review. *arXiv preprint arXiv:1704.00371*, 2017.

[150] Long Ju, Baisong Geng, Jason Horng, Caglar Girit, Michael Martin, Zhao Hao, Hans A Bechtel, Xiaogan Liang, Alex Zettl, Y Ron Shen, et al. Graphene plasmonics for tunable terahertz metamaterials. *Nature nanotechnology*, 6(10):630, 2011.

[151] Xiaofei Xiao, Xiaofeng Li, Joshua D Caldwell, Stefan A Maier, and Vincenzo Giannini. Theoretical analysis of graphene plasmon cavities. *Applied Materials Today*, 12:283–293, 2018.

[152] Yan Francescato. *New frequencies and geometries for plasmonics and metamaterials*. PhD thesis, Imperial College London, 2014.

[153] Jiao Lin, JP Balthasar Mueller, Qian Wang, Guanghui Yuan, Nicholas Antoniou, Xiao-Cong Yuan, and Federico Capasso. Polarization-controlled tunable directional coupling of surface plasmon polaritons. *Science*, 340(6130):331–334, 2013.

[154] Yuan Zhao and Yanwu Zhu. Graphene-based hybrid films for plasmonic sensing. *Nanoscale*, 7(35):14561–14576, 2015.

[155] Lisa V Brown, Ke Zhao, Nicholas King, Heidar Sobhani, Peter Nordlander, and Naomi J Halas. Surface-enhanced infrared absorption using individual cross antennas tailored to chemical moieties. *Journal of the American Chemical Society*, 135(9):3688–3695, 2013.

[156] Dietmar Nau, A Seidel, RB Orzekowsky, S-H Lee, S Deb, and H Giessen. Hydrogen sensor based on metallic photonic crystal slabs. *Optics letters*, 35(18):3150–3152, 2010.

[157] Michael C Kemp, PF Taday, Bryan E Cole, JA Cluff, Anthony J Fitzgerald, and William R Tribe. Security applications of terahertz technology. In *Terahertz for Military and Security Applications*, volume 5070, pages 44–53. International Society for Optics and Photonics, 2003.

[158] Salih Ergün and Selçuk Sönmez. Terahertz technology for military applications. *Journal of Management and Information Science*, 3(1):13–16, 2015.

[159] Martti Kauranen and Anatoly V Zayats. Nonlinear plasmonics. *nature photonics*, 6(11):737, 2012.

[160] Guixin Li, Shuang Zhang, and Thomas Zentgraf. Nonlinear photonic metasurfaces. *Nature Reviews Materials*, 2(5):17010, 2017.